26-04-04 13:55:06

1. Introduction

The deep drawing process is a commonly used forming process for sheet metal. The principle of the deep drawing process is displayed in Figure 1-1. An initially flat piece of sheet material, the blank, is clamped between the die and the blank holder. The blank holder is loaded by the blank holder force F_{blh}, see Figure 1-1(a). The blank holder force is necessary to prevent wrinkling and to control the flow of the material. Then the punch moves down with displacement u to deform the blank. The shape of the punch and eventually the contra-shape of the die define the shape of the formed blank, see Figure 1-1(b). During the punch movement, the material is drawn out of the die/blank holder region into the die. That is why this process is called deep drawing.

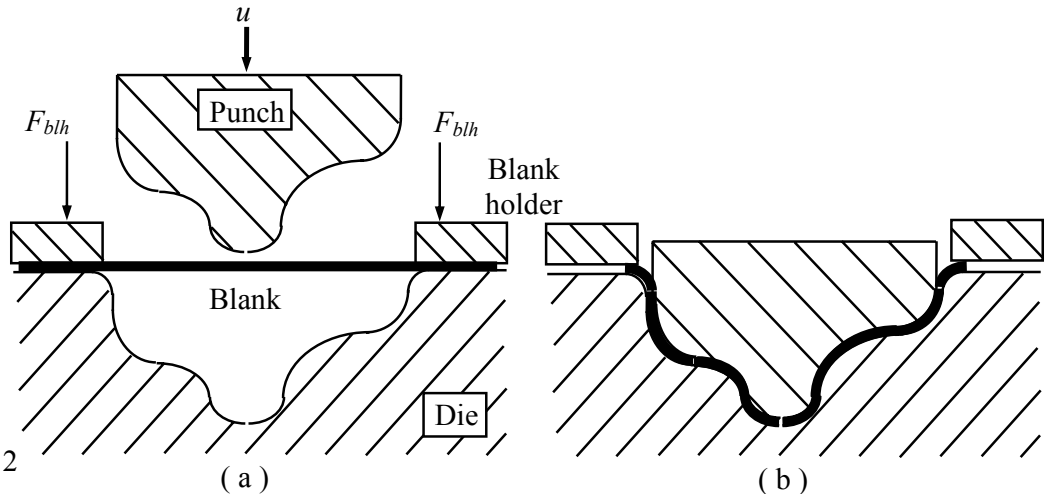

Figure 1-1 *Principle of the deep drawing process.*

The material flow into the die is not only influenced by the blank holder but it is also influenced by the use of a lubricant, by coatings on the blank and by placing drawbeads in the die/blank holder region. The influence of the lubricant is investigated by ter Haar. [Haar, 1996]. This research project resulted in an advanced friction model which describes the evaluation of friction during the forming sheet metal products. A drawbead is a kind of obstacle over which the blank material has to flow, a drawbead locally restrains the material flow.

The deep drawing process is well used in the packaging industry and in the automotive industry. In the packaging industry the process is, among others used to produce petfood containers and to produce beverage cans [Nichols, 1995][Bongaerts, 1996]. In the automotive industry many parts are produced by using the deep drawing process, for example inner parts, stiffeners and body panels [El Mouatassim, 1995][Schmidt, 1996].

The tools in combination with the blank are important parameters that define the final shape of the product. When the blank shape and the tools are not optimally designed, a product with a deviating shape or with failures is produced. The most common types of failure are wrinkling and tearing.
Other important process parameters are the material behaviour and the friction. Most sheet material is anisotropic, this means that the material behaves differently in different directions because of the rolling process. An example of anisotropic behaviour is the development of the so called ears in an axi-symmetric product. The friction behaviour depends on a lot of parameters, for example whether a lubricant is used or not, the surface roughness of the tools and the blank, the normal pressure and the sliding velocity. These parameters depend among others on the sort of lubricant and the coatings on the blank.
In order to produce a complicated part with the deep drawing process all these parameters must be accurately tuned. Once the tools are designed and produced, an extensive trial and error process starts to determine the right parameters. Sometimes this tuning results in a re-design of the tools or even a new set of tools. In order to reduce this press shop tuning and to avoid the waste of time and money, numerical models can be used to perform a pre-tuning.

Numerical models can simulate the deep drawing process before the tools are produced. The tools must only exist in numerical form. Most CAD packages used to design the tools have the possibility to generate a tool description suitable for numerical models. With the numerical model it is possible to study the influence of the material, the friction and the other process parameters on the deep drawing process. Even a change of the deep drawing tools can be performed without any risk. This makes the numerical models a powerful tool in the design of a deep drawing product.
In the product design phase, one has to ensure that the product can be produced according the wanted quality. In this phase a simple and fast model like the inverse approach can be used [Barlet, 1996]. Once the product geometry is known, the process design starts, the right tool geometry and process parameters must be obtained. In this phase more

sophisticated models such as the finite element method can be used [Carleer, 1996]. This method is also used for trouble shooting production problems [Langerak, 1995].

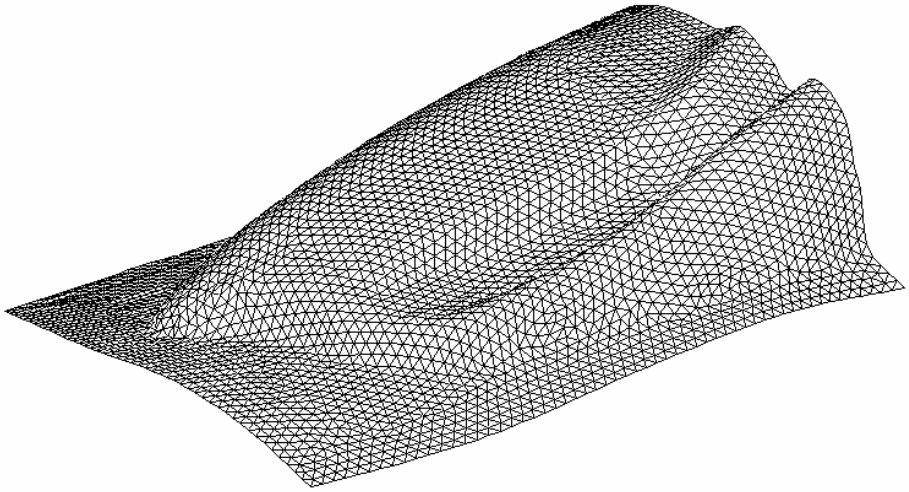

Figure 1-2 *Just a nice picture of a simulated front fender* [Koning, 1996].

In this work the finite element program DIEKA is used. DIEKA has been developed at the University of Twente in close co-operation with Hoogovens Research & Development and has been designed to simulate among others the deep drawing process. The advantage of developing one's own program is the flexibility. Small modifications to improve the program are performed very quickly. Special purpose models can be implemented when an application asks for it. Examples of these models are material models, friction models, special sandwich laminate models and contact algorithms. Further the limits of the program are well known, the impossible will never be tried. A disadvantage is that you can never blame someone else.

The DIEKA deep drawing history started in 1987. In the last decade a lot of researchers have been working to develop DIEKA to its present standard. In 1992, Vreede presented the application of axi-symmetric and rectangular deep drawing simulations. Further, a deep drawing simulation of a automotive product was presented [Vreede, 1992].

In 1997, this work presents the main research of the last five years. The goal of the present research was to develop the existing software in order to better satisfy the requirement for industrial applications. The model had to be extended at some points. The material description is extended to an elastic-plastic formulation, which offers the possibility for analysing springback phenomena. The material anisotropy is also incorporated in the material description. Further a new material description based on multi-axial stress states has been implemented. In order to predict failure in a product, a forming limit diagram is used. The failure of coatings on the blank can be predicted based on forming limit diagrams for coatings.
In the blank description only stretching energy was incorporated. When the curvature of a product is sharp according to the blank thickness this description fails, therefore the bending energy is also incorporated in the blank description. The contact between the blank and the tools is the driving force for the deep drawing process and therefore of major interest in the simulations. The contact detection is improved to handle CAD

generated tool descriptions. The friction model is extended to a wider applicable model. In order to control the flow of the material, drawbeads are used. A model to efficiently incorporate the drawbead is developed. Applications of the different models complete this work.

1.1 References

[Barlet, 1996]
Barlet O., J. L. Batoz, Y. Q. Guo, F. Mercier, H. Naceur, C. Knopf-Lenior, *Optimum design of blank contours using the inverse approach and a mathematical programming technique*, Numerical simulation of 3-D sheet metal forming processes, G. L. Kinzel et al. (eds.), Dearborn, 1996

[Bongaerts, 1996]
Bongaerts P. C. P., *Buckling in a square petfood container*, Sheet metal 1996, H. J. J. Kals et al. (eds.), 1996

[Carleer, 1996]
Carleer B. D., J. Huétink, *Closing the gap between the workshop and numerical simulations in sheet metal forming*, ECCOMAS '96, J. -A. Désidéri et al. (eds.), Paris, 1996

[El Mouatassim, 1995]
El Mouatassim M., B. Thomas, J. -P. Jameux, E. Di Pasquale, *An industrial finite element code for one-step simulation of sheet metal forming*, Simulation of materials processing: theory, methods and applications, S. F. Shen & P. Dawson (eds.), Balkema, Rotterdam, 1995

[Haar, 1996]
Haar R. ter, *Friction in sheet metal forming, the influence of (local) contact conditions and deformation*. PhD-thesis, University of Twente, 1996

[Koning, 1996]
Koning A., *Deep drawing simulations of a front fender*, Graduate report, University of Twente, 1996

[Langerak, 1995]
Langerak N. A. J., *The application of strain measurements and computer simulations to analyse sheet metal forming processes*, Materialen (in Dutch), 3, May/June, 1995

[Nichols, 1995]
Nichols I. E., G. Louwerse, A. J. L. Crook, *The application of novel numerical methods to multiple state forming operations in the manufacture of thin walled steel cans*, Simulation of materials processing: theory, methods and applications, S. F. Shen & P. Dawson (eds.), Balkema, Rotterdam, 1995

[Schmidt, 1996]

Schmidt H., T. Chung Vu, L. Recke, *Sheet forming simulation, the breakthrough of a new technology*, Numerical simulation of 3-D sheet metal forming processes, G. L. Kinzel et al. (eds.), Dearborn, 1996

[Vreede, 1992]
Vreede P. T., *A finite element method for simulations of 3-dimensional sheet metal forming*, PhD-thesis, University of Twente, 1992

2. Continuum Mechanics

A sample of material is built up of a finite number of 'particles'. The appearance of these 'particles' depends on the scale at which the material is observed. On the smallest scale atoms can be observed. When increasing the scale, molecules can be observed and increasing the scale further crystallites can be recognised. When the scale is large enough no 'substructure' can be distinguished; the macroscopic scale is reached. On this scale a sample material is treated as a continuous medium. The field of continuum mechanics describes the material behaviour of such a sample. This field is split up into the general equations and the constitutive equations. The mathematical description of finite deformations is based on the principles of the continuum mechanics [Huétink, 1986],[Besseling, 1994],[Betten, 1993]. In section 2.1 a brief outline of the deformations of a continuous body is given. This is indicated as kinematics and strains. The section 2.2 discusses the stresses in a body. These two sections deal with the general principles. The link between the strains and the stresses is discussed in section 2.3, the constitutive equations.

2.1 Kinematics and Strains

A particle of a material is considered. Its position in the initial configuration is defined by the vector $\boldsymbol{X}$. The current configuration is positioned by the vector $\boldsymbol{x}$, Figure 2-1:

$$\boldsymbol{x} = \boldsymbol{x}(\boldsymbol{X}, t) \quad ; \quad \boldsymbol{X} = \boldsymbol{X}(\boldsymbol{x}, t) \tag{2-1}$$

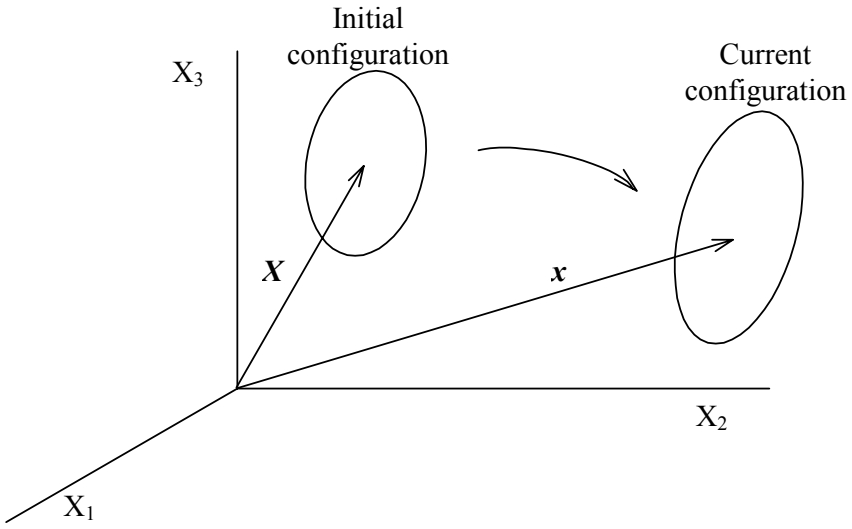

Figure 2-1 *A particle of material in its initial and current configuration.*

There is always a mapping between the initial configuration and the current configuration, This one-to-one correspondence is represented by the deformation gradient tensor $\boldsymbol{F}$:

$$d\boldsymbol{x} = \boldsymbol{F} \cdot d\boldsymbol{X} \quad ; \quad d\boldsymbol{X} = \boldsymbol{F}^{-1} \cdot d\boldsymbol{x} \tag{2-2}$$

The tensor F and its inverse are expressed as:

$$\boldsymbol{F} = \left(\frac{\partial \boldsymbol{x}}{\partial \boldsymbol{X}} \right)_t \quad ; \quad \boldsymbol{F}^{-1} = \left(\frac{\partial \boldsymbol{X}}{\partial \boldsymbol{x}} \right)_t \tag{2-3}$$

Polar decomposition results in an orthogonal and a symmetric part:

$$\boldsymbol{F} = \boldsymbol{R} \cdot \boldsymbol{U} = \boldsymbol{V} \cdot \boldsymbol{R} \tag{2-4}$$

Where $\boldsymbol{R}$ is the rotation tensor, $\boldsymbol{U}$ the right stretch tensor and $\boldsymbol{V}$ the left stretch tensor.

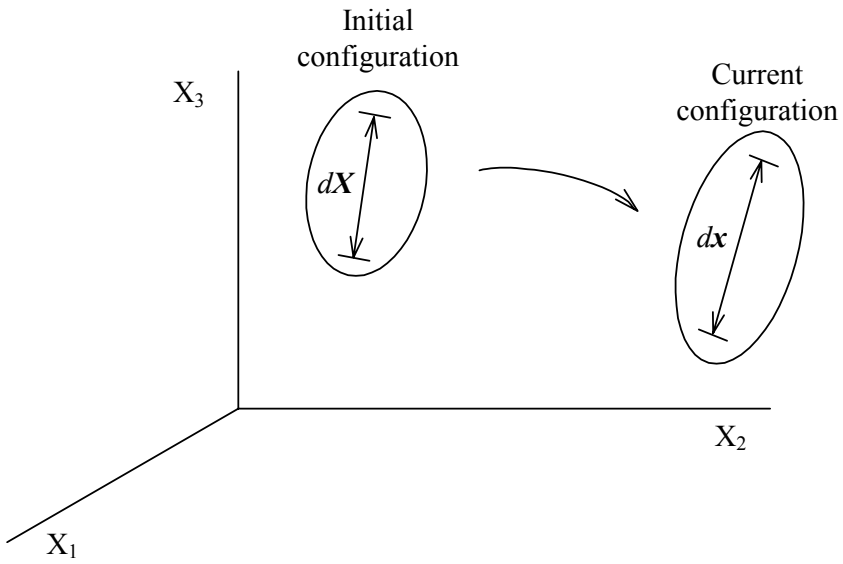

Figure 2-2 *An infinitesimal line element in the current and in the initial configuration.*

The strain is defined as the difference between the square length of an infinitesimal line element in the current configuration and in the initial configuration, Figure 2-2:

$$\|d\boldsymbol{x}\|^2 - \|d\boldsymbol{X}\|^2 \tag{2-5}$$

In the material description the initial configuration is the reference state. The strain in the material description is defined as:

$$\|d\boldsymbol{x}\|^2 - \|d\boldsymbol{X}\|^2 = 2\, d\boldsymbol{X} \cdot \boldsymbol{\eta} \cdot d\boldsymbol{X} \tag{2-6}$$

Where $\boldsymbol{\eta}$ is the Lagrangian strain tensor which is written as:

$$\boldsymbol{\eta} = \tfrac{1}{2}\left(\boldsymbol{F}^T \cdot \boldsymbol{F} - \boldsymbol{I}\right) \tag{2-7}$$

From here the right Cauchy Green tensor is defined:

$$\boldsymbol{C} = \boldsymbol{F}^T \cdot \boldsymbol{F} = \boldsymbol{U}^2 \tag{2-8}$$

In the spatial description, the current configuration is the reference state. The strain definition in the spatial description is:

$$\|d\boldsymbol{x}\|^2 - \|d\boldsymbol{X}\|^2 = 2\, d\boldsymbol{x} \cdot \boldsymbol{\varepsilon} \cdot d\boldsymbol{x} \tag{2-9}$$

Where $\boldsymbol{\varepsilon}$ is the Euler Almansi strain tensor which is written as:

$$\boldsymbol{\varepsilon} = \tfrac{1}{2}\left(\boldsymbol{I} - \left(\boldsymbol{F} \cdot \boldsymbol{F}^T\right)^{-1}\right) \tag{2-10}$$

From here the left Cauchy Green tensor is defined:

$$\boldsymbol{B} = \boldsymbol{F} \cdot \boldsymbol{F}^T = \boldsymbol{V}^2 \tag{2-11}$$

For small deformations the right and left Cauchy Green tensor coincide:

$$\boldsymbol{C} \cong \boldsymbol{B} \cong \boldsymbol{I} + 2\boldsymbol{\varepsilon} = \boldsymbol{I} + 2\boldsymbol{\eta} \tag{2-12}$$

With the infinitesimal strain expressed as a function of the displacements $\boldsymbol{u}$:

$$\boldsymbol{\varepsilon} = \boldsymbol{\eta} = \tfrac{1}{2}\left(\vec{\nabla}\boldsymbol{u} + \boldsymbol{u}\overleftarrow{\nabla}\right) \tag{2-13}$$

The change of a physical quantity ψ can be expressed in the material description with $\boldsymbol{X}$ and t as independent variables and in the spatial description with $\boldsymbol{x}$ and t as independent variables. These two derivatives are related by:

$$\dot{\psi} = \frac{d}{dt}\psi(\boldsymbol{X},t) = \frac{\partial}{\partial t}\psi(\boldsymbol{x},t) + \boldsymbol{v}\cdot\nabla\psi \tag{2-14}$$

Where v is the velocity of a material point:

$$\boldsymbol{v} = \dot{\boldsymbol{x}} = \frac{d\boldsymbol{x}}{dt} \tag{2-15}$$

The material rate of change of a volume integral depending on Ψ can be written as:

$$\frac{d}{dt}\int_V \Psi dV = \int_{V_0}\left(\dot{\Psi}J + \Psi\dot{J}\right)dV_0 \tag{2-16}$$

The Jacobian J is the determinant of $\boldsymbol{F}$, it is a measure for the volume change. The rate of change of the volume is denoted by $\dot{J}$.

The rate of change of the line element d$\boldsymbol{x}$ can be written as:

$$(d\boldsymbol{x})^{\cdot} = \frac{\partial \boldsymbol{v}}{\partial \boldsymbol{x}}d\boldsymbol{x} = \boldsymbol{L}d\boldsymbol{x} \tag{2-17}$$

In which $\boldsymbol{L}$ is the spatial gradient of the velocity. In general this gradient is non symmetric and can be composed into a symmetric part, the rate of deformation $\boldsymbol{D}$, and an anti symmetric part, the spin tensor $\boldsymbol{W}$:

$$\boldsymbol{D} = \tfrac{1}{2}\left(\boldsymbol{L} + \boldsymbol{L}^T\right) \quad ; \quad \boldsymbol{W} = \tfrac{1}{2}\left(\boldsymbol{L} - \boldsymbol{L}^T\right) \tag{2-18}$$

2.2 Stresses

An arbitrary cross section of a deformed continuum is looked into. In the cross section $\boldsymbol{n}$ is the normal vector and is $\boldsymbol{P}$ the force per unit surface area. This vector can be represented as:

$$\boldsymbol{P} = \boldsymbol{\sigma} \cdot \boldsymbol{n} \tag{2-19}$$

Where $\boldsymbol{\sigma}$ is the Cauchy stress tensor, which is the true stress in the current configuration. It is an objective tensor. In the absence of distributed moments or coupled stresses it follows from the conservation of angular momentum that the Cauchy stress tensor is symmetric. The Cauchy stress can also be defined by the following equation, Figure 2-3:

$$d\boldsymbol{P} = \boldsymbol{\sigma} \cdot d\boldsymbol{S} \tag{2-20}$$

Where $d\boldsymbol{P}$ is a force vector acting on an oriented surface element $d\boldsymbol{S} = \boldsymbol{n} \cdot dS$.

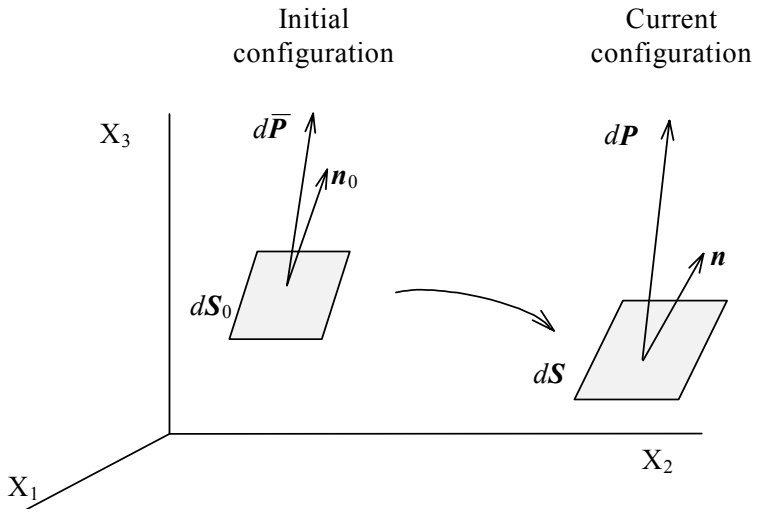

Figure 2-3 *The force vector, the normal vector and the oriented surface elements in the initial and in the current configuration.*

The first Piola Kirchhoff stress tensor is defined by projecting the force vector on the initial surface element $d\boldsymbol{S}_0 = \boldsymbol{n}_0 \cdot dS$:

$$d\boldsymbol{P} = \hat{\boldsymbol{T}} \cdot d\boldsymbol{S}_0 \tag{2-21}$$

The first Piola Kirchhoff stress tensor $\hat{\boldsymbol{T}}$ is non symmetric. For this reason the stress tensor is modified. Firstly, the force vector is transformed from the current configuration to the initial configuration according to equation (2-2)

$$d\bar{\boldsymbol{P}} = \boldsymbol{F}^{-1} \cdot d\boldsymbol{P} \tag{2-22}$$

Secondly, this force vector is projected on the initial surface. Now the second Piola Kirchhoff stress tensor $\boldsymbol{T}$ can be defined:

$$d\overline{\boldsymbol{P}} = \boldsymbol{T} \cdot d\boldsymbol{S_0} \tag{2-23}$$

This stress tensor is symmetric. The Cauchy stress tensor and the second Piola Kirchhoff stress tensor are related by the following expression:

$$\boldsymbol{\sigma} = \boldsymbol{F}^{-1} \cdot \boldsymbol{T} \cdot \boldsymbol{F}^{-T} \tag{2-24}$$

2.3 Constitutive Equations

Different materials behave differently under the same external load. To describe this behaviour there is a need for a connection between the stresses and strains in a continuum. These relations are called the constitutive equations.
The tensile test is one of the simplest tests to study the stress strain behaviour of materials. A test specimen with length L_0 and a cross section A_0 is subjected by a tensile force F. The tensile curve, Figure 2-4, is characterised by the true stress σ and the natural or logarithmic strain ε:

$$\sigma = \frac{F}{A} \quad ; \quad \varepsilon = \ln\left(\frac{\mathrm{L}}{\mathrm{L}_0}\right) \tag{2-25}$$

With F : the tensile force
A : the actual cross section area
L : the actual length of the specimen
L_0 : the initial length of the specimen

When the material goes while the force is removed back in its initial state, the behaviour is elastic or reversible. For most metals the elastic behaviour is linear:

$$\sigma = E\varepsilon \tag{2-26}$$

With E : Young's modulus

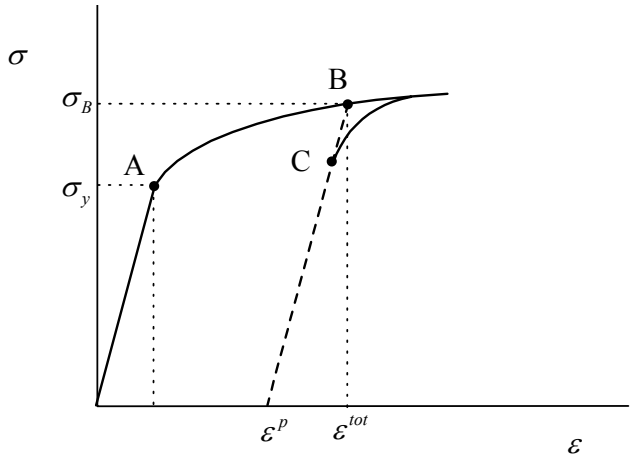

Figure 2-4 *The tensile curve.*

At a certain value of the strain the yield stress σ_y is reached, point A in Figure 2-4. The material behaviour is plastic or irreversible. At the yield stress the slope of the stress strain curve changes considerably. When the test specimen is unloaded in the plastic range, point B in Figure 2-4, a permanent plastic strain ε^p results. The plastic strain is smaller than the total strain ε^{tot} at point B. The slope of the stress strain curve during unloading is assumed to be the same as in the elastic range, the Young's modulus is assumed to be constant. So, the plastic deformations do not affect the elastic properties of the material. This is the basis of the plasticity theory. The total strain is decomposed into an elastic part and a plastic part:

$$\varepsilon^{tot} = \varepsilon^e + \varepsilon^p \tag{2-27}$$

For most engineering materials an ever increasing stress is found for continued deformation. This effect is called strain hardening. When, after unloading, the material is reloaded from ε^p the plasticity restarts at an earlier point, point C in Figure 2-4, than the previous plastic stress σ_B After further deformation the curve approaches the stress strain curve that would be found without unloading.
A similar effect is found when after unloading the material is compressed. The yielding again starts before the stress has reached the value σ_B The different behaviour under tension and compression is known as the Bauschinger effect.

The tensile test is a uni-axial test. Multi-axial stress states cannot be illustrated by a simple stress strain curve. But the uni-axial test is a suitable representation of the actual stress and strain. A mathematical formulation for the multi-axial material behaviour is given underneath.

In the linear elasticity Hooke's law is used:

$$\boldsymbol{\sigma} = \boldsymbol{E} : \boldsymbol{\varepsilon}^e \tag{2-28}$$

The stress tensor $\boldsymbol{\sigma}$ and the small elastic strain tensor $\boldsymbol{\varepsilon}^e$ are related by the fourth order elasticity tensor $\boldsymbol{E}$. When the stress and strain tensor are written as a vector and the elasticity tensor is written as a matrix the following expression for orthotropic material is found:

$$\begin{Bmatrix} \sigma_{xx} \\ \sigma_{yy} \\ \sigma_{zz} \\ \sigma_{xy} \\ \sigma_{yz} \\ \sigma_{xz} \end{Bmatrix} = \begin{bmatrix} 2G+l & l & l & 0 & 0 & 0 \\ l & 2G+l & l & 0 & 0 & 0 \\ l & l & 2G+l & 0 & 0 & 0 \\ 0 & 0 & 0 & G & 0 & 0 \\ 0 & 0 & 0 & 0 & G & 0 \\ 0 & 0 & 0 & 0 & 0 & G \end{bmatrix} \begin{Bmatrix} \varepsilon_{xx} \\ \varepsilon_{yy} \\ \varepsilon_{zz} \\ \varepsilon_{xy} \\ \varepsilon_{yz} \\ \varepsilon_{xz} \end{Bmatrix} \tag{2-29}$$

With G : the shear modulus
l : the constant of Lamé

Both parameters can be expressed by the elasticity modulus E and Poisson's ratio v:

$$G = \frac{E}{2(1+\nu)} \quad ; \quad l = \frac{\nu E}{(1+\nu)(1-2\nu)} \tag{2-30}$$

After further loading the material behaves plastic. The total strain tensor is split into an elastic part and a plastic part.

$$\boldsymbol{\varepsilon} = \boldsymbol{\varepsilon}^e + \boldsymbol{\varepsilon}^p \tag{2-31}$$

Substitution of the elastic strain tensor $\boldsymbol{\varepsilon}^e$ in Hooke's law, equation (2-28), and differentiating with respect to time gives:

$$\dot{\boldsymbol{\sigma}} = \boldsymbol{E} : \left(\dot{\boldsymbol{\varepsilon}} - \dot{\boldsymbol{\varepsilon}}^p \right) \tag{2-32}$$

In order to distinguish plastic deformation at a multi-axial stress state a yield function is defined. The yield function ϕ gives a combination of the stresses at which the material starts to deform plastic:

$$\phi = \phi(\boldsymbol{\sigma}, \lambda) \tag{2-33}$$

The yield function depends on the stresses and the accumulated plastic strain. The yield function is a potential for the plastic strain rate. The plastic deformation occurs when $\phi=0$; in the elastic region counts $\phi<0$. Drucker's postulate says that for a material volume element any complete cycle in stress space requires a non-negative energy input. The postulate must hold for every plastic strain increment, regardless how small. The postulate can be written as:

$$\left(\sigma - \sigma_0 \right) \dot{\varepsilon}^p \geq 0 \tag{2-34}$$

In this equation is σ_0 the initial stress state, σ an arbitrary value in the stress space and $\dot{\varepsilon}^p$ the corresponding plastic strain increment. The postulate is a non-physical requirement but metals satisfy it. The postulate expresses two rules. The first rule says that the yield function must be convex. The second rule says that the plastic strain rate tensor is orthogonal to the yield surface. This normality condition or flow rule is written:

$$\dot{\boldsymbol{\varepsilon}}^p = \dot{\lambda}\frac{\partial \phi}{\partial \boldsymbol{\sigma}} \quad ; \quad \dot{\lambda} \geq 0 \tag{2-35}$$

The parameter $\dot{\lambda}$ is a scalar. The flow rule holds as long as the deformation is plastic and no unloading takes place. When the deformation is elastic the scalar $\dot{\lambda}$ is set to zero. Summarised counts:

$$\begin{aligned} &\dot{\lambda} = 0 \quad \text{if} \quad \left(\phi < 0\right) \vee \left(\phi = 0 \wedge \dot{\phi} < 0\right) \\ &\dot{\lambda} > 0 \quad \text{if} \quad \left(\phi = 0 \wedge \dot{\phi} \geq 0\right) \end{aligned} \tag{2-36}$$

Equation (2-32) can now be written as:

$$\dot{\boldsymbol{\sigma}} = \boldsymbol{E} : \left(\dot{\boldsymbol{\varepsilon}} - \dot{\lambda}\frac{\partial \phi}{\partial \boldsymbol{\sigma}}\right) \tag{2-37}$$

For isotropic hardening the yield stress only depends on the stress and the scalar variable $\dot{\lambda}$ representing the accumulated plastic strain. With the condition that the stress state remains on the yield surface $\dot{\lambda}$ can be determined:

$$\dot{\phi} = 0 \quad \Rightarrow \quad \frac{\partial \phi}{\partial \boldsymbol{\sigma}} : \dot{\boldsymbol{\sigma}} + \frac{\partial \phi}{\partial \lambda}\dot{\lambda} = 0 \tag{2-38}$$

With equation (2-37) is found:

$$\dot{\lambda} = \frac{-\dfrac{\partial \phi}{\partial \boldsymbol{\sigma}} : \boldsymbol{E} : \dot{\boldsymbol{\varepsilon}}}{\dfrac{\partial \phi}{\partial \lambda} - \dfrac{\partial \phi}{\partial \boldsymbol{\sigma}} : \boldsymbol{E} : \dfrac{\partial \phi}{\partial \boldsymbol{\sigma}}} \tag{2-39}$$

So the general constitutive equation for elastic plastic material with isotropic hardening can be written as:

$$\dot{\boldsymbol{\sigma}} = \boldsymbol{E} : \left(\dot{\boldsymbol{\varepsilon}} - \frac{\dfrac{\partial \phi}{\partial \boldsymbol{\sigma}} : \boldsymbol{E} : \dot{\boldsymbol{\varepsilon}}}{\dfrac{\partial \phi}{\partial \lambda} - \dfrac{\partial \phi}{\partial \boldsymbol{\sigma}} : \boldsymbol{E} : \dfrac{\partial \phi}{\partial \boldsymbol{\sigma}}} \frac{\partial \phi}{\partial \boldsymbol{\sigma}}\right) \tag{2-40}$$

Alternatively and a friendlier form:

$$\dot{\boldsymbol{\sigma}} = \left(\boldsymbol{E} - (1-h)\boldsymbol{Y}\right) : \dot{\boldsymbol{\varepsilon}} \tag{2-41}$$

Where $\boldsymbol{Y}$ is the fourth order yield tensor which is independent of the hardening and is written as:

$$\boldsymbol{Y} = \frac{\boldsymbol{E}:\frac{\partial\phi}{\partial\boldsymbol{\sigma}}\frac{\partial\phi}{\partial\boldsymbol{\sigma}}:\boldsymbol{E}}{\frac{\partial\phi}{\partial\boldsymbol{\sigma}}:\boldsymbol{E}:\frac{\partial\phi}{\partial\boldsymbol{\sigma}}} \tag{2-42}$$

The scalar h is the hardening coefficient:

$$h = \frac{\frac{\partial\phi}{\partial\lambda}}{\frac{\partial\phi}{\partial\lambda} - \frac{\partial\phi}{\partial\boldsymbol{\sigma}}:\boldsymbol{E}:\frac{\partial\phi}{\partial\boldsymbol{\sigma}}} \tag{2-43}$$

A general equation, equation (2-41), depending on an arbitrary yield function ϕ is found. This description counts for small deformations. In case of large deformations these deformations are considered as piece wise small deformations [Vreede, 1992]. The only thing to be done is correcting the stresses rate for rotations. This is done by expressing the Jaumann stress rate in terms of the stress rate:

$$\boldsymbol{\sigma}^{\nabla} = \dot{\boldsymbol{\sigma}} - \boldsymbol{W}\cdot\boldsymbol{\sigma} + \boldsymbol{\sigma}\cdot\boldsymbol{W} \tag{2-44}$$

The next step is to find a suitable expression for this yield function. This function strongly depends on which material is to be described. In the next subsections two yield functions are studied which are very useful for sheet metal forming processes.

2.3.1 Hill Yield Function

A yield criterion to describe orthotropic material behaviour is the Hill yield criterion, [Hill, 1950]. This criterion is an extension of the isotropic Von Mises criterion. The Hill yield criterion in its most general form is written as:

$$\begin{aligned} 2\phi(\boldsymbol{\sigma}) &= \tfrac{2}{3}(F+G+H)\sigma_y^2 = F(\sigma_{yy}-\sigma_{zz})^2 + G(\sigma_{zz}-\sigma_{xx})^2 + H(\sigma_{xx}-\sigma_{yy})^2 + \\ &+ 2(L\sigma_{yz}^2 + M\sigma_{xz}^2 + N\sigma_{xy}^2) = 1 \end{aligned} \tag{2-45}$$

The material x-, y- and z-direction coincide with the axes of orthotropy. The parameters F, G, H, L, M and N describe the anisotropy of the material. The constants F, G, and H may be expressed in terms of the yield stresses in tension; the parameters L, M, and N by the yield stresses in pure shear. Equation (2-45) can be rewritten, [Koenis, 1994][Carleer, 1996]

$$\phi = \sqrt{\boldsymbol{\sigma}:\boldsymbol{P}:\boldsymbol{\sigma}} - \sqrt{\tfrac{2}{3}(F+G+H)}\,\sigma_y = 1 \tag{2-46}$$

The last term represents a mean value of the yield stress. The components of the tensor $\boldsymbol{P}$ and the components of the stress tensor σ are written as:

$$\boldsymbol{P}=\begin{bmatrix} G+H & -H & -G & 0 & 0 & 0 \\ -H & F+H & -F & 0 & 0 & 0 \\ -G & -F & F+G & 0 & 0 & 0 \\ 0 & 0 & 0 & 2N & 0 & 0 \\ 0 & 0 & 0 & 0 & 2M & 0 \\ 0 & 0 & 0 & 0 & 0 & 2L \end{bmatrix}; \boldsymbol{\sigma} = \begin{Bmatrix} \sigma_{xx} \\ \sigma_{yy} \\ \sigma_{zz} \\ \sigma_{xy} \\ \sigma_{xz} \\ \sigma_{yz} \end{Bmatrix} \tag{2-47}$$

The derivative of ϕ becomes with the notation of equation (2-46):

$$\frac{\partial \phi}{\partial \boldsymbol{\sigma}} = \frac{\boldsymbol{P}:\boldsymbol{\sigma}}{\sqrt{\boldsymbol{\sigma}:\boldsymbol{P}:\boldsymbol{\sigma}}} \tag{2-48}$$

The next step is to determine the parameters of anisotropy. Concerning metals the rate of plastic deformation satisfies the flow rule (2-35):

$$\dot{\boldsymbol{\varepsilon}}^{p} = \dot{\lambda}\frac{\partial \phi}{\partial \boldsymbol{\sigma}} = \dot{\lambda}\frac{\boldsymbol{P}:\boldsymbol{\sigma}}{\sqrt{\boldsymbol{\sigma}:\boldsymbol{P}:\boldsymbol{\sigma}}} \tag{2-49}$$

Consider a sheet of metal. The x-direction and the y-direction of the sheet coincide with the rolling direction RD and the transverse direction TD respectively. A test specimen is cut out of a sheet, see Figure 2-5(a). The longitudinal direction of the test specimen is inclined under a certain angle θ with the RD. A uni-axial tensile stress σ is applied along the longitudinal axis of the in-plane test specimen, see Figure 2-5(b). During this test the plane stress assumption is valid, $\sigma_{zz} = 0$.

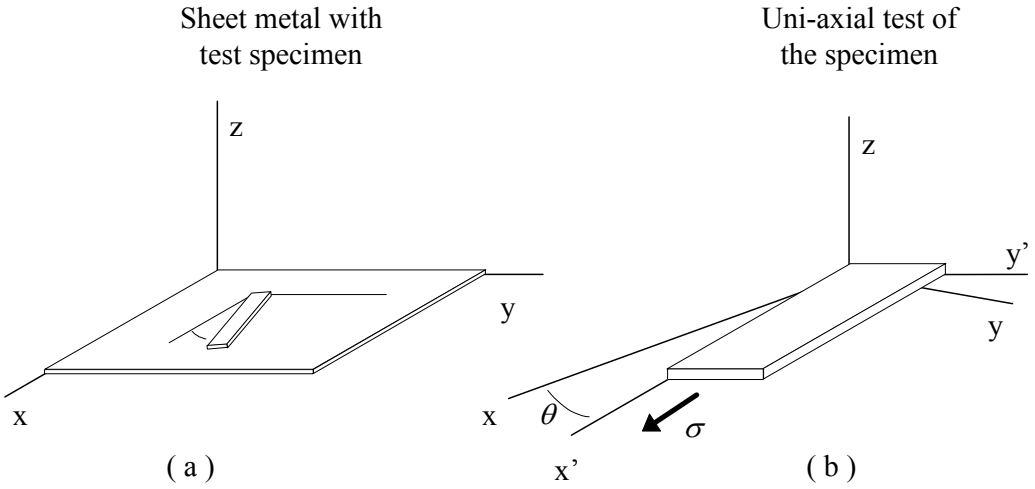

Figure 2-5 *A uni-axial test on a specimen inclined at an angle θ to the material co-ordinates.*

The uni-axial tensile stress can be transformed according to the stresses of the material co-ordinates [Rees, 1994]:

$$\begin{aligned}\sigma_{xx} &= \sigma \cos^2 \theta \\ \sigma_{yy} &= \sigma \sin^2 \theta \\ \sigma_{xy} &= \sigma_{yx} = \tfrac{1}{2}\sigma \sin 2\theta\end{aligned} \tag{2-50}$$

The transformation of the plastic strain increments from the material co-ordinates x, y, and z to the longitudinal and lateral axes x' and y' respectively is found by substitution of equation (2-50) in equation (2-49), see Figure 2-5(b):

$$\begin{aligned}\dot{\varepsilon}^p_{xx} &= \dot{\lambda}\sigma\left((H+G)\cos^4\theta - 2H\sin^2\theta\cos^2\theta + (F+H)\sin^4\theta + \tfrac{1}{2}N\sin^2 2\theta\right) \\ \dot{\varepsilon}^p_{yy} &= \dot{\lambda}\sigma\left((2H+F+G)\sin^2\theta\cos^2\theta - H(\sin^4\theta+\cos^4\theta) + \tfrac{1}{2}N\sin^2 2\theta\right) \\ \dot{\varepsilon}^p_{xy} &= \dot{\lambda}\sigma\left(\tfrac{1}{2}\sin^2\theta\left[(F+H)\sin^2\theta - (H+G)\cos^2\theta\right] + \right. \\ &\qquad \left. + \tfrac{1}{2}H\left[\sin^2\theta\sin 2\theta - \cos^2\theta\cos 2\theta\right] + \tfrac{1}{2}N\sin 2\theta\cos 2\theta\right) \\ \dot{\varepsilon}^p_{zz} &= \dot{\lambda}\sigma\left(G\cos^2\theta + F\sin^2\theta\right)\end{aligned} \tag{2-51}$$

The sheet anisotropy is characterised by the width-to-thickness ratio of the plastic strain increment. The anisotropy parameter R is acquired from equation (2-51):

$$R_\theta = \frac{\dot{\varepsilon}^p_{yy}}{\dot{\varepsilon}^p_{zz}} = -\frac{\left((2H+F+G)\sin^2\theta\cos^2\theta - H(\sin^4\theta+\cos^4\theta) - \tfrac{1}{2}N\sin^2 2\theta\right)}{\left(G\cos^2\theta + F\sin^2\theta\right)} \tag{2-52}$$

In this equation R_θ denotes the R-value for the tensile direction θ to the material 1-direction. Most deep drawing steels show a four earing behaviour. In order to determine the anisotropic material parameters for four earing material, uni-axial tests for $\theta = 0°$, 45° and 90° are required. The material x-direction, $\theta = 0°$, is chosen as the rolling direction. From here the transverse direction, $\theta = 90°$, and the intermediate direction, $\theta = 45°$, are defined. Setting $\theta = 0°$, 45° and 90° in equation (2-52) gives the desired R-values:

$$R_0 = \frac{H}{G} \quad ; \quad R_{45} = \frac{-G-F+2N}{2(G+F)} \quad ; \quad R_{90} = \frac{H}{F} \tag{2-53}$$

By performing three tensile tests the three R-values can be determined. These R-values are sufficient to derive the parameters H, G, F and N since only the ratios between the four parameters are of interest. The four parameters describing the planar anisotropy of the sheet become:

$$H = R_0 \cdot R_{90} \quad ; \quad G = R_{90} \quad ; \quad F = R_0 \quad ; \quad N = (R_{45} + 0.5)(R_0 + R_{90}) \tag{2-54}$$

The two missing parameters M and L can not be determined by a uni-axial test. As the corresponding stresses have minor effect on the sheet metal forming process, the parameters are chosen equal to three corresponding to the isotropic case. In the isotropic case all R-values are equal one. When substituting the six parameters in the yield equation (2-46) the description of the planar anisotropic material is complete.

For graphic presentations the yield criterion is presented on the plane stress space $\sigma_{zz}=0$. This plane stress state usually occurs during sheet metal forming. The yield criterion is presented in principal stresses which means that the shear stresses are absent. Figure 2-6 presents two yield surfaces which describe planar isotropic behaviour, the R-value does not vary with θ. The solid line represents the yield function with an R-value of 1, the Hill yield function degenerates to the Von Mises function. The dotted line represents the yield function with an R-value of 2; the ellipse is more stretched.

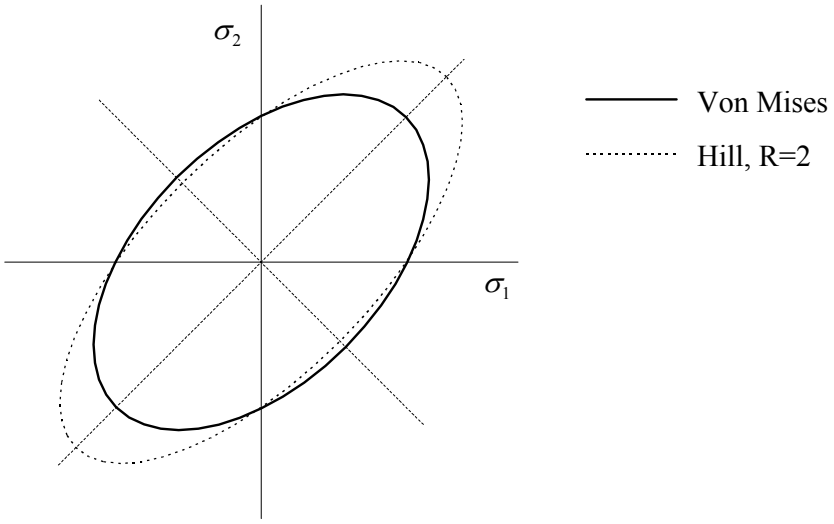

Figure 2-6 *A presentation of the Hill yield function and the Von Mises yield function.*

2.3.2 Vegter Yield Function

The parameters in the Hill yield function are determined with uni-axial tensile tests. This description is not always sufficiently accurate. Experimental information of tests at multi-axial stress states is necessary. Vegter [Vegter, 1995] proposed a description which directly uses the test results at multi-axial stress states. A yield criterion based on the pure shear point, the uni-axial point, the plane strain point and the equi-biaxial point has been developed. These four reference points are represented at the plane stress space of the principal stress space (Figure 2-7).

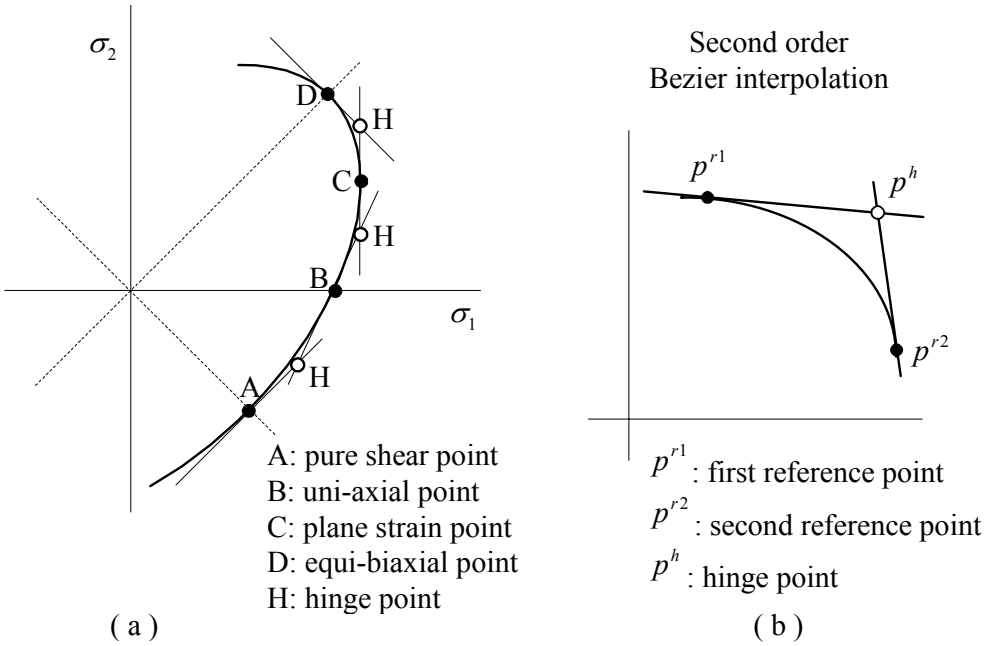

Figure 2-7 *The four reference points to construct the Vegter yield function (a). Second order Bezier interpolation with help of two reference points and one hinge point (b).*

In case of isotropic material behaviour the gradient $d\sigma_2/d\sigma_1$ at the reference points is known. In the uni-axial point the tangent is a function of the R-value, whereas in the other reference points the tangent has a fixed value.
For the uni-axial point the R-value is defined according equation (2-52) and can be expressed in terms of $\dot{\varepsilon}_1$ and $\dot{\varepsilon}_2$ because of the plastic incompressibility:

$$R = \frac{\dot{\varepsilon}_2}{\dot{\varepsilon}_3} = \frac{\dot{\varepsilon}_2}{-\left(\dot{\varepsilon}_1 + \dot{\varepsilon}_2\right)} \tag{2-55}$$

The gradient can be expressed in terms of the strain gradients which in turn can be expressed in terms of the R-value according equation (2-55):

$$\frac{d\sigma_2}{d\sigma_1} = -\frac{\dfrac{\partial \phi}{\partial \sigma_1}}{\dfrac{\partial \phi}{\partial \sigma_2}} = -\frac{\dot{\varepsilon}_1}{\dot{\varepsilon}_2} = \frac{1+R}{R} \tag{2-56}$$

An overview of the gradients in case of isotropic material behaviour is given in Table 2-1.

Reference point	$d\sigma_2 / d\sigma_1$
pure shear	1
uni-axial	$(1+R)/R$
plane strain	∞
equi-biaxial	-1

Table 2-1 *The tangent of the reference points in case of isotropic material behaviour.*

A yield surface is constructed by using the reference points and the gradients. This construction is performed with the help of Bezier interpolations. The hinge points, p^h, between the reference points, p^{r1} and p^{r2}, are defined as the intersection points of the tangents of the respective reference points. Between the reference points a second order Bezier interpolation is used (Figure 2-7):

$$\boldsymbol{\sigma} = (1-\beta)^2 \, \boldsymbol{p}^{r1} + 2\beta(1-\beta)\boldsymbol{p}^h + \beta^2 \boldsymbol{p}^{r2} \tag{2-57}$$

Where β is a scalar increasing from 0 to 1 between the two reference points. For the four reference points, three Bezier interpolations are used to describe a quarter of the yield function. The first between the equi- biaxial point and the plane strain point, the second between the plane strain point and the uni-axial point and the third between the uni-axial point and the pure shear point. This yield function is a multi-faceted yield function. The advantage of using Bezier interpolations is that the normal of the yield function is continuous in the reference points.
The major stresses σ_1 and σ_2 are defined in a way that $\sigma_1 \geq \sigma_2$. So only half a yield surface underneath the line $\sigma_1 = \sigma_2$ is needed. The material is assumed to behave identically under compression as under tension because of the lack of reliable compression tests. So, the yield surface is completed by using symmetry in the line $\sigma_1 = -\sigma_2$. The construction of the yield surface can easily be extended to more points. The only condition is that the tangent must be known in that point. It is obvious that the yield surface must always remain convex.

The stress definition of the yield surface (2-57) is used to develop a yield function ϕ [Pijlman, 1996]. This Vegter yield function is defined as:

$$\phi = \sigma_{bez} - \sigma_y \tag{2-58}$$

Where σ_{bez} is a kind of equivalent stress and σ_y is the yield stress. In order to find a suitable expression for σ_{bez}, equation (2-57) is normalised with σ_{bez}. For both stress components the following expression is found:

$$\begin{aligned} \sigma_1 / \sigma_{bez} &= (1-\beta)^2 \, p_1^{r1} + 2\beta(1-\beta)\, p_1^h + \beta^2 p_1^{r2} \\ \sigma_2 / \sigma_{bez} &= (1-\beta)^2 \, p_2^{r1} + 2\beta(1-\beta)\, p_2^h + \beta^2 p_2^{r2} \end{aligned} \tag{2-59}$$

This results in two expressions for σ_{bez}:

$$\begin{aligned} \sigma_{bez} &= \frac{\sigma_1}{(1-\beta)^2 \, p_1^{r1} + 2\beta(1-\beta)p_1^h + \beta^2 p_1^{r2}} \\ \sigma_{bez} &= \frac{\sigma_2}{(1-\beta)^2 \, p_2^{r1} + 2\beta(1-\beta)p_2^h + \beta^2 p_2^{r2}} \end{aligned} \tag{2-60}$$

With help of these expression a quadratic function for β is found:

$$\beta^2\left(\sigma_2\left(p_1^{r2} - 2p_1^h + p_1^{r1}\right) - \sigma_1\left(p_2^{r2} - 2p_2^h + p_2^{r1}\right)\right) + \\ + \beta\left(2\sigma_2\left(p_1^h - p_1^{r1}\right) - 2\sigma_1\left(p_2^h - p_2^{r1}\right)\right) + \sigma_2 p_1^{r1} - \sigma_1 p_2^{r1} = 0 \tag{2-61}$$

When solving equation (2-61) only one value of β satisfies the boundary condition of lying between 0 and 1. Secondly, an expression for σ_{bez} is found by substituting this value in one of the equations of (2-59).
The yield surface can be described with six Bezier interpolations because of the definition that $\sigma_1 \geq \sigma_2$, see Figure 2-8. The ratio σ_1/σ_2 determines an area where an Bezier interpolation is valid. Depending on the area the reference points and the hinge points are defined. By substitution of the right reference and hinge points into equation (2-59) the yield function can be determined. It must be noticed that σ_{bez} is determined for every Bezier interpolation.

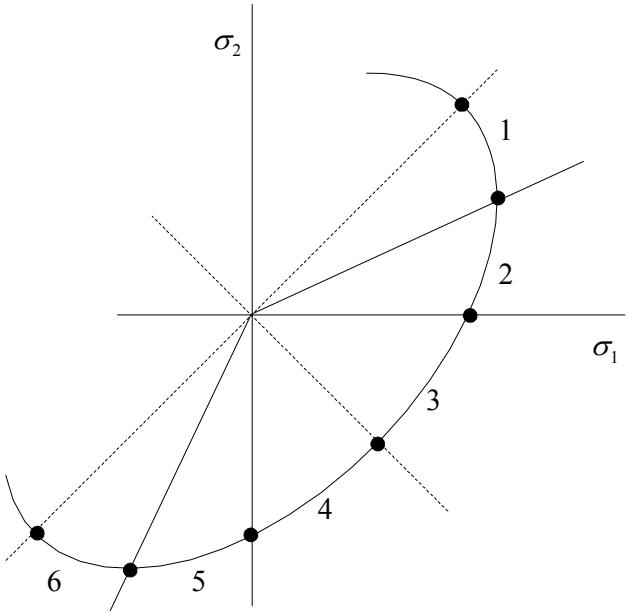

Figure 2-8 *The six areas in the stress space to determine the right Bezier interpolation of the Vegter yield function.*

The four reference points define the yield function. The experiments to obtain the reference points must be performed at various angles with the rolling direction. When the reference points do not vary with the angle, the material behaves planar isotropic. Then the above mentioned description of the yield function is satisfactory. But, when the reference points vary, the material behaves planar anisotropic. In that case the yield function gas to be extended.

When anisotropy is determined, experiments are performed in three directions. These directions are related to the rolling direction and are described by the angle θ. The experiments are performed for $\theta = 0°$, 45° and 90°. This is analogue to the determination

of the Hill yield function, section 2.3. So for each angle θ the reference points and R-value are obtained.

A yield surface for the measured angles θ can be constructed. The first part of the yield surface is constructed by using the measured reference points, the full circles in Figure 2-9. The yield surface can not be completed by simply using symmetry in the line $\sigma_1 = -\sigma_2$. When mirroring the reference points from the first part to the second part the rolling direction shifts 90°. So, for constructing the second part of the yield surface the reference points of the angle θ+90° must be used. The determination of the plane strain point in the second part of the yield surface is illustrated in Figure 2-9. The plane strain point for θ+90° is mirrored in the line $\sigma_1 = -\sigma_2$. The other reference points of the second part are also shown, the open circles in Figure 2-9.

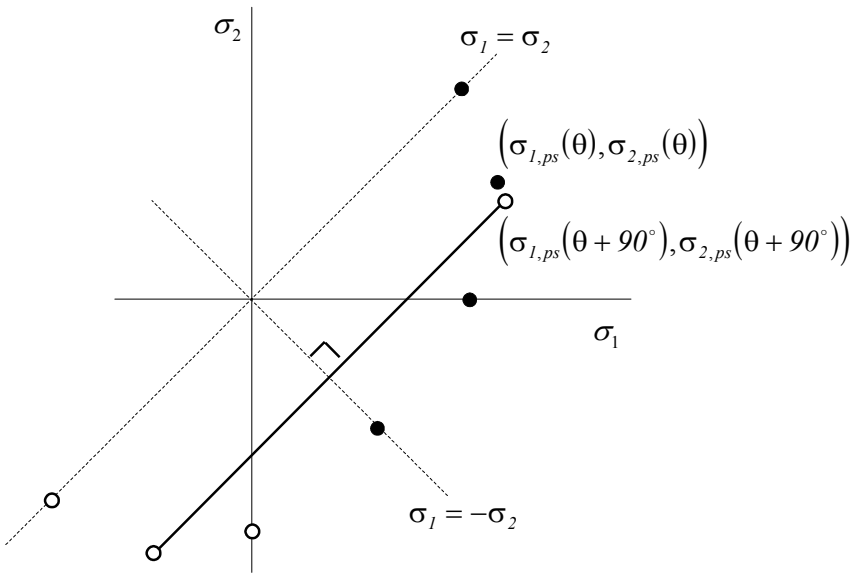

Figure 2-9 *Construction of the reference points for the Vegter yield surface in case of anisotopy.*

The gradients in the reference points also differ from the isotropic case. The stress state does not coincide with the deformation state because of the anisotropy. For example a biaxial stress state results not in a biaxial deformation state. So, the gradient in each reference point must be constructed. This construction is explained for the biaxial point in Figure 2-10.
The gradient in the biaxial point can not be related to measurements. The desire of a smooth yield surface is the basis for the gradient construction. The gradient is constructed with help of the plane strain point. The plane strain point for angle θ is drawn. The plane strain point for the angle θ+90° is mirrored in the line $\sigma_1 = \sigma_2$ The line through this two points is translated to the biaxial point to define the gradient.

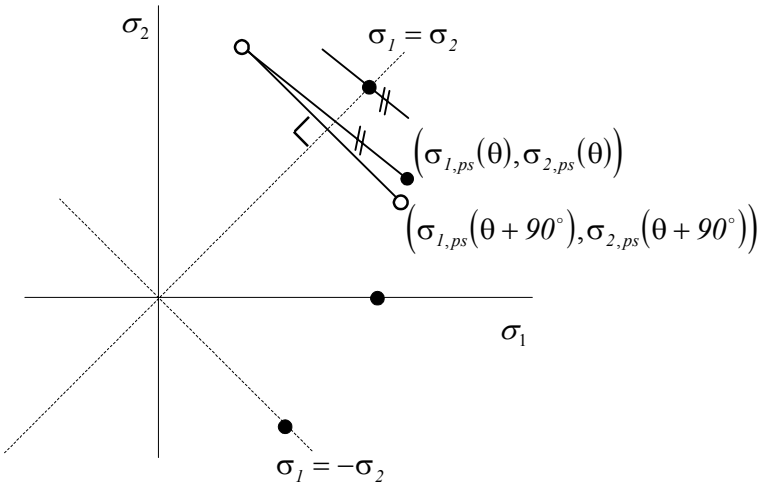

Figure 2-10 *Construction of the gradients for the Vegter yield surface in case of anisotopy.*

The gradient in the plane strain point and in the uni-axial point are similar to the gradients in the isotropic case. The gradient in the pure shear point is constructed with help of the uni-axial points in a similar way as for the bi-axial point. An overview of the tangents in case anisotropic material behaviour is given in Table 2-2.

Reference point	$d\sigma_2 / d\sigma_1$
pure shear	$f\left(\boldsymbol{\sigma}_{un}(\theta), \boldsymbol{\sigma}_{un}\left(\theta + 90^\circ\right)\right)$
uni-axial	$\left(1 + R(\theta)\right) / R(\theta)$
plane strain	∞
equi-biaxial	$g\left(\boldsymbol{\sigma}_{ps}(\theta), \boldsymbol{\sigma}_{ps}\left(\theta + 90^\circ\right)\right)$

Table 2-2 *The tangent of the reference points in case of anisotropic material behaviour.*

For the measured angles, a yield function based on second order Bezier interpolations exists. The yield function for an arbitrary angle can be determined with the help of an interpolation. The corresponding reference points are interpolated as function of the angle θ to obtain a new reference point. With the interpolated reference points a new yield function is constructed.

For this interpolation a suitable interpolation function must be found. The value of a reference point as function of the angle θ is denoted by $\sigma_{test}(\theta)$. The following boundary condition must be fulfilled; the angles $\theta = 0°$ and $\theta = 90°$ are angles of symmetry:

$$\boldsymbol{\sigma}_{test}(\theta) = \boldsymbol{\sigma}_{test}(-\theta)$$
$$\boldsymbol{\sigma}_{test}(90^\circ - \theta) = \boldsymbol{\sigma}_{test}(90^\circ + \theta) \qquad (2\text{-}62)$$

This periodic function can be interpolated with Fourrier series:

$$F(x) = \sum_{n=0}^{\infty} a_n \sin nx + b_n \cos nx$$

For four earing material this condition is met with the following terms of the Fourrier series:

$$\sigma_{test}(\theta) = A + B\cos 2\theta + C\cos 4\theta \tag{2-63}$$

The second boundary condition is rather obvious, the interpolation must correspond with the experimental value $\sigma_{exp,\theta}$:

$$\begin{aligned} \boldsymbol{\sigma}_{test}(\theta = 0^\circ) &= \boldsymbol{\sigma}_{\exp,0} \\ \boldsymbol{\sigma}_{test}(\theta = 45^\circ) &= \boldsymbol{\sigma}_{\exp,45} \\ \boldsymbol{\sigma}_{test}(\theta = 90^\circ) &= \boldsymbol{\sigma}_{\exp,90} \end{aligned} \tag{2-64}$$

Equation (2-63) holds three unknowns which can be solved with the boundary condition (2-64). So, the interpolation function becomes:

$$\begin{aligned} \sigma_{test}(\theta) = {} & \frac{\sigma_{\exp,0} + 2\sigma_{\exp,45} + \sigma_{\exp,90}}{4} + \frac{\sigma_{\exp,0} - \sigma_{\exp,90}}{2}\cos 2\theta + \\ & + \frac{\sigma_{\exp,0} - 2\sigma_{\exp,45} + \sigma_{\exp,90}}{4}\cos 4\theta \end{aligned} \tag{2-65}$$

With equation (2-65) it is possible to determine the reference points for arbitrary angles θ. With these reference points a Vegter yield function can be constructed. In Table 2-3 an example of the interpolation is given. A row represents a reference point or the R-value. The reference points are normalised by a mean yield stress. The columns $\theta = 0°$, 45° and 90° represent the experimentally obtained values of the reference points and the R-value. The R-value must be interpolated to determine the tangent in the uni-axial point. With equation (2-65) the values for an angle of 30° with the rolling direction are derived. With the values printed in the last column, $\theta = 30°$, the corresponding yield function can be constructed.

Experimental value	0°	45°	90°	$\theta = 30^\circ$
$\sigma_{pure\,shear}$	0.60	0.60	0.60	0.60
$\sigma_{uni-axial}$	0.90	1.10	1.00	1.04
$\sigma_{plane\,strain}$	1.10	1.25	1.15	1.21
$\sigma_{equi-biaxial}$	1.00	1.00	1.00	1.00
R-value	0.50	2.00	1.00	1.56

Table 2-3 *The reference points and the R-values obtained from experiments (arbitrary normalised values) with interpolated values for* $\theta = 30°$.

2.4 Concluding Remarks

In this chapter the field of the continuum mechanics is discussed. The strains as well as the stresses appearing in a body under deformation are treated. An important factor in the description of the material behaviour is the constitutive equation, it connects the stresses and the strains. In case of elastic behaviour the constitutive equation is rather simple. When plastic deformation occurs, the constitutive equation becomes more complex and a yield function must be defined. Two yield functions useful in sheet metal forming are treated. The classic Hill yield function and the newly developed Vegter yield function.

2.5 Reference

[Besseling, 1994]
Besseling J.F., E. van der Giessen, *Mathematical Modelling of Inelastic Deformation*, R.J. Knops & K.W. Morton (eds.), Chapman & Hall, 1994

[Betten, 1993]
Betten J., *Kontinuumsmechanik*, Springer Verlag, Berlin, 1993

[Carleer, 1996]
Carleer B.D., A.H.Streppel, P.T.G. Koenis, J. Huétink, *The analysis of planar anisotropic sheet metal*, Sheet metal 1996,. H. J. J. Kals, et al. (eds.), 1996

[Hill, 1950]
Hill R, *The mathematical theory of Plasticity,* Clarendon Press, Oxford, 1950

[Huétink, 1986]
Huétink J., *On the numerical simulations of thermo mechanical forming processes*, PhD-thesis, University of Twente, 1986

[Koenis, 1994]
Koenis P. T. G., *Finite element simulations of 3-D sheet metal forming processes*, Report TM-963, University of Twente, 1994

[Pijlman, 1996]
Pijlman H.H., *Implementation of the Vegter yield criterion in the finite element program DIEKA*, Graduate report, University of Twente, 1996

[Rees, 1994]
Rees D.W.A., *Equivalence and instability correlations for isotropic and anisotropic sheet plasticity*, J. of Mat. Proc. Tech., 40, 1994

[Vegter, 1995]
Vegter H., P. Drent, J. Huétink, *A planar isotropic yield criterion based on mechanical testing at multi-axial stress states,* Simulation of materials processing: theory, methods and applications, S. F. Shen & P. Dawson (eds.), Balkema, Rotterdam, 1995

[Vreede, 1992]
Vreede P. T., *A finite elements method for simulations of 3-dimensional sheet metal forming*, PhD-thesis, University of Twente, 1992

3. Finite Element Formulation

Often problems are so complex that it is impossible to create the solution at once. A strategy to solve these problems is to divide them into smaller parts and by solving these smaller parts to create a solution of the whole complex problem.
An example of this strategy is the standard discrete system. The problem is divided into a finite number of well defined components. In the first section of this chapter an example of a standard discrete system is given. When the problem does not exist of well defined components, the system is called continuous. This system is divided into a number of elements. For every element a relative simple set of equations can be defined. Combining all the elements with their equations leads to a number of algebraic equations describing the behaviour of the system. A finite element formulation for numerical simulations of forming processes is given in the section 3.1 to 3.4.
The interest of this work lies in deep drawing simulations. Suitable elements for this kind of simulations are plate elements. In section 3.5, three different types of plate elements are discussed. In order to give information on the element performance a few tests are performed. In section 3.6 elastic tests are discussed whereas in section 3.7 plastic tests are discussed.

3.1 Standard Discrete System

To explain the standard discrete system a structure built up from linear lastic modules is considered (Figure 3-1a). The modules denoted by bold numbers are connected at the nodes, denoted by regular numbers. At node 2 an external load is prescribed. The following procedure is used to solve the displacement of every node and the internal force of every module [Zienkiewicz, 1977].

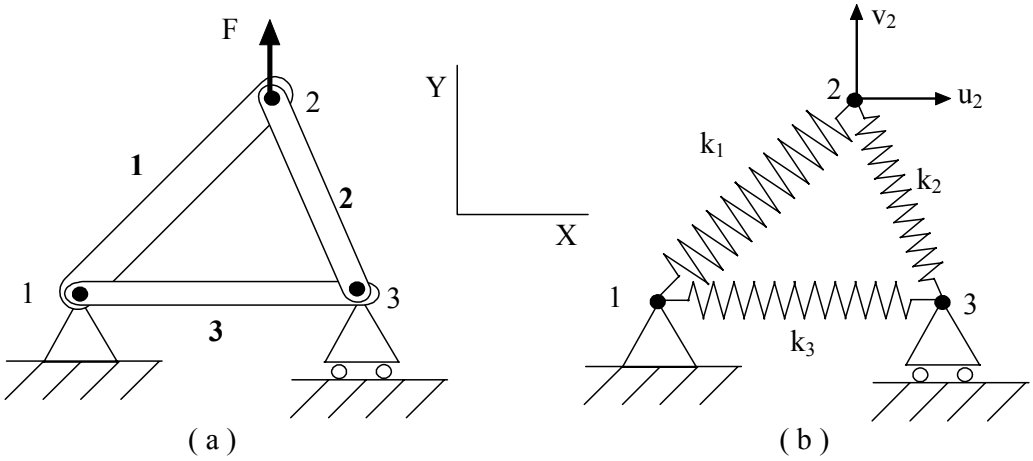

Figure 3-1 *A structure built up of three modules (a). The modules can be presented as springs (b).*

For every node *n* a displacement vector $\boldsymbol{u}_n$ is defined:

$$\boldsymbol{u}_n = \begin{Bmatrix} u_n \\ v_n \end{Bmatrix} \tag{3-1}$$

A force vector $\boldsymbol{f}_n$ is defined:

$$\boldsymbol{f}_n = \begin{Bmatrix} U_n \\ V_n \end{Bmatrix} \tag{3-2}$$

The modules behave linear elastic. Therefore they can be denoted as linear springs with stiffness k_i (Figure 3-1b). The characteristic behaviour of the modules is of the form:

$$\boldsymbol{K}^c \cdot \boldsymbol{u}^c = \boldsymbol{f}^c \tag{3-3}$$

In which $\boldsymbol{K}^c$ represents the stiffness of the module, $\boldsymbol{u}^c$ represents the nodal displacements and $\boldsymbol{f}^c$ represents the nodal forces. Depending on the orientation of the module in the global co-ordinate system the elements of $\boldsymbol{K}^c$ are expressed in terms of the stiffness k_i. For every module of the structure such a characteristic behaviour can be set up.
In order to find the solution of the whole structure the different modules must be brought together. The characteristic behaviour of each module is assembled to obtain the behaviour of the whole structure. Two conditions must met to obtain the complete solution:

- displacement compatibility
- equilibrium

The first condition is met automatically by defining a nodal vector $\boldsymbol{u}$ in which all the modules of the structure participate
To obtain equilibrium, it is necessary to establish equilibrium at the nodes of the structure. Therefore the force vector $\boldsymbol{f}$ is defined which contains all the nodal forces. To establish equilibrium, each element of $\boldsymbol{f}$ must be equal to the sum of the nodal forces:

$$f_n = \sum_{c=1}^{m} f_n^c \tag{3-4}$$

In which f_n^c is the force contributed to node n by module c. The summation only concerns the modules which contribute to node n. Substitution of equation (3-3) into equation (3-4), the force contribution to node n is:

$$f_n = \sum_{c=1}^{m} K_n^c \, u_n^c \tag{3-5}$$

For every node n equation (3-5) is assembled. This assembly gives the following equation for the entire system:

$$\boldsymbol{K} \cdot \boldsymbol{u} = \boldsymbol{f} \tag{3-6}$$

Where $\boldsymbol{K}$ is the stiffness matrix of the structure, $\boldsymbol{u}$ is the vector with the nodal displacements and $\boldsymbol{f}$ is the vector with the nodal forces. This general assembly process can be found to be the common and fundamental feature of all finite element calculations.

The system of equations can be solved when the boundary conditions have been substituted. There is always a need for a minimum number of boundary conditions in order to prevent rigid body motions. Without these boundary conditions is it impossible to solve the system. For this discrete system the displacement in X- and Y-direction are suppressed for node 1 and the displacement in Y-direction for node 3. In node 2 a load F in Y-direction is prescribed. So, the boundary conditions are:

$$\begin{aligned} u_1 = v_1 = v_3 = 0 \\ V_2 = F \end{aligned} \qquad (3\text{-}7)$$

When substituting the boundary conditions into equation (3-6) the system can be solved. The nodal displacements and the internal forces in each module can be obtained.

3.2 Virtual Power

A system is divided into a number of elements when it does not exists out of well defined components (Figure 3-2). For every element an element stiffness matrix is obtained. The element matrices are assembled into a system matrix. The basic equations describing the forming process have been given in chapter two.
The finite element method is applied to solve the differential equations of the forming process. The area of the sheet is divided into a finite number of elements and the equilibrium equations within every element are solved approximately, whereas the constitutive equations and compatibility equations are satisfied exactly, [Huétink, 1986], [Vreede, 1992].

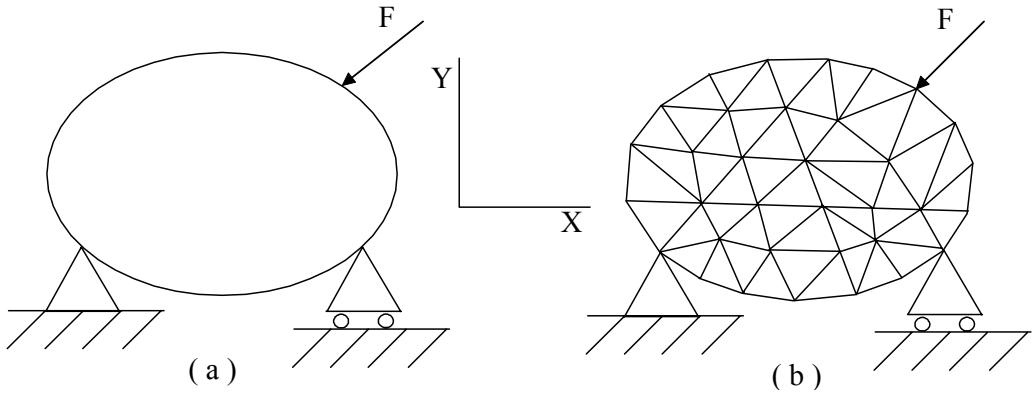

Figure 3-2 *A system which does not exist out of well defined components (a) is divided into elements (b).*

Mechanical equilibrium in a volume V and on a surface S is considered:

$$\begin{aligned} &\nabla \cdot \boldsymbol{\sigma} + \rho \boldsymbol{f} = \boldsymbol{0} \quad \text{in} V \\ &\boldsymbol{n} \cdot \boldsymbol{\sigma} - \boldsymbol{t} = \boldsymbol{0} \quad \text{on} S \end{aligned} \tag{3-8}$$

Where $\boldsymbol{f}$ represents a body force per unit mass and ρ represents the mass density. The surface traction per unit outer surface $\boldsymbol{t}$ can be neglected because they can be expressed in body forces. Inertia is not taken into account. The mechanical equilibrium equations can be written in the weak formulation:

$$\delta W = -\int_V \delta \boldsymbol{v} \cdot \left(\vec{\nabla} \cdot \boldsymbol{\sigma} + \rho \boldsymbol{f} \right) dV + \int_S \delta \boldsymbol{v} \cdot (\boldsymbol{n} \cdot \boldsymbol{\sigma}) dS = 0 \quad \forall \delta \boldsymbol{v} \tag{3-9}$$

Where $\delta \boldsymbol{v}$ is called the virtual velocity and $\boldsymbol{n}$ represents the outward normal vector of the surface.

The first term of equation (3-9) transforms by using the divergence theorem. The weak form, equation (3-9), becomes:

$$\delta W = \int_V \left(\vec{\nabla} \delta \boldsymbol{v} : \boldsymbol{\sigma} - \delta \boldsymbol{v} \cdot \rho \boldsymbol{f} \right) dV = 0 \quad \text{for any } \delta \boldsymbol{v} \tag{3-10}$$

Equation (3-10) is known as the virtual power equation. The stress tensor cannot directly be eliminated because the constitutive equation is an expression for the stress rate, not for the total stress. A weak formulation containing the stress rate is obtained from the equilibrium equation by considering the material rate of change of (3-10) and require that the resulting expression vanishes for any time dependent virtual velocity field. By applying equation (2-16) is found:

$$\begin{aligned} \delta \dot{W} = &\int_V \left(\left(\vec{\nabla} \delta \boldsymbol{v} \right)^{\cdot} : \boldsymbol{\sigma} + \vec{\nabla} \delta \boldsymbol{v} : \dot{\boldsymbol{\sigma}} - \delta \dot{\boldsymbol{v}} \cdot \rho \boldsymbol{f} - \delta \boldsymbol{v} \cdot \left(\rho \boldsymbol{f} \right)^{\cdot} \right) dV + \\ &\int_V \left(\vec{\nabla} \delta \boldsymbol{v} : \boldsymbol{\sigma} - \delta \boldsymbol{v} \cdot \rho \boldsymbol{f} \right) \vec{\nabla} \cdot \delta \boldsymbol{v} \, dV = 0 \end{aligned} \tag{3-11}$$

The material rate of change of the gradient of the virtual velocity can be written as:

$$\left(\vec{\nabla} \delta \boldsymbol{v} \right)^{\cdot} = \vec{\nabla} \delta \dot{\boldsymbol{v}} - \vec{\nabla} \boldsymbol{v} \cdot \vec{\nabla} \delta \boldsymbol{v} \tag{3-12}$$

Substituting equation (3-12) into equation (3-11) and separating the terms containing $\delta \boldsymbol{v}$ and $\delta \dot{\boldsymbol{v}}$ the following equation is found:

$$\begin{aligned} \delta \dot{W} = &\int_V \left(\vec{\nabla} \delta \boldsymbol{v} : \dot{\boldsymbol{\sigma}} - \left(\vec{\nabla} \boldsymbol{v} \cdot \vec{\nabla} \delta \boldsymbol{v} \right) : \boldsymbol{\sigma} + \vec{\nabla} \delta \boldsymbol{v} : \boldsymbol{\sigma} \vec{\nabla} \cdot \boldsymbol{v} \right) dV + \\ &- \int_V \left(\delta \boldsymbol{v} \cdot \left(\rho \boldsymbol{f} \right)^{\cdot} + \delta \boldsymbol{v} \cdot \rho \boldsymbol{f} \vec{\nabla} \cdot \boldsymbol{v} \right) dV + \\ &- \int_V \left(\vec{\nabla} \delta \dot{\boldsymbol{v}} : \boldsymbol{\sigma} - \delta \dot{\boldsymbol{v}} \cdot \rho \boldsymbol{f} \right) dV = 0 \end{aligned} \tag{3-13}$$

Because of equation (3-10) the terms containing $\delta\dot{\boldsymbol{v}}$ vanish. Substituting the expression for the Jaumann rate into equation (3-13) gives:

$$\delta\dot{W} = \int_V \left(\vec{\nabla}\delta\boldsymbol{v} : \boldsymbol{L} : \boldsymbol{D} + \vec{\nabla}\delta\boldsymbol{v} : \left(\boldsymbol{W}\cdot\boldsymbol{\sigma} - \boldsymbol{\sigma}\cdot\boldsymbol{W}\right) - \left(\vec{\nabla}\boldsymbol{v}\cdot\vec{\nabla}\delta\boldsymbol{v}\right) : \boldsymbol{\sigma} + \vec{\nabla}\delta\boldsymbol{v} : \boldsymbol{\sigma}\vec{\nabla}\cdot\boldsymbol{v}\right) dV + \tag{3-14}$$
$$- \int_V \left(\delta\boldsymbol{v}\cdot\left(\rho\boldsymbol{f}\right)^{\cdot} + \delta\boldsymbol{v}\cdot\rho\boldsymbol{f}\vec{\nabla}\cdot\boldsymbol{v}\right) dV = 0$$

In metal forming, the density changes are very small compared to the deformation rate. For that reason the terms containing $\vec{\nabla}\cdot\boldsymbol{v}$ can be neglected.
The virtual rate of deformation tensor is defined:

$$\delta\boldsymbol{D} = \tfrac{1}{2}\left(\delta\boldsymbol{v}\overleftarrow{\nabla} + \vec{\nabla}\delta\boldsymbol{v}\right) \tag{3-15}$$

The first integral of equation (3-14) can be rewritten and with the notation of equation (3-15) the following equation is found:

$$\delta\dot{W} = \int_V \left(\delta\boldsymbol{D} : \boldsymbol{C} : \boldsymbol{D} - 2\left(\delta\boldsymbol{D}\cdot\boldsymbol{D}\right) : \boldsymbol{\sigma} + \left(\vec{\nabla}\delta\boldsymbol{v}\cdot\boldsymbol{v}\overleftarrow{\nabla}\right) : \boldsymbol{\sigma}\right) dV + \tag{3-16}$$
$$- \int_V \left(\rho\delta\boldsymbol{v}\cdot\dot{\boldsymbol{f}}\right) dV = 0$$

3.3 Finite Element Discretization

The volume of integration is divided into a finite number of elements. In the present study isoparametric elements are used. A characteristic of these elements is that the same rule is applied to interpolate both the geometry and the independent field variables between the values in the nodes:

$$\boldsymbol{x} = \sum_n \Psi^n \boldsymbol{x}^n$$
$$\boldsymbol{v} = \sum_n \Psi^n \boldsymbol{v}^n \quad \text{and} \quad \delta\boldsymbol{v} = \sum_n \Psi^n \delta\boldsymbol{v}^n \tag{3-17}$$

Here Ψ^n is the interpolation function related to the nodal point *n*. The interpolation function depends on the local natural co-ordinates. The gradients of the velocity and of the virtual velocity are, respectively:

$$\vec{\nabla}\boldsymbol{v} = \sum_n \vec{\nabla}\Psi^n \boldsymbol{v}^n \quad \text{and} \quad \vec{\nabla}\delta\boldsymbol{v} = \sum_n \vec{\nabla}\Psi^n \delta\boldsymbol{v}^n \tag{3-18}$$

The rate of the deformation tensor can be written as:

$$\boldsymbol{D} = \sum_n \boldsymbol{B}^n \cdot \boldsymbol{v}^n \tag{3-19}$$

Where $\boldsymbol{B}^n$ is a third order tensor depending on the interpolation function. For the virtual deformation relation an equation similar to equation (3-19) holds:

$$\delta \boldsymbol{D} = \sum_n \boldsymbol{B}^n \cdot \delta \boldsymbol{v}^n = \sum_n \delta \boldsymbol{v}^n \cdot \boldsymbol{B}^{*n} \tag{3-20}$$

Where $\boldsymbol{B}^{*n}$ is also a third order tensor depending on the interpolation function. Substitution of equations (3-17) to (3-20) in equation (3-16), gives:

$$\delta \dot{\boldsymbol{W}} = \sum_{m,n} \left(\delta \boldsymbol{v}^{\boldsymbol{m}} \cdot \left(\boldsymbol{K}^{\boldsymbol{mn}} \right) \cdot \boldsymbol{v}^{\boldsymbol{n}} \right) - \sum_m \delta \boldsymbol{v}^{\boldsymbol{m}} \cdot \dot{\boldsymbol{f}}^{\boldsymbol{m}} = 0 \tag{3-21}$$

Where:

$$\boldsymbol{K}^{\boldsymbol{mn}} = \int_V \left(\boldsymbol{B}^{*m} : (\boldsymbol{C} - \boldsymbol{H} \cdot \boldsymbol{\sigma} - \boldsymbol{\sigma} \cdot \boldsymbol{H}) : \boldsymbol{B}^n \right) dV + \int_V \left(\boldsymbol{I} \left(\vec{\nabla} \Psi^{\boldsymbol{m}} \cdot \boldsymbol{\sigma} \cdot \vec{\nabla} \Psi^{\boldsymbol{n}} \right) \right) dV \tag{3-22}$$

With $\boldsymbol{H}$ and $\boldsymbol{I}$ the fourth and second order unity tensor.

And:

$$\dot{\boldsymbol{f}}^{\boldsymbol{m}} = \int_V \left(\Psi^m \rho \dot{\boldsymbol{f}} \right) dV \tag{3-23}$$

All nodal degrees of freedom can be regarded as a multi dimensional vector $\dot{\boldsymbol{u}}$. The requirement that equation (3-21) vanishes for all values of $\delta \boldsymbol{v}$ results in a set of linear algebraic equations for the components of $\dot{\boldsymbol{u}}$ which is formally written as:

$$\boldsymbol{K} \cdot \dot{\boldsymbol{u}} - \dot{\boldsymbol{f}} = \boldsymbol{0} \quad \text{or} \quad \boldsymbol{K} \cdot \dot{\boldsymbol{u}} = \dot{\boldsymbol{f}} \tag{3-24}$$

This equation looks similar to equation (3-6) for the standard discrete system.

3.4 Incremental Formulation

The nodal velocity rates can be solved from equation (3-24). However, not only the current velocity is of interest but the history of the process as well. Therefore an incremental procedure is used. During a time increment Δt the velocity is approximated as being constant. The displacement increments are given by:

$$\Delta \boldsymbol{u} = \hat{\boldsymbol{v}} \Delta \boldsymbol{t} \tag{3-25}$$

Where $\hat{\boldsymbol{v}}$ is the average velocity during the time increment. Equation (3-24) becomes:

$$\hat{\boldsymbol{K}} \cdot \Delta \boldsymbol{u} = \Delta \boldsymbol{f} \tag{3-26}$$

The circumflex indicates that the average values are taken during the time increment. These average values are not known yet. A first approximation is found by the known state at the start of an increment. The displacement increments are predicted by the solution of:

$$\boldsymbol{K}^{\boldsymbol{0}} \cdot \Delta \boldsymbol{u}^{1} = \Delta \boldsymbol{f} \tag{3-27}$$

From the solved displacement increments of the nodal points, the average deformation rate in the integration points is calculated with the help of equation (3-19):

$$\hat{\boldsymbol{D}} = \left(\sum_{n} \boldsymbol{B} \cdot \Delta \boldsymbol{u}^{n} \right) \frac{1}{\Delta t} \tag{3-28}$$

The stresses are calculated by numerical integration of the constitutive equation under assumption that the rate of deformation is constant during the increment.

From the stresses in the integration points the nodal point reaction forces can be calculated:

$$\boldsymbol{R}^{m} = \int_{V} \left(\boldsymbol{B}^{*m} : \boldsymbol{\sigma} \right) dV \tag{3-29}$$

These reaction forces are generally not in equilibrium with the prescribed nodal point forces $\boldsymbol{f}^{m}$ The residual is denoted as the mechanical unbalance ratio:

$$R^{f} = \frac{\left\| \boldsymbol{f}^{m} - \boldsymbol{R}^{m} \right\|}{\left\| \boldsymbol{R}^{m} \right\|} \tag{3-30}$$

The mechanical unbalance ratio is a measure for the accuracy of the calculated increment. If it is not sufficiently small, the displacement increment is recalculated in an iteration process. The increments after the i^{th} iteration can be written as:

$$\Delta \boldsymbol{u}^{i} = \Delta \boldsymbol{u}^{i-1} + \Delta\Delta \boldsymbol{u}^{i} \tag{3-31}$$

Where $\Delta\Delta \boldsymbol{u}^{i}$ is found by solving:

$$\boldsymbol{K}^{i-1} \cdot \Delta\Delta \boldsymbol{u}^{i} = \left(\boldsymbol{f} - \boldsymbol{R}^{i-1} \right) \tag{3-32}$$

The stresses, the mechanical work and the nodal reaction forces are recalculated with the new increment $\Delta \boldsymbol{u}^{i}$. The iteration process stops if the unbalance ratio is sufficiently small. The acceptable unbalance ratio depends on the type of the problem that is being analysed.

3.5 Sheet model

In the previous sections a general finite element formulation was given. Depending on the kind of problem, different kind of elements can be used. Structures with a very small thickness compared to their other dimensions are often described by plate elements. The idea of the plate theory is that the geometry of the sheet is described by only using variables on the mid-plane. The thickness of the sheet is denoted by *h*. The mid-plane is situated in the local xy-plane; the local z-axis is normal to the mid-plane (Figure 3-3).

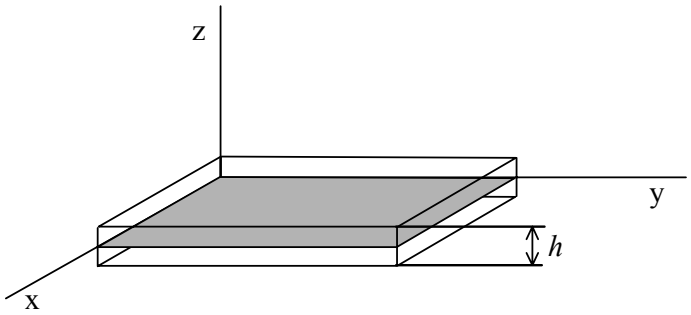

Figure 3-3 *The local co-ordinate system of a plate element with thickness h. The mid-plane is accentuated.*

A material point of the plate can be represented as the sum of a vector to a point in the mid-plane and a vector normal to the plane. This is written as:

$$\mathbf{r} = \mathbf{r}^{0} + z\,\mathbf{n} \quad ; \quad -\frac{h}{2} \le z \le \frac{h}{2} \tag{3-33}$$

With: $\mathbf{r}$: vector to the material point
$\mathbf{r}^{0}$: vector to the material point in the mid-plane
z : distance perpendicular to the mid-plane
$\mathbf{n}$: normal vector
h : sheet thickness

When analysing a structure, the plate element is arbitrarily orientated in the 3D space. Therefore a transformation from the local co-ordinate system to the global co-ordinate system is necessary. The relation between the two systems is given by:

$$\boldsymbol{x}_{loc} = \boldsymbol{R}\,\boldsymbol{x}_{glob} \tag{3-34}$$

Where $\boldsymbol{R}$ is an orthogonal matrix.

For the plate, the stress in normal direction is negligibly small compared to the other stresses. Therefore this stress is assumed to remain zero. As result the state of stress is two dimensional and is called plane stress. Three different plate deformation theories are distinguished. These theories are:

- membrane theory
- Kirchhoff theory
- Mindlin theory

For sake of convenience, the description is restricted to small elastic deformations. For the extension to plastic deformations the kinematic description holds if the strains and the displacements are regarded as small increments.

The membrane theory

The membrane theory assumes that the bending and shear stiffness can be neglected compared to the membrane stiffness. This is true when the plate is thin compared to the curvature. Because of the small curvature in the membrane element, the displacements in the entire element are approximated by the displacement of the mid-plane:

$$\begin{Bmatrix} u \\ v \\ w \end{Bmatrix} = \begin{Bmatrix} u_0(x,y) \\ v_0(x,y) \\ w_0(x,y) \end{Bmatrix} \tag{3-35}$$

The strain field becomes:

$$\begin{Bmatrix} \varepsilon_{xx} \\ \varepsilon_{yy} \\ \varepsilon_{zz} \\ \gamma_{xy} \\ \gamma_{xz} \\ \gamma_{yz} \end{Bmatrix} = \begin{Bmatrix} u_{0,x} \\ v_{0,y} \\ f(\varepsilon_{xx}, \varepsilon_{yy}) \\ u_{0,y} + v_{0,x} \\ 0 \\ 0 \end{Bmatrix} \tag{3-36}$$

The thickness strain cannot be derived from the kinematic relations. This component is derived from the in-plane strain components using the constitutive relations. In the elastic state the plane stress state gives:

$$\varepsilon_{zz} = -\frac{\nu}{(1-\nu)}(\varepsilon_{xx} + \varepsilon_{yy}) \tag{3-37}$$

With ν : Poisson's ratio

In the plastic state the incompressibility condition is valid:

$$\varepsilon_{zz} = -\varepsilon_{xx} - \varepsilon_{yy} \tag{3-38}$$

In elastic-plastic calculations the thickness strain is calculated using the elastic and the plastic strain component.

The Kirchhoff theory

The Kirchhoff theory takes into account the bending stiffness. Points on the normal to the mid-plane remain on that normal after deformation, see Figure 3-4a. The displacements according to the Kirchhoff theory are expressed below as:

$$\begin{Bmatrix} u \\ v \\ w \end{Bmatrix} = \begin{Bmatrix} u_0(x,y) \\ v_0(x,y) \\ w_0(x,y) \end{Bmatrix} + z \begin{Bmatrix} \theta_y \\ -\theta_x \\ 0 \end{Bmatrix} \tag{3-39}$$

Where u_0, v_0 and w_0 are the displacements of the mid-plane and where θ_x and θ_y are the rotations of the normal about the x- and y-axis, respectively. The strains are listed below:

$$\begin{Bmatrix} \varepsilon_{xx} \\ \varepsilon_{yy} \\ \varepsilon_{zz} \\ \gamma_{xy} \\ \gamma_{xz} \\ \gamma_{yz} \end{Bmatrix} = \begin{Bmatrix} u_{0,x} \\ v_{0,y} \\ f(\varepsilon_{xx}, \varepsilon_{yy}) \\ u_{0,y} + v_{0,x} \\ w_{0,x} + \theta_y \\ w_{0,y} - \theta_x \end{Bmatrix} + z \begin{Bmatrix} \theta_{y,x} \\ -\theta_{x,y} \\ 0 \\ \theta_{y,y} - \theta_{x,x} \\ 0 \\ 0 \end{Bmatrix} \tag{3-40}$$

The thickness strain is again derived from the constitutive equations. The shear deformation in the normal direction of the plate must be zero, see Figure 3-4(a). This shear deformation is defined as follows:

$$\begin{Bmatrix} \gamma_{xz} \\ \gamma_{yz} \end{Bmatrix} = \begin{Bmatrix} w_{0,x} + \theta_y \\ w_{0,y} - \theta_x \end{Bmatrix} = \begin{Bmatrix} 0 \\ 0 \end{Bmatrix} \tag{3-41}$$

This formula is called the Kirchhoff constraint. The rotations θ_x and θ_y are coupled with the derivative of the displacement w_0:

$$\begin{aligned} w_{0,x} &= -\theta_y \\ w_{0,y} &= \theta_x \end{aligned} \tag{3-42}$$

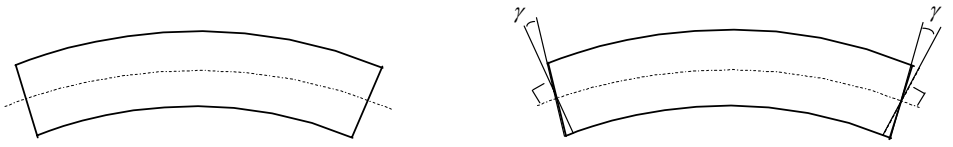

Kirchhoff deformation Mindlin deformation

(a) Pure bending (b)

Figure 3-4 *A plate under pure bending according to the Kirchhoff theory (a) and according to the Mindlin theory (b).*

The Mindlin theory

The Mindlin theory takes into account both the bending and the shear stiffness. The points on the normal to the mid-plane remain on a straight line after deformation, but this

straight line does not necessary remain normal to the mid plane, see Figure 3-4b. The displacements and the strain field according to the Mindlin theory are identical to those of the Kirchhoff theory, equation (3-39) and equation (3-40) respectively.

Summarising the strain field for the plate deformation theories, it can be split in a membrane part, a bending part and a shear part respectively:

$$\begin{Bmatrix} \varepsilon_{xx} \\ \varepsilon_{yy} \\ \varepsilon_{zz} \\ \gamma_{xy} \\ \gamma_{xz} \\ \gamma_{yz} \end{Bmatrix} = \begin{Bmatrix} u_{0,x} \\ v_{0,y} \\ f\left(\varepsilon_{xx}, \varepsilon_{yy}\right) \\ u_{0,y} + v_{0,x} \\ 0 \\ 0 \end{Bmatrix} + z \begin{Bmatrix} \theta_{y,x} \\ -\theta_{x,y} \\ 0 \\ \theta_{y,y} - \theta_{x,x} \\ 0 \\ 0 \end{Bmatrix} + \begin{Bmatrix} 0 \\ 0 \\ 0 \\ 0 \\ w_{0,x} + \theta_y \\ w_{0,y} - \theta_x \end{Bmatrix} \tag{3-43}$$

In short notation:

$$\boldsymbol{\varepsilon} = \boldsymbol{\eta} + z\boldsymbol{\kappa} + \boldsymbol{\gamma} \tag{3-44}$$

Integrating the stresses gives the following resultants, for the membrane forces:

$$N_{xx} = \int_{-\frac{h}{2}}^{\frac{h}{2}} \sigma_{xx} dz \quad ; \quad N_{yy} = \int_{-\frac{h}{2}}^{\frac{h}{2}} \sigma_{yy} dz \quad ; \quad N_{xy} = \int_{-\frac{h}{2}}^{\frac{h}{2}} \sigma_{xy} dz \tag{3-45}$$

For the bending moments:

$$M_{xx} = \int_{-\frac{h}{2}}^{\frac{h}{2}} z\sigma_{xx} dz \quad ; \quad M_{yy} = \int_{-\frac{h}{2}}^{\frac{h}{2}} z\sigma_{yy} dz \quad ; \quad M_{xy} = \int_{-\frac{h}{2}}^{\frac{h}{2}} z\sigma_{xy} dz \tag{3-46}$$

And for the transverse shear forces:

$$S_x = \int_{-\frac{h}{2}}^{\frac{h}{2}} \sigma_{xz} dz \quad ; \quad S_y = \int_{-\frac{h}{2}}^{\frac{h}{2}} \sigma_{yz} dz \tag{3-47}$$

The plate equilibrium equations are expressed as follows:

$$\begin{aligned} N_{xx,x} + N_{xy,y} &= 0 \\ N_{xy,x} + N_{yy,y} &= 0 \end{aligned} \tag{3-48}$$

$$M_{xx,x} + M_{xy,y} - S_x = 0$$
$$M_{xy,x} + M_{yy,y} - S_y = 0 \tag{3-49}$$

$$S_{x,x} + S_{y,y} + q = 0 \tag{3-50}$$

Where q denotes the transverse surface loading.

With the above mentioned stress and strain fields the resultants can be defined with help of the constitutive equations. For the linear elastic case the normal forces become according equation (3-45):

$$\begin{Bmatrix} N_{xx} \\ N_{yy} \\ N_{xy} \end{Bmatrix} = \frac{Eh}{1-\nu^2} \begin{bmatrix} 1 & \nu & 0 \\ \nu & 1 & 0 \\ 0 & 0 & 1-\nu \end{bmatrix} \begin{Bmatrix} \varepsilon_{xx} \\ \varepsilon_{yy} \\ \gamma_{xy} \end{Bmatrix} = \boldsymbol{D}_{\eta} \cdot \boldsymbol{\eta} \tag{3-51}$$

The moments become according equation (3-46):

$$\begin{Bmatrix} M_{xx} \\ M_{yy} \\ M_{xy} \end{Bmatrix} = \frac{Eh^3}{12\left(1-\nu^2\right)} \begin{bmatrix} 1 & \nu & 0 \\ \nu & 1 & 0 \\ 0 & 0 & 1-\nu \end{bmatrix} \begin{Bmatrix} \varepsilon_{xx} \\ \varepsilon_{yy} \\ \gamma_{xy} \end{Bmatrix} = \boldsymbol{D}_{\kappa} \cdot \boldsymbol{\kappa} \tag{3-52}$$

The transverse shear forces become according equation (3-47):

$$\begin{Bmatrix} S_x \\ S_y \end{Bmatrix} = kGh \begin{bmatrix} 1 & 0 \\ 0 & 1 \end{bmatrix} \begin{Bmatrix} \gamma_{xz} \\ \gamma_{yz} \end{Bmatrix} = \boldsymbol{D}_{\gamma} \cdot \boldsymbol{\gamma} \tag{3-53}$$

With E : Young's modulus
ν : Poissons's ratio
G : Shear modulus
k : Shear correction factor

The shear correction factor counts for the effect that the shear stresses are zero at the outer faces of the plate. The shear correction factor is put on $\frac{5}{6}$ [Papadopoulos, 1990]. For plastic problems the same shear correction of $\frac{5}{6}$ is usually applied.

In case of plasticity, the constitutive equations are expressed in the stress rate and the strain rate. So, the resultants are also expressed as rate variables.

In the finite element code DIEKA, three element types are implemented. One of the membrane type, one of the Kirchhoff type and one of the Mindlin type. For each element type a large variety of elements exists. These elements can differ in shape, number of nodes, degrees of freedom, number of integration points and interpolation functions.
The three element types in DIEKA are three node triangular elements. They have displacements and rotations at the corner nodes as degree of freedom. The membrane element is a constant strain triangle. An extended study of plate elements stated that for

the Kirchhoff type the discrete Kirchhoff triangle is most effective; for the Mindlin type the discrete shear triangle is the best choice [Wisselink, 1993]. The integration procedure for the elements depends on the element type. These procedures are explained in appendix A.
Each type has advantages and disadvantages. It is difficult to state which type is most effective based on criteria combining accuracy and computational cost. This strongly depends on the problem that has to be solved.

3.5.1 Membrane Element

The membrane element is a constant strain triangle. The element degrees of freedom are two displacements u and v. The membrane stresses act tangent to the mid-plane. Whereas in equation (3-17) the interpolation is written in general form, for the membrane element are the displacement components interpolated linearly:

$$u\left(L_1, L_2\right) = \sum_{i=1}^{3} L_i u_i \qquad (3\text{-}54)$$
$$v\left(L_1, L_2\right) = \sum_{i=1}^{3} L_i v_i$$

Where L_i are the triangular co-ordinates as explained in appendix A. The vector with the external d.o.f. is written as:

$$\boldsymbol{d} = \left\{u_1 \quad v_1 \quad u_2 \quad v_2 \quad u_3 \quad v_3\right\}^T \qquad (3\text{-}55)$$

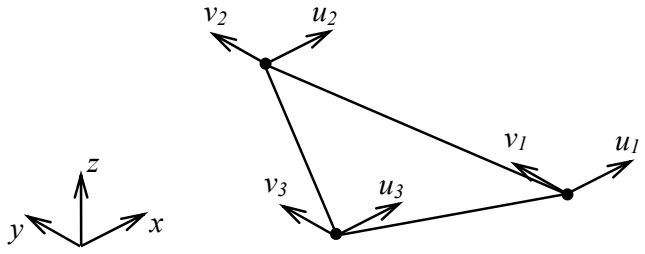

Figure 3-5 *The external degrees of freedom for the membrane element.*

The three membrane strain components are written according equation (3-19) in terms of the d.o.f.:

$$\boldsymbol{\eta} = \boldsymbol{B}_\eta \cdot \boldsymbol{d} \qquad (3\text{-}56)$$

Where the $\boldsymbol{B}_\eta$-matrix is given in appendix B.

When transforming the external d.o.f. to the global co-ordinate system the displacements perpendicular to the element do not contribute to the internal work. This can lead to instabilities of the element. The instability is prevented by adding a small torsion stiffness in the two out-plane directions [Vreede, 1992]. The small torsion stiffness stabilises the calculation but has no noticeable effect on the results. The application of the torsion stiffness can be regarded as a pre-stress condition in the membrane element.

3.5.2 Kirchhoff Element

The formulation of this element is based on the membrane theory and the discrete Kirchhoff theory for bending of thin plates [Batoz, 1980]. The element is labelled DKT, discrete Kirchhoff triangle. The transverse shear energy is neglected and the Kirchhoff hypothesis is introduced in a discrete way; the rotations of the element sides are related to the transverse displacement along the edges of the element. The element has 9 d.o.f. in addition to the membrane d.o.f.. This section is restricted to these additional d.o.f.; in order to avoid diffusion the membrane d.o.f. are left out. The additional d.o.f. are two rotations and one translation in every corner. The vector with external d.o.f. becomes (Figure 3-6a):

$$\boldsymbol{d} = \left\{ w_1 \quad \theta_{x1} \quad \theta_{y1} \quad w_2 \quad \theta_{x2} \quad \theta_{y2} \quad w_3 \quad \theta_{x3} \quad \theta_{y3} \right\}^T \tag{3-57}$$

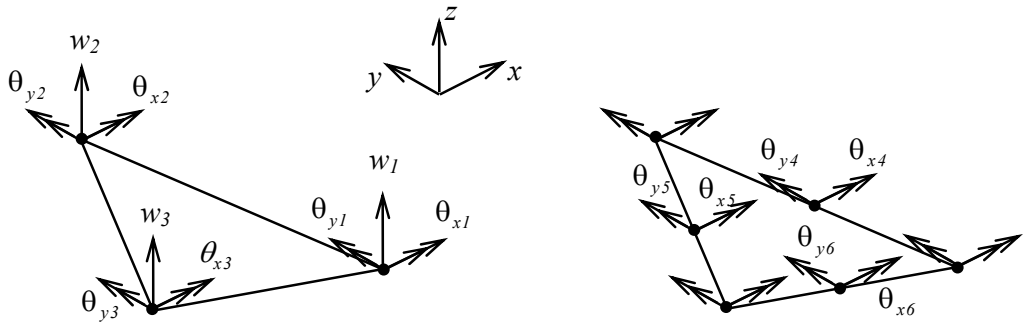

(a) (b)

Figure 3-6 *The external d.o.f (a) and the internal d.o.f. (b) for the Kirchhoff and the Mindlin element.*

The bending strain of the mid-plane, also called curvature, is expressed as:

$$\boldsymbol{\kappa} = \boldsymbol{B}_\kappa \cdot \boldsymbol{\theta}^* \tag{3-58}$$

The $\boldsymbol{B}_\kappa$-matrix is given in appendix B and with the internal d.o.f. θ^*:

$$\boldsymbol{\theta}^* = \left\{ \theta_{x1} \quad \theta_{y1} \quad \theta_{x2} \quad \theta_{y2} \quad \theta_{x3} \quad \theta_{y2} \quad \theta_{x4} \quad \theta_{y4} \quad \theta_{x5} \quad \theta_{y5} \quad \theta_{x5} \quad \theta_{y6} \right\} \tag{3-59}$$

Where the numbers 4, 5 and 6 denote the numbers of the mid-side help nodes (Figure 3-6b).

The Kirchhoff constraints state that the shear component is equal to zero. These constraints are imposed at a number of discrete points; these points are the corner nodes denoted with subscript *i*:

$$\begin{aligned} \gamma_{xzi} &= \theta_{yi} + w_{i,x} = 0 \\ \gamma_{yzi} &= \theta_{xi} - w_{i,y} = 0 \end{aligned} \tag{3-60}$$

And the mid-side help nodes denoted with subscript *k*:

$$\gamma_{szk} = \theta_{nk} - w_{k,s} = 0 \tag{3-61}$$

With the Kirchhoff constraints, equation (3-60) and (3-61), it is possible to express the terms of θ^* in terms of $\boldsymbol{d}$. A general description of the transformation is given below.

It is assumed that the rotation of the element side θ_s varies linear along the sides. The rotation in the middle of the element side can be expressed in terms of the rotation of the corner nodes:

$$\theta_{sk} = \frac{1}{2}\left(\theta_{si} + \theta_{sj}\right) \tag{3-62}$$

Where *k* is the number of the side on which node *k* is situated and *i* and *j* are the corner nodes, *j* stands for the node with the highest number. The rotation θ_{si} is expressed by simple co-ordinate transformation in terms of θ_{xi} and θ_{yi}.

$$\theta_{sk} = \frac{1}{2}\left(\cos\varphi_k\left(\theta_{xi} + \theta_{xj}\right) + \sin\varphi_k\left(\theta_{yi} + \theta_{yj}\right)\right) \tag{3-63}$$

Where φ_k is the orientation of the element side *k*.

The transverse displacement *w* is related to the rotation normal to the mid-plane. A cubic variation of *w* along the sides is imposed [Batoz, 1980]:

$$w_{k,s} = \frac{3}{2l_k}\left(w_j - w_i\right) - \frac{1}{4}\left(w_{j,s} + w_{i,s}\right) \tag{3-64}$$

The term l_k stand for the length of the side where node *k* is situated. The derivative of *w* along the side is:

$$w_{i,s} = \cos\varphi_k \; w_{i,x} + \sin\varphi_k \; w_{i,y} \tag{3-65}$$

With use of equation (3-60) the derivative of *w* is expressed in terms of the rotations and substituted into equation (3-65):

$$w_{i,s} = -\cos\varphi_k\ \theta_{yi} + \sin\varphi_k\ \theta_{xj} \tag{3-66}$$

Substituting equation (3-64) and (3-66) into equation (3-61) gives the Kirchhoff constraints for the DKT element:

$$\theta_{nk} = \frac{3}{2l_k}\left(w_j - w_i\right) - \frac{1}{4}\left(\sin\varphi_k\left(\theta_{xi} + \theta_{xj}\right) - \cos\varphi_k\left(\theta_{yi} + \theta_{yj}\right)\right) \tag{3-67}$$

Equation (3-63) gives an expression of θ_s in terms of θ_x and θ_y of equation (3-67) gives an expression of θ_n in terms of w, θ_x and θ_y. These two equations are sufficient to express the transformation of θ^* to $\boldsymbol{d}$. The transformation is written in short as:

$$\boldsymbol{\theta}^* = \boldsymbol{T}^+ \cdot \boldsymbol{d} \tag{3-68}$$

In appendix C the components of the transformation matrix $\boldsymbol{T}^+$ are elaborated.

Now, the curvature can be expressed in terms of the external d.o.f. $\boldsymbol{d}$:

$$\boldsymbol{\kappa} = \boldsymbol{B}_\kappa \cdot \boldsymbol{T}^+ \cdot \boldsymbol{d}$$

This Kirchhoff element is used in two variants. The first variant has one integration points in-plane and is called DKT1. The second one has three integration points in-plane and is called DKT3. More details on the numerical integration procedure can be found in appendix A.

Because of the low order integration of the DKT1 element instabilities may arise. These instabilities are called Zero Energy Modes (ZEM). The ZEM refer to nodal displacement modes $\boldsymbol{d}$ that are no rigid-body modes but produce zero strain energy:

$$\frac{1}{2}\boldsymbol{d}^T\boldsymbol{K}\boldsymbol{d} = 0 \tag{3-69}$$

The existence of ZEM in an element can lead to incorrect behaviour of a structure. So, the ZEM must be detected and prevented.

An instability in an existing $\boldsymbol{K}$ can be detected by means of an eigen value test. The eigen problem is defined as follows:

$$\left(\boldsymbol{K} - \lambda\,\boldsymbol{I}\right)\boldsymbol{d} = 0 \quad \text{or} \quad \boldsymbol{K}\boldsymbol{d} = \lambda\boldsymbol{d} \tag{3-70}$$

There are as many eigen values λ_i as there are d.o.f. in $\boldsymbol{d}$. To each λ_i corresponds an eigen vector $\boldsymbol{d_i}$. When λ_i is zero, the corresponding $\boldsymbol{d_i}$ should represent a rigid-body mode. The number of eigen values equal zero may not exceed the number of rigid body modes. Too few suggest that the element does not have rigid-body motion without strain. Too many

suggests the existents of ZEM. For an additional eigen value the corresponding ***d*** represents a ZEM.
The stiffness matrix of the DKT1 element has six eigen values equal zero. The number of rigid body modes is three, so the number of ZEM is three. The ZEM are the eigen vectors ***d*** corresponding to the zero eigen values which are no rigid-body modes. Analysing the eigen vectors it was found that the ZEM are a twist of the element sides around the mid-point of the element side (Figure 3-7a). It appeared that the ZEM for the DKT1 element can be expressed in the orientation of the element sides with respect to the x-axis, Figure 3-7b.

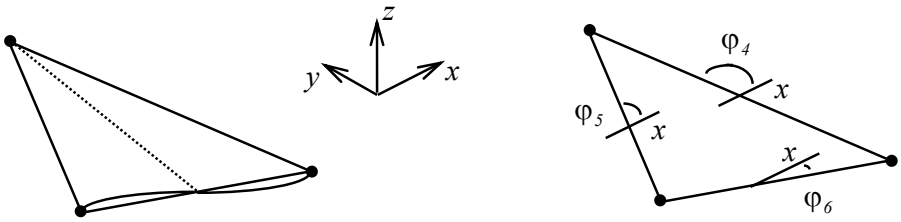

Zero Energy Mode

(a) (b)

Figure 3-7 *A Zero Energy Mode of the DKT1 element (a) and the definition of the orientation of the element sides (b).*

A general expression for the ZEM is given below:

$$\begin{aligned}
\boldsymbol{d}_{ze1} &= \left\{0 \quad -\sin\varphi_4 \quad \cos\varphi_4 \quad 0 \quad -\sin\varphi_4 \quad \cos\varphi_4 \quad 0 \quad \sin\varphi_4 \quad -\cos\varphi_4\right\}^T \\
\boldsymbol{d}_{ze2} &= \left\{0 \quad \sin\varphi_5 \quad \cos\varphi_5 \quad 0 \quad -\sin\varphi_5 \quad \cos\varphi_5 \quad 0 \quad -\sin\varphi_5 \quad \cos\varphi_5\right\}^T \\
\boldsymbol{d}_{ze3} &= \left\{0 \quad \sin\varphi_6 \quad -\cos\varphi_6 \quad 0 \quad -\sin\varphi_6 \quad \cos\varphi_6 \quad 0 \quad \sin\varphi_6 \quad -\cos\varphi_6\right\}^T
\end{aligned} \tag{3-71}$$

Now the ZEM are detected, they must be prevented. The control method must eliminate the instability without simultaneously stiffening the element's modes that are already working well. The method provided here is inexpensive to formulate and works very well [Cook, 1989][Schotmeijer, 1996].
Consider a ZEM $\boldsymbol{d}_{ze}$. In order to suppres this mode, a stabilisation matrix K_s is formed:

$$\boldsymbol{K}_s = \boldsymbol{d}_{ze}\,\boldsymbol{d}_{ze}^{\boldsymbol{T}} \tag{3-72}$$

This stabilisation matrix is weighted with a factor k_s and added to the stiffness matrix. The factor k_s is small, order 10^{-3}, and depends on the shape and area of the element. Note that the ZEM is orthogonal to all other modes:

$$\boldsymbol{d}_{ze}^{T}\,\boldsymbol{d} = 0 \quad \forall\, \boldsymbol{d} \neq \boldsymbol{d}_{ze} \tag{3-73}$$

These orthogonality prevents $\boldsymbol{K}_s$ from stiffening other modes.

3.5.3 Mindlin Element

The formulation of the Mindlin element is valid for analysis of thick to very thin plates. The formulation is based on the membrane theory and on the Mindlin theory [Batoz, 1989]. The element degenerates automatically to the DKT element if the transverse shear stresses do not occur. The expression for the shear stresses are represented in a discrete manner. The element is labelled DST, discrete shear triangle. The element has 9 d.o.f. in addition to the membrane d.o.f.. Again this section is restricted to these additional d.o.f.; in order to avoid diffusion the membrane d.o.f. are left out. The additional d.o.f. are two rotations and one translation in every corner. So, the vector with external d.o.f. is identical to the one of the Kirchhoff element:

$$\boldsymbol{d} = \left\{ w_1 \quad \theta_{x1} \quad \theta_{y1} \quad w_2 \quad \theta_{x2} \quad \theta_{y2} \quad w_3 \quad \theta_{x3} \quad \theta_{y3} \right\}^{T} \tag{3-74}$$

This element can describe bending and shearing. The strain vectors become respectively:

$$\begin{aligned} \boldsymbol{\kappa} &= \boldsymbol{B}_{\kappa} \cdot \boldsymbol{\theta}^{*} \\ \boldsymbol{\gamma} &= \boldsymbol{B}_{\gamma} \cdot \boldsymbol{\theta}^{*} \end{aligned} \tag{3-75}$$

Where the $\boldsymbol{B}_{\kappa}$-matrix and the $\boldsymbol{B}_{\gamma}$-matrix are given in appendix B and again with the internal d.o.f. θ^{*}:

$$\boldsymbol{\theta}^{*} = \left\{ \theta_{x1} \quad \theta_{y1} \quad \theta_{x2} \quad \theta_{y2} \quad \theta_{x3} \quad \theta_{y2} \quad \theta_{x4} \quad \theta_{y4} \quad \theta_{x5} \quad \theta_{y5} \quad \theta_{x5} \quad \theta_{y6} \right\} \tag{3-76}$$

The Mindlin conditions equalise the assumed shear deformation field and the kinematic shear deformation field. The assumed field is derived from the equation of equilibrium and the constitutive law. The kinematic field follows from differentation of the displacement field. The Mindlin condition in the corner nodes is:

$$\begin{aligned} \gamma_{xzi} &= \theta_{yi} + w_{i,x} \\ \gamma_{yzi} &= \theta_{xi} - w_{i,y} \end{aligned} \tag{3-77}$$

And the mid-side nodes:

$$\gamma_{szk} = \theta_{nk} - w_{k,s} \tag{3-78}$$

With the Mindlin conditions, equation (3-77) and (3-78), the terms of θ^{*} can be expressed in terms of $\boldsymbol{d}$. A general description of the transformation is given next.

According equation (3-63) the rotations in the middle of the element side are expressed in terms of the rotations of the corner nodes:

$$\theta_{sk} = \frac{1}{2}\left(\cos\varphi_k\left(\theta_{xi} + \theta_{xj}\right) + \sin\varphi_k\left(\theta_{yi} + \theta_{yj}\right)\right) \tag{3-79}$$

For the derivative of w in the corner nodes to s of element side k counts:

$$w_{i,s} = \sin\varphi_k \; w_{i,x} - \cos\varphi_k \; w_{i,y} \tag{3-80}$$

An expression for the derivative of w to x and y respectively is found in equation (3-77) and is substituted into equation (3-80).

$$w_{i,s} = \sin\varphi_k \left(\gamma_{xzi} - \theta_{yi}\right) - \cos\varphi_k \left(\gamma_{yzi} + \theta_{xi}\right) \tag{3-81}$$

The shear term in the mid-side node γ_{szk} is expressed in terms of γ_{xzk} and γ_{yzk} and substituted into equation (3-78):

$$\theta_{nk} - w_{k,s} = \sin\varphi_k \; \gamma_{yzk} + \cos\varphi_k \; \gamma_{xzk} \tag{3-82}$$

The shear terms in equation (3-82) are the kinematic shear terms. These terms follow from the displacement field and are expressed in equation (3-75).

For the Mindlin element, also a cubic variation of w along the sides is imposed:

$$w_{k,s} = \frac{3}{2l_k}\left(w_j - w_i\right) - \frac{1}{4}\left(w_{j,s} + w_{i,s}\right) \tag{3-83}$$

Substituting equation (3-81), (3-83) and (3-75) into equation (3-82) gives the expression for θ_n:

$$\theta_{nk} = \frac{3}{2l_k}\left(w_j - w_i\right) - \frac{1}{4}\left(\sin\varphi_k\left(\theta_{xi} + \theta_{xj}\right) - \cos\varphi_k\left(\theta_{yi} + \theta_{yj}\right)\right) - \tag{3-84}$$

$$\frac{3}{2}\left[\cos\varphi_k \quad \sin\varphi_k\right] B_\gamma \cdot \boldsymbol{\theta}^*$$

Comparing this equation with the equation for the Kirchhoff element, equation (3-67), only the fourth term is new. This term contains the components θ_{n4}, θ_{n5} and θ_{n6}. That means that a matrix must be inverted to find the transformation matrix. This means that the element is not fully compatible anymore.

The rotations θ_{sk} are expressed in terms of θ_{xk} and θ_{yk}, equation (3-79); the rotations θ_{nk} are expressed in terms of w, θ_{xk} and θ_{yk}, equation (3-84). These two equations are used to complete the transformation. In short the transformation is written as:

$$\boldsymbol{\theta}^{*} = \boldsymbol{T}^{++} \cdot \boldsymbol{d} \tag{3-85}$$

In Appendix D the components of the transformation matrix $\boldsymbol{T}^{++}$ are given.

The curvature and the shearing expressed in terms of $\boldsymbol{d}$ are:

$$\begin{aligned} \boldsymbol{\kappa} &= \boldsymbol{B}_{\kappa} \cdot \boldsymbol{T}^{++} \cdot \boldsymbol{d} \\ \boldsymbol{\gamma} &= \boldsymbol{B}_{\gamma} \cdot \boldsymbol{T}^{++} \cdot \boldsymbol{d} \end{aligned} \tag{3-86}$$

3.6 Elastic Tests

In this section a few elastic tests are performed. The results of these tests give information on the performance of the element. The first series of tests are the so called patch tests. A patch test is a simple test and serves as a necessary and sufficient condition for correct convergence of a finite element formulation. A patch test does not give information on the convergence characteristic of the element. Therefore tests which cannot be solved exactly are required. These tests are denoted as convergence tests or precision tests. The proposed tests are an *obstacle course* for plate elements [Belytschko, 1985].

3.6.1 Patch Tests

The convergence of an element is guaranteed when the following two conditions are fulfilled:

- An element can describe a theoretical constant stress state.
- The constant theoretical solution is independent of mesh irregularities.

The plate elements of section 3.5. can describe membrane, bending and shear states. For each state a patch test is defined. The membrane element can only be applied for the membrane force patch test.

Membrane force (Figure 3-8a)
For the membrane force, all the elements pass the patch test.

Bending moment (Figure 3-8b)
The membrane element cannot describe this bending state. The other elements pass the patch test.

Twisting moment (Figure 3-8c)
The Kirchhoff elements DKT1 and DKT3, pass this test. The Mindlin element DST, passes this test only for thin plates $L/h < 10$, where L denotes the length of the structure. For thick plates $L/h > 10$. the element fails the test as a result of the application of the Mindlin conditions. The element is not fully compatible for thick plates. But in case of mesh refinements the element converges to the exact solution. So, for thick plates this test

is not a patch test but a convergence test. The element is said to have passed a weak patch test.

Shear force (Figure 3-8d)
This test can only be applied on the Mindlin element for thick plates, otherwise this is a convergence test. In a plate under constant shear force, S_{xx}, the bending moments M_{xx} and M_{xy} are linear. If the bending stiffness is very large compared to the shear stiffness, the curvature tends to zero and the strain energy is represented by the shear strain energy only. This is the thick plate limit. For thick plates the element passes this test.

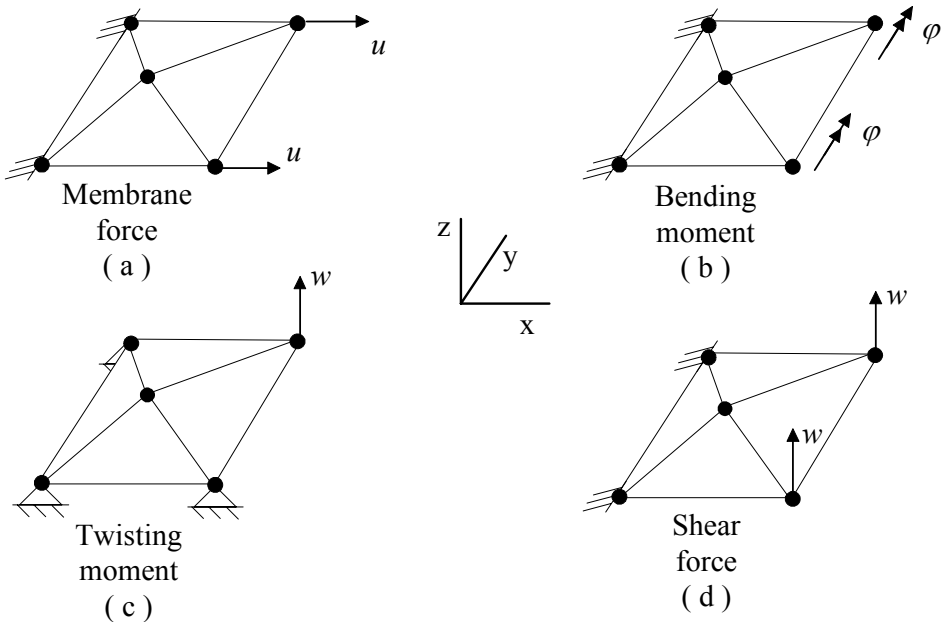

Figure 3-8 *Patch tests for the different stress states.*

The conclusion from these patch tests is that under the right conditions, all elements fulfil the tests. The user of these elements must be aware of this conclusion.

3.6.2 Convergence Tests

The three convergence tests described in this section form an obstacle course for plate elements. The tests are developed to challenge the capabilities required in a well performing element. A good element has the ability to handle inextensional bending modes, rigid-body motion without straining and complex membrane stress states.
Beside, the course must be reasonable short. It is superfluous to include tests which only disqualify elements which are already disqualified by other tests. The three problems

described here are an extremely discriminating set of problems [Belytschko, 1985]. The problems are elastic, so it is sufficient to use two integration points in thickness direction.

Hemispherical Shell

The Hemispherical Shell problem is a challenging test of an element's ability to represent inextensional bending modes. It exhibits almost no membrane strains. It is a very useful problem for checking the ability of the element to handle rigid body rotations about the normal to the surface.

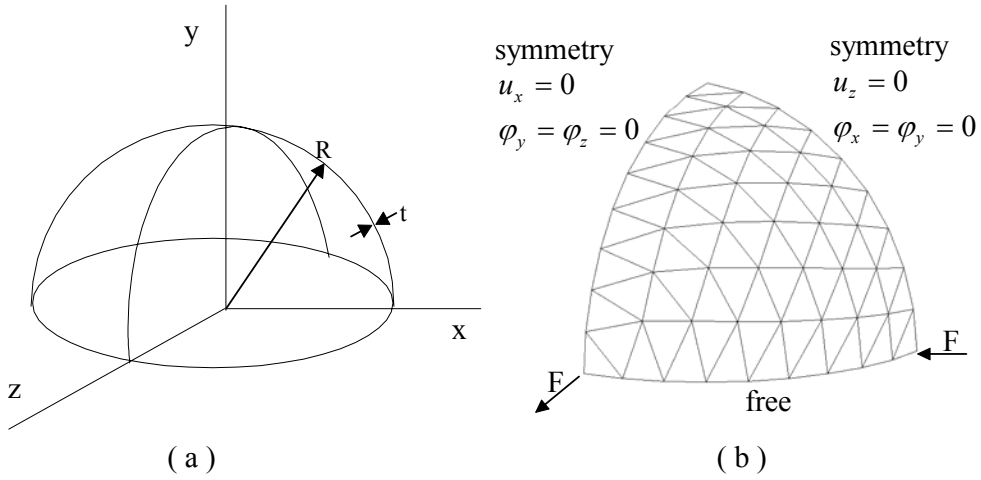

Figure 3-9 *Geometry of the Hemispherical Shell (a) and a mesh with its boundary conditions.*

The geometry of this problem is shown in Figure 3-9a. Half a sphere of very thin material is radial loaded with a force alternating at 90º. Because of the symmetry in the geometry only one quarter of the problem is modelled. An example of a mesh with its boundary and symmetry conditions is shown in Figure 3-9b. The problem parameters are listed in Table 3-1.

Radius R	10.0 mm
Thickness t	0.04 mm
Young's modulus E	$6.825 \cdot 10^7$ N/mm^2
Poisson's ratio ν	0.3
Boundary conditions	Bottom edge of hemisphere is free
Loading	Opposing radial point loads alternating at 90º, F= ±2.0 N
Solution	Radial displacement at loaded points 0.0924 mm

Table 3-1 *Problem parameters for the Hemispherical Shell.*

The results of this problem are shown in Figure 3-10. On the x-axis the nodes per side are printed and on the y-axis the solution of the simulation. The exact solution of the problem is given in Table 3-1 and is also depicted in Figure 3-10. The more nodes per side the closer the solution is to the exact solution. The DKT3 and the DST perform identical. This was expected because of the very thin sheet. The DKT1 converges slower than the other two elements.

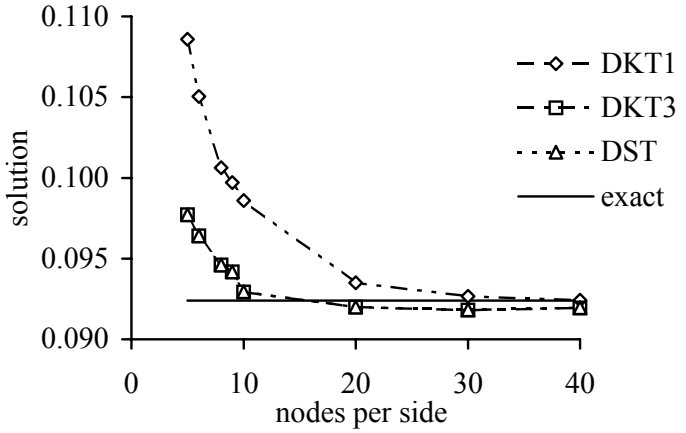

Figure 3-10 *Results of the Hemispherical Shell problem.*

Scordelis-Lo Roof

The Scordelis-Lo Roof problem is extremely useful to determine the ability of an element to accurately solve complex states of membrane strain. A substantial part of the strain energy is the membrane strain energy.

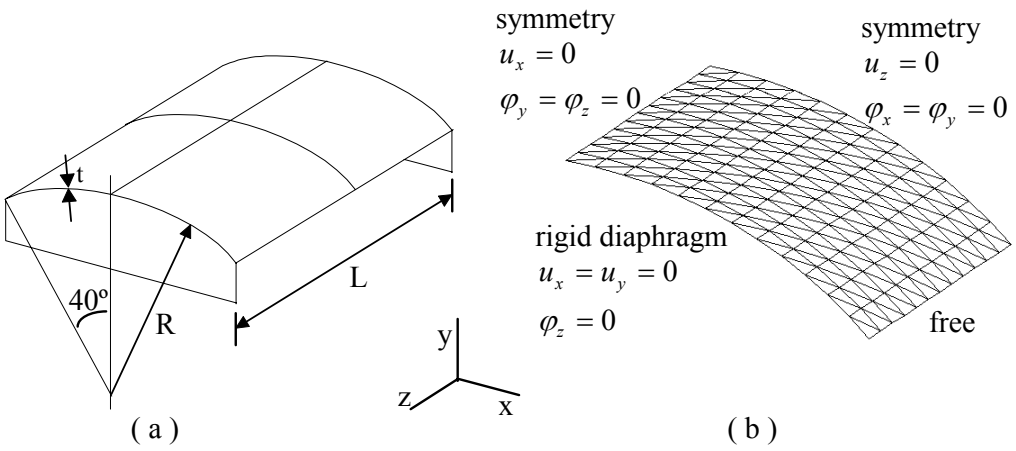

Figure 3-11 *Geometry of the Scordelis-Lo Roof (a) and a mesh with its boundary conditions (b).*

In Figure 3-11a the geometry of this test problem is shown. A curved roof supported at both ends is loaded with the gravity load. Because of symmetry only one quarter of the problem is simulated. Figure 3-11b shows an example of a mesh used for this problem. The boundary conditions and the symmetry conditions are also depicted. The complete problem parameters are printed in Table 3-2.

Length L	50.0 mm
Radius R	25.0 mm
Thickness t	0.25 mm
Young's modulus E	$4.32 \cdot 10^8$ N/mm^2
Poisson's ratio ν	0.0
Boundary conditions	Supported at each end by rigid diaphragm
Loading	Uniform vertical gravity load of 90.0 N per unit area
Solution	Converged numerical solution, vertical displacement at the mid-side of the free edge: 0.3024 mm

Table 3-2 *Problem parameters for the Scordelis-Lo Roof.*

The results of this problem are shown in Figure 3-12. The nodes per side are plotted against the solution. All three elements converge the same way and for 23 nodes per side they are almost identical to the exact solution. The DKT1 element behaves a little different for a small number of nodes per side but for seven and more nodes per side the behaviour is comparable with the DKT3 and DST.

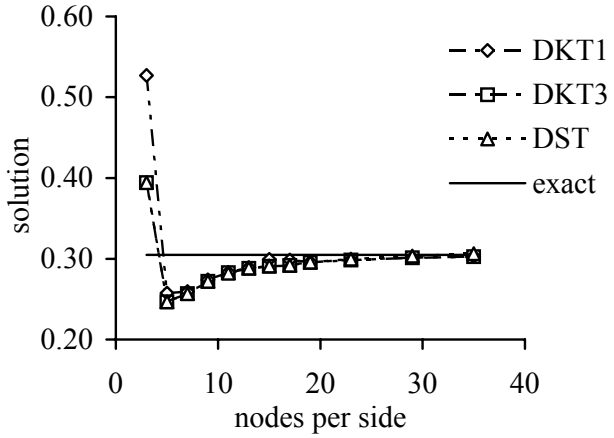

Figure 3-12 *Solution of the Scordelis-Lo Roof problem.*

Pinched Cylinder

The Pinched Cylinder with a diaphragm is one of the most severe tests for both inextensional bending modes and complex membrane stress states.

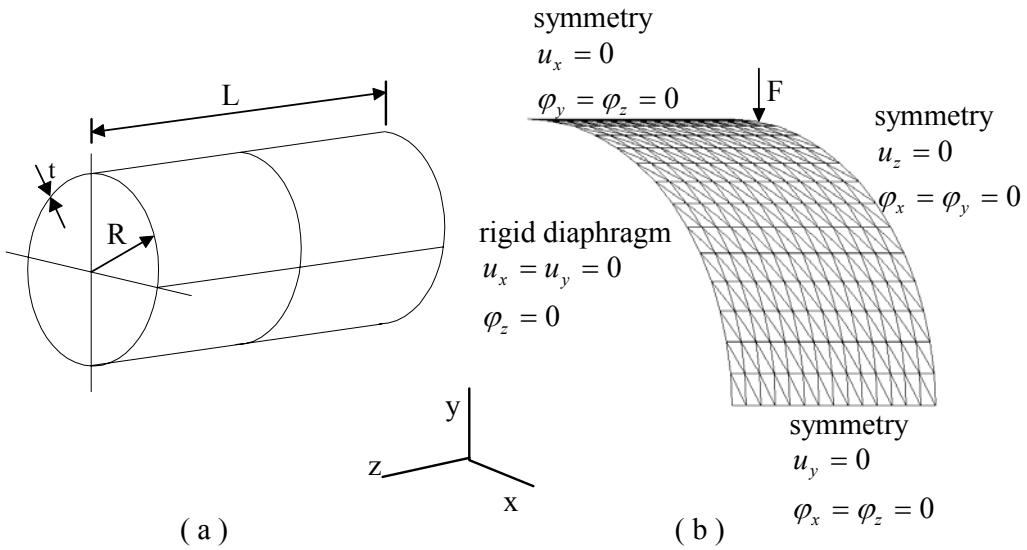

Figure 3-13 *Geometry of the Pinched Cylinder (a) and a mesh with its boundary conditions (b).*

Figure 3-13a shows the geometry of this problem. A cylinder with a diaphragm is loaded in the middle with opposing radial loads. Because of symmetry only one eight of the problem is simulated. A used mesh with the boundary and symmetry conditions is shown in Figure 3-13b. Table 3-3 lists the complete problem parameters.

Length *L*	600.0 mm
Radius *R*	300.0 mm
Thickness *t*	3.0 mm
Young's modulus *E*	$3.0 \cdot 10^6$ N/mm^2
Poisson's ratio ν	0.3
Boundary conditions	Supported at each end by rigid diaphragm
Loading	Opposing radial loads in the middle of the cylinder F=1.0 N
Solution	Radial displacement at point load: 0.1824 10^{-4} mm

Table 3-3 *Problem parameters for the Pinched Cylinder.*

In Figure 3-14 are the solutions of the simulations shown against the number of nodes per side. Again the DKT3 and DST perform very well and almost identical. The DKT1 converges much slower, but it does.

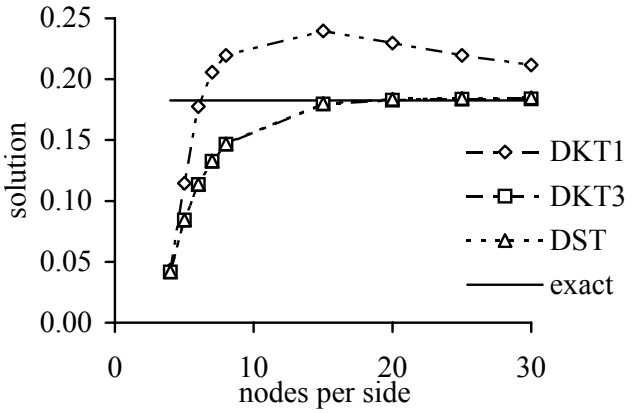

Figure 3-14 *Solution of the Pinched Cylinder problem.*

The conclusion from the convergence test is that all three elements fulfil the tests. The DKT3 and DST converge faster than the DKT1, but the DKT1 element is less time and memory consuming than the other two elements.

3.7 Plastic Tests

In case of plastic calculations the material behaviour is history dependent and not linear anymore. In order to test the plastic performance of the elements a few simple tests are performed. The tests treat different types of deformation the elements can describe.
The first test treats the membrane deformations. The second test treats the bending deformations. Because of the variation of the stresses in thickness direction the number of integration points in height is important. The last test treats combined bending and membrane deformations.

Membrane Deformations

The membrane test is a simple test. A clamped sheet is elongated with a prescribed displacement. An elastic plastic material model with linear hardening is used. The initial yield stress was 250 N/mm^2 and the Young's modulus was $1.0 \cdot 10^5$ N/mm^2. The resulting stress-strain curve of this test is shown in Figure 3-15. The non-linear material behaviour can be distinguished at the transition from elastic to plastic. This transition is at a stress level of 250 N/mm^2. All three element types can describe this deformation.

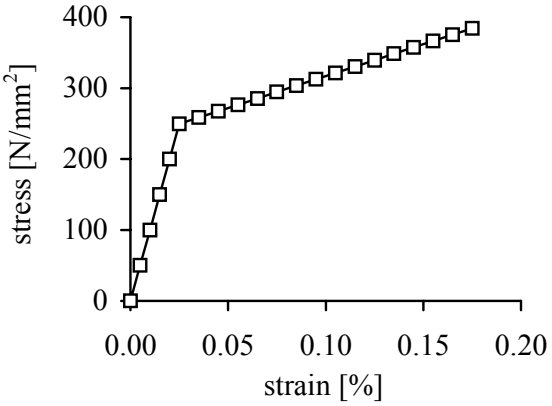

Figure 3-15 *Results of the membrane deformation test.*

Bending Deformations

This test evaluates pure bending of a sheet and can only be evaluated with the Kirchhoff and Mindlin elements. The material model used is elastic plastic material with linear hardening. The difficulty of this problem is the changing stiffness at the transition from elastic behaviour to plastic behaviour. Because of the pure bending deformation this transition starts at the outer side of the sheet and moves inside with further bending. The numerical integration procedure must handle the moving transition.

The integration of the stiffness tensor is performed using a variable number of integration points in the thickness direction. The accuracy of the integration in the thickness direction increases with increasing number of integration points. The results of the simulations are shown in Figure 3-16. The bending moment is shown as function of the curvature of the sheet. Figure 3-16(a) shows the whole range of the curvature and Figure 3-16(b) shows a close-up of the elastic plastic transition. The simulations are performed with 2 up to 7 integration points in thickness direction.

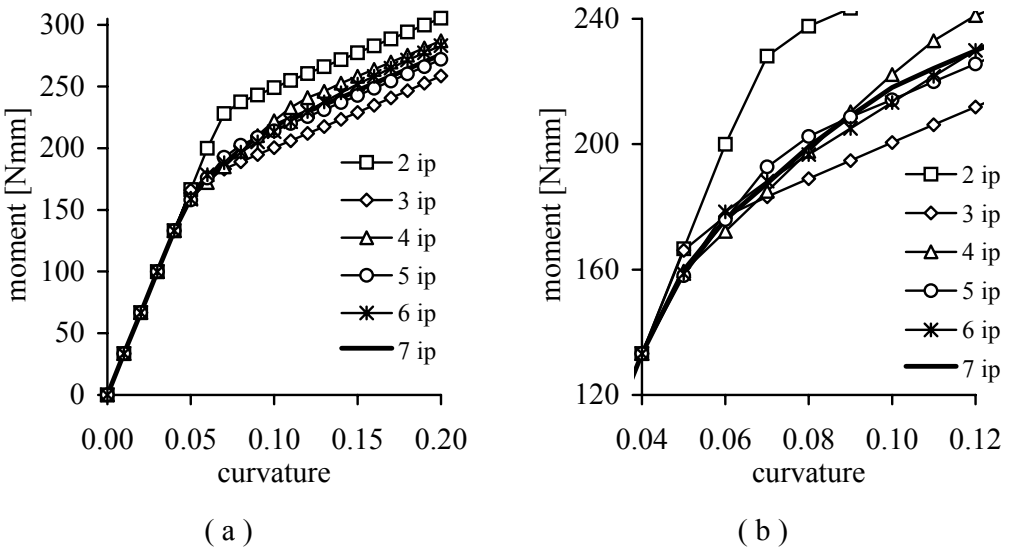

Figure 3-16 *Results of the numerical stiffness integration for the bending test.*

The result for seven integration points coincides as far as can be distinguished in the figure with the exact solution. When looking at the results, the following remarks can be made:

- The elastic part is solved exactly. So, the elastic stiffness tensor is integrated exactly for all number of integration points.
- The calculated elastic deformation is larger than the exact elastic deformation because the integration points are never located at the surface. The transition from elastic to plastic deformation takes place in an integration point at the moment when the surface is already plastic.
- The moment-curvature lines wiggles several times as a consequence of the location of the integration points, see Figure 3-16(b). When the stress in an integration point reaches the yield stress the curve twists. For example, the solution for 4 integration points twists two times; symmetry with respect to the neutral surface causes two integration points to become plastic at the same time.
- It appears that an even number of integration points overestimates the stiffness whereas an odd number underestimates the stiffness. The integration points in the *even case* are on the average more situated near the mid plane than in the *odd case*. The plastic deformation grows from the surface to the mid plane and reaches the integration points at a later stage.

Combined Bending and Membrane Deformations

In this test an initially flat sheet is loaded with a deformation cycle as shown in Figure 3-17 and explained below:

- In the first stage the sheet is elongated with a force F in sheet direction, step one (Figure 3-17a). The force is chosen that large so that the pure membrane stress coincides with the initial yield stress This force remains on the sheet during the bending process.
- In step two where the sheet is bent down (Figure 3-17b).
- In the third stage the sheet is bent up in two steps, step three and four (Figure 3-17c).

- In the last stage the sheet is bend back in its initial stage, step five, and the load F is removed, step six (Figure 3-17d).

The test can be performed with the Kirchhoff and the Mindlin element, both elements showed the same results. The material model used is elastic plastic material with linear hardening.

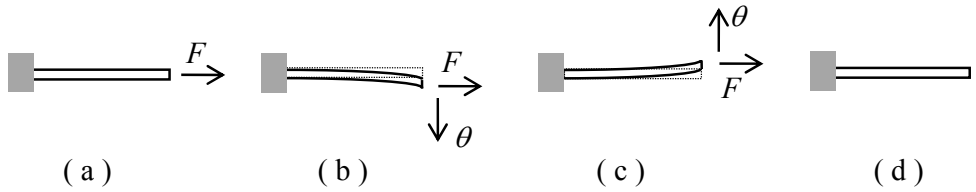

Figure 3-17 *Test cycle for the combined bending and membrane deformations.*

Figure 3-18 shows the results of this test. The stress in x-direction is plotted as a function of the strain of the mid-plane in x-direction. Figure 3-18(a) shows the whole range of the deformation cycle and Figure 3-18(b) shows a close-up of the stresses in the bending range. The stresses of the lower face, the mid plane and the upper face of the sheet are printed. The markers in the graph coincide with the steps of the deformation cycle.
In the first step the stress is uniform in the sheet. In step two, during the first bend the stress at the upper face is stretched and exceeds the yield stress. Because of the non linear material behaviour the neutral plane slightly moves down and the mid plane is also deformed plastic. When the sheet is bend back in the third step, the stresses do not return into a uniform stress distribution because of the appeared strain hardening. In step four the sheet is bend up and the stress at the lower face exceeds the yield stress. Again the mid plane deforms plastic because of the movement of the neutral plane. When in step five the sheet is bend back in its initial state, the stresses at the sheet faces are lower than at the mid plane. When releasing the sheet, it relaxes further. The gradient of the three curves differ because the stress is plotted as function of the strain of the mid plane. The stress distribution is not uniform in the sheet because the hardening was not homogenous in the sheet. Residual stresses remain in the sheet.

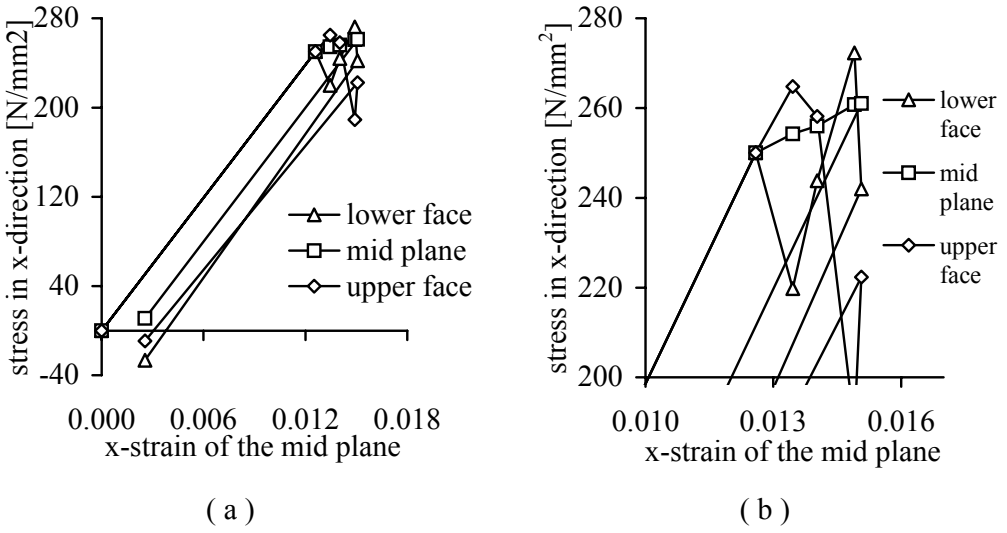

Figure 3-18 *Results of the combined bending and membrane deformation test.*

3.8 Concluding Remarks

This chapter started with a general explanation of the finite element method. This method is used to simulate the deep drawing process. In order to simulate this process plate elements are used. Three different element types are treated, the membrane element, the Kirchhoff element and the Mindlin element. All three elements differ in performance and in computational cost. Depending on the problem to be solved the user has to decide the right element type.

3.9 References

[Batoz, 1980]
Batoz J.L., K.J Bathe, L.W. Ho, *A study of three-node triangular plate bending elements,* Int. J. Num. Meth. Eng., 15, 1771-1812, 1980

[Batoz, 1989]
Batoz J.L., P. Lardeur , *A discrete shear triangular nine d.o.f element for the analysis of thick to very thin plates,* Int. J. Num. Meth. Eng., 28, 533-560, 1989

[Belytschko, 1985]
Belytschko T.,H. Stolarski, W.K. Liu, N. Charpenter, J.S.J. Ong, *Stress projection for membrane and shear locking in shell finite elemnts*, Comp. Meth. Appl. Mech. Eng., 51, 221-258, 1985

[Cook, 1989]
Cook R.D., *Concepts and applications of finite element analysis,* third edition, John Wiley & Sons, New York, 1989

[Huétink, 1986]
Huétink J., *On the numerical simulations of thermo mechanical forming processes,* PhD-thesis, University of Twente, 1986

[Kamperman, 1994]
Kamperman S., *A Mindlin element and material model for sheet metal forming simulations,* Graduate report Computational Mechanics, University of Twente, 1986

[Papadopoulos, 1990]
Papadopoulos P.,R.L. Taylor, *A Triangular element based on Reissner-Mindlin plate theory*, Int. J. Num. Meth, Eng., 30, 1029-1049, 1990

[Schotmeijer, 1996]
Schotmeijer G.J., *A Kirchhoff element with zero energy stabilisation,* Graduate report, University of Twente, 1996

[Vreede, 1992]
Vreede P.T., *A finite element method for simulations of 3-dimensional sheet metal forming,* PhD-thesis, University of Twente, 1992

[Wisselink, 1993]
Wisselink H.H., *Triangular elements for bending of thin and thick plates,* Graduate report (in Dutch), University of Twente, 1993

[Zienkiewicz, 1977]
Zienkiewicz O.C., *The Finite Element Method,* McGraw-Hill Book Company, 1977

4. Contact

The phenomenon of contact occurring during the sheet metal forming process is an important factor. It is the driving force of deforming the material. In finite element simulations it is also a major field of interest. Several aspects must be dealt with, for example the determination of the contact points, the normal forces and the friction forces. These aspects are discussed in this chapter.
Section 4.1 discusses the modelling of the contact behaviour. With this model the normal force and the friction force can be determined. The tool description is discussed in section 4.2. In section 4.3 the contact search is discussed. With this search, the point of contact on the discretised tools is determined.

4.1 Modelling the Contact Behaviour

The contact behaviour is modelled with constitutive equations. These equations must describe the behaviour of no penetration of two body surfaces and whether these two body surfaces stick or slip. The contact behaviour presented here is based on a friction layer approach [Lugt, 1986]. Firstly, the normal force which prevents the penetration is considered. Secondly, the friction force is looked at.

4.1.1 Normal Contact

The contact condition is formulated via a gap function g. The function is defined in terms of the closest point projection (Figure 4-1). The size of the gap function is the perpendicular distance from the node n to the contact surface, denoted with $\|g\|$. The sign of g states whether there is contact or not. When $g>0$ no contact occurs, when $g\leq 0$ contact occurs and n penetrates the body.

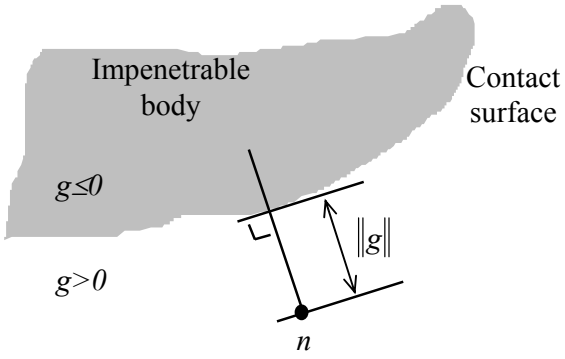

Figure 4-1 *Definition of the gap function g.*

When the node *n* starts to penetrate the body, a pressure prevents *n* of further penetration. The pressure represents the normal contact stress and is denoted by τ_n. The value of this pressure is defined by a penalty parameter, also called the contact stiffness, E_c:

$$\tau_n = E_c \cdot g \tag{4-1}$$

This approach of describing normal contact is known as the penalty approach. The advantages of this technique are that it is simple, it introduces no additional equations and it is interpreted from a physical standpoint. It is also known that this approach worsens when the contact stiffness increases, while the impenetrable condition is satisfied only in limit of infinite stiffness values [Simo, 1992].
Another problem that arises is that with small variations of the gap function the contact stress may vary considerably, resulting in a disturbance of the stress equilibrium. A method to avoid unwanted variations is to apply damping. The damping is a function of the change in gap function; this change is denoted by Δg. Even when for $g>0$, a small amount of damping is applied. The damping starts to work at a value of g_{damp}. The damping value is denoted by C_d. When $g>0$ the damping decreases with the reciprocal of its opening. The damping stabilises the mechanism from contact to no contact and vice versa. The expression for the contact normal pressure becomes:

$$\begin{aligned} \tau_n &= 0 && \text{for } g_{damp} < g \\ &= \left(1 - \frac{g}{g_{damp}}\right) C_d \cdot \Delta g && \text{for } 0 < g \le g_{damp} \\ &= E_c \cdot g + C_d \cdot \Delta g && \text{for } g \le 0 \end{aligned} \tag{4-2}$$

The normal pressure against the gap function is presented in a graph in Figure 4-2. In this figure a contact cycle of a node penetrating into a body with constant step size Δu is described.

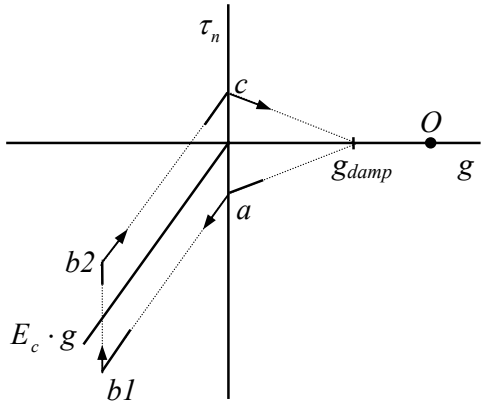

Figure 4-2 *The normal contact stress against the gap function.*

The contact cycle will be described point by point

- The cycle starts at point *O* and the node moves to the left. While the gap function *g* is larger than g_{damp} no contact pressure is present.
- When *g* decreases, the damping starts to act when $g=g_{damp}$. The damping results already in a small contact pressure. The damping prevents the node from penetrating the body too fast, the contact is already felt. The damping increases with decreasing *g*; the contact pressure increases too.
- At the moment that $g=0$, point *a,* the contact spring is activated and the damping has reached its maximum constant value. The contact pressure now increases with the contact stiffness and with the damping.
- When the direction of movement changes, the damper works in the opposite direction and the contact pressure jumps from point *b1* to point *b2*. The damper prevents the movement of losing contact to fast. This can be seen when *g* approaches 0, the contact pressure has become a tensile traction which holds the contact.
- At the moment $g=0$, point *c*, the contact spring stops working. The contact pressure which is now a tensile traction depends on the damping only. With increasing *g* the damping decreases.
- Finally the contact pressure is zero at $g=g_{damp}$.

The damping has a positive influence on the open-closure behaviour. But, the damping can not be chosen too large because otherwise unwanted tensile stresses occur. This becomes worse with an increasing step size because Δg becomes larger too [Stoker, 1994].

4.1.2 Frictional Contact

The friction is not totally irreversible, it has a reversible part as well. The reversible part is caused by elastic deformations of the local contact spots. When two surfaces with many asperities are considered a small tangential displacement will result in a small tangential stress, proportional to the displacement. This linear elastic contact behaviour results in:

$$\dot{\boldsymbol{\tau}} = \boldsymbol{E}^{C} \cdot \boldsymbol{d}^{rv} \tag{4-3}$$

Where $\boldsymbol{E}^{C}$ is the contact stiffness tensor and $\boldsymbol{d}^{rv}$ is the reversible relative velocity.

This relative velocity is related to the local co-ordinates, see Figure 4-3a. The vectors $\boldsymbol{e}_1$ and $\boldsymbol{e}_2$ denote the tangential directions whereas the vector $\boldsymbol{e}_3$ denotes the normal direction. The reversible contact behaviour is illustrated in Figure 4-3b. The elastic stiffness in normal direction as described in the previous sub-section is denoted by E_{33} and the elastic stiffness in the tangential direction are denoted by E_{11} and E_{22}. The contact stiffness tensor $\boldsymbol{E}^{C}$ has a diagonal form and when written in a matrix the components are:

$$\left[E_{ij}\right] = \begin{bmatrix} E_{11} & 0 & 0 \\ 0 & E_{22} & 0 \\ 0 & 0 & E_{33} \end{bmatrix} \tag{4-4}$$

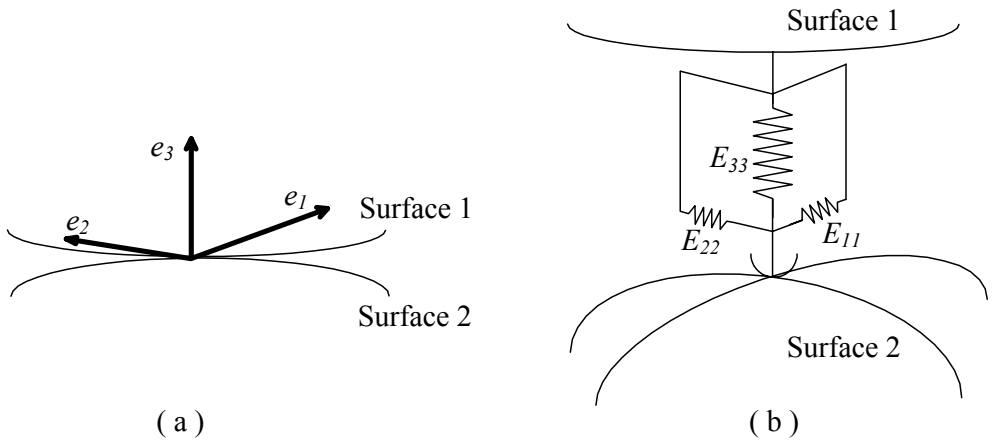

Figure 4-3 *The local co-ordinate system (a) and the contact behaviour (b).*

In the situation when there is no contact, the stiffness between the two bodies vanishes, the damping as mentioned in section 4.1.1 stays. In that case the stiffness tensor is set to zero. In the present study a non-isotropic linear contact situation is considered. After the tangential stress has reached a critical value, sliding of the bodies relative to each other takes place. It is assumed that the relative velocity can be decomposed in a reversible part and an irreversible part:

$$\boldsymbol{d} = \boldsymbol{d}^{rv} + \boldsymbol{d}^{ir} \tag{4-5}$$

Substituting (4-5) into (4-3) results in:

$$\dot{\boldsymbol{\tau}} = \boldsymbol{E}^{C} \cdot \left(\boldsymbol{d} - \boldsymbol{d}^{ir} \right) \tag{4-6}$$

In case of contact with a possibility of frictional sliding, stick or slip will be determined by the contact function:

$$\phi^{C} = \tau_1^2 + \tau_2^2 - \mu^2 \tau_3^2 \tag{4-7}$$

Where τ_1 and τ_2 are the shear stress components and τ_3 is the normal contact stress from sub-section 4.1.1, which are all related to the local co-ordinate system. The friction coefficient is denoted by μ.
The contact function determines the region in the contact stress space in which only reversible behaviour or stick occurs, $\phi^C<0$. Slip occurs when $\phi^C=0$, this surface is called the slip cone and is shown in Figure 4-4. The top angle of the cone depends on the coefficient of friction.

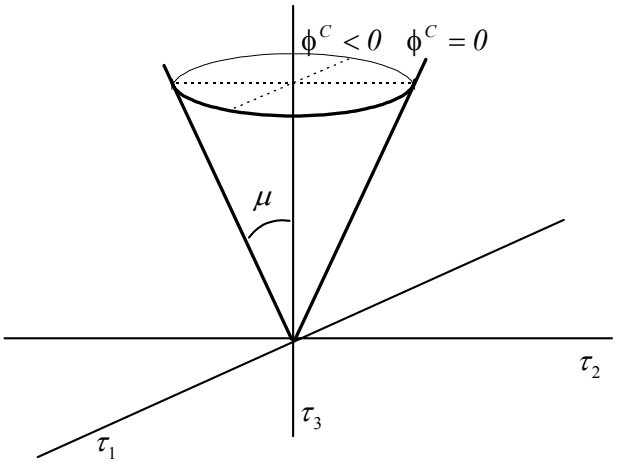

Figure 4-4 *The slip cone in the stress space.*

For sliding to occur the contact stress vector must satisfy the condition $\phi^C=0$ and must remain on the slip surface, which results in case of a constant coefficient of friction in:

$$\dot{\phi}^C = 0 \quad \Rightarrow \quad \frac{\partial \phi^C}{\partial \boldsymbol{\tau}} \cdot \dot{\boldsymbol{\tau}} = 0 \tag{4-8}$$

The irreversible relative velocity can be associated with the gradient of a potential function ϕ in the stress space. Normally this potential function depends on the same variables as the slip surface. However, the normal component of the irreversible relative velocity is assumed to be zero. So, the potential function is only a function of the shear stresses:

$$\varphi = \tau_1^2 + \tau_2^2 \tag{4-9}$$

The irreversible relative velocity must satisfy the following equation:

$$\boldsymbol{d}^{ir} = \kappa \frac{\partial \varphi}{\partial \boldsymbol{\tau}} \tag{4-10}$$

With $\kappa \geq 0$ if $\left(\phi = 0 \wedge \dot{\phi} \geq 0\right)$

$\kappa = 0$ if $\left(\phi < 0\right) \vee \left(\phi = 0 \wedge \dot{\phi} < 0\right)$

The scalar κ can be determined by substitution of equation (4-6) and (4-10) into equation (4-8):

$$\frac{\partial \phi^C}{\partial \boldsymbol{\tau}} \cdot \boldsymbol{E}^{\boldsymbol{C}} \cdot \left(\boldsymbol{d} - \kappa \frac{\partial \varphi}{\partial \boldsymbol{\tau}} \right) = 0 \tag{4-11}$$

Leading to:

$$\kappa = \left(\frac{\partial \phi^C}{\partial \boldsymbol{\tau}} \cdot \boldsymbol{E^C} \cdot \frac{\partial \varphi}{\partial \boldsymbol{\tau}} \right)^{-1} \left(\frac{\partial \phi^C}{\partial \boldsymbol{\tau}} \cdot \boldsymbol{E^C} \cdot \boldsymbol{d} \right) = 0 \tag{4-12}$$

Substitution of equation (4-10), with κ according to (4-12) into equation (4-6) gives:

$$\dot{\boldsymbol{\tau}} = \left(\boldsymbol{E^C} - \boldsymbol{Y^C} \right) \cdot \boldsymbol{d} \tag{4-13}$$

With:

$$\boldsymbol{Y^C} = \frac{\boldsymbol{E^C} \cdot \frac{\partial \varphi}{\partial \boldsymbol{\tau}} \frac{\partial \phi^C}{\partial \boldsymbol{\tau}} \cdot \boldsymbol{E^C}}{\frac{\partial \phi^C}{\partial \boldsymbol{\tau}} \cdot \boldsymbol{E^C} \cdot \frac{\partial \varphi}{\partial \boldsymbol{\tau}}} \tag{4-14}$$

The contact slip tensor $\boldsymbol{Y}^C$ is not symmetric since:

$$\frac{\partial \varphi}{\partial \boldsymbol{\tau}} \neq \frac{\partial \phi^C}{\partial \boldsymbol{\tau}} \tag{4-15}$$

Applying equation (4-7) and (4-9) and performing some algebraic manipulations the components of $\boldsymbol{Y}^C$ become:

$$\left[Y_{ij}^C \right] = \frac{1}{E_{11}\tau_1^2 + E_{22}\tau_2^2} \begin{bmatrix} E_{11}^2 \tau_1^2 & E_{11}E_{22}\tau_1\tau_2 & -\mu^2 E_{11}E_{33}\tau_1\tau_3 \\ E_{11}E_{22}\tau_1\tau_2 & E_{22}^2\tau_2^2 & -\mu^2 E_{22}E_{33}\tau_2\tau_3 \\ 0 & 0 & 0 \end{bmatrix} \tag{4-16}$$

In the case of stick the tensor $\boldsymbol{Y}^C$ is set to $\boldsymbol{0}$.

When there is no contact, or when two bodies loose contact, $\boldsymbol{E}^C$ and $\boldsymbol{Y}^C$ are set to $\boldsymbol{0}$.

The tangential stiffness is smaller than the normal stiffness, it is set on $\mu \cdot E_{33}$. This results in a constant sliding distance independent of the coefficient of friction and a better convergence behaviour for low friction or friction less simulations. The constitutive behaviour for contact is implemented in the finite element code DIEKA [Vreede, 1992].

4.1.3 Coefficient of Friction

As a first approximation the coefficient of friction μ is a constant global parameter. This friction model is called the Coulomb friction model. From a tribological point of view the use of a global constant coefficient of friction is not corresponding to practice. According to [Schipper, 1988] the coefficient of friction depends on the local contact conditions. This means that the contact conditions and thus the coefficient of friction might differ for each sheet/tool contact. According to [Schey, 1983] there are several different contacts between the sheet and the tools for each forming process. Therefore, a good friction model needs a coefficient of friction which depends on the local contact conditions.

In the work of [Schipper, 1988] the coefficient of friction is presented as a function of the dimensionless lubrication number L, which in its turn is a function of several operational parameters:

$$L = \frac{\eta \cdot v}{p \cdot R_a} \tag{4-17}$$

With η : the dynamic viscosity [Pa·s]
v : the sum velocity [m/s]
p : mean contact pressure [Pa]
R_a : CLA surface roughness [m]

When the coefficient of friction μ is plotted as a function of L the following graph is found, see Figure 4-5 [Haar, 1996].

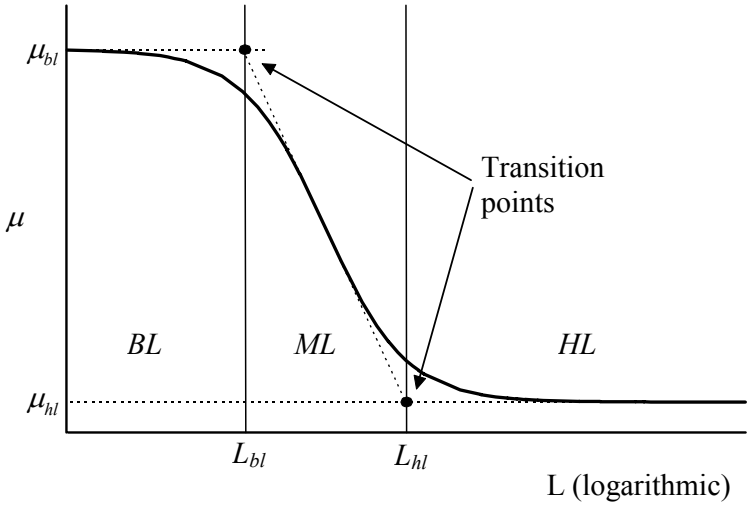

Figure 4-5 *Generalised Stribeck curve* [Haar, 1996].

In this figure, which is called the generalised Stribeck curve, three different zones can be distinguished. On the left hand side of the graph μ has a constant high value, this is the boundary lubrication regime, *BL*. Under these conditions the load on a contact is completely carried by the interacting surface asperities. On the right hand side the value of μ is rather low. Under these conditions the load on the contact is fully carried by the lubricant which separates the surfaces totally. This zone is called the hydrodynamic lubrication regime, *HL*. The zone in between is called the mixed lubrication regime, *ML*. The load is partly carried by the surface asperities and partly by the pressurised lubricant.
According to the operational conditions of the forming process, μ can have a varying value during the process. The use of a model which describes the frictional behaviour in this way would be a large improvement for the simulations. It is possible to use a mathematical formula, obtained by curve fitting techniques, for the desired dependency of μ on the operational conditions.
With help of Figure 4-5 a description is given to find a suitable curve fit for μ as function of L. In this figure the Stribeck curve is represented by the fat line; the three straight help lines are represented by the dotted lines. The two horizontal help lines represent the value of μ for the boundary lubrication regime, μ_{bl} and for the hydrodynamic lubrication

regime, μ_{hl} The third help line touches the Stribeck curve at a μ exact between μ_{bl} and μ_{hl}. In this way two intersections of the help lines are found. These intersections are called the transition points. The first transition point L_{bl} gives the transition from the boundary lubrication regime to the mixed lubrication regime. The second transition point L_{hl} gives the transition from the mixed lubrication regime to the hydrodynamic lubrication regime. With aid of the transition points a formula can be derived for which the Stribeck curve is approximated. A suitable fit is defined by the following equation:

$$\mu(L) = \tfrac{1}{2}\left(\left(\mu_{bl} + \mu_{hl}\right) + \left(\mu_{bl} - \mu_{hl}\right) \tanh\left(\frac{\log\left(\frac{L^2}{L_{bl} \cdot L_{hl}} \right)}{\log\left(\frac{L_{bl}}{L_{hl}} \right)} \right) \right) \tag{4-18}$$

With μ_{bl} : boundary lubrication value of μ
μ_{hl} : hydrodynamic lubrication value of μ
L_{bl} : L at transition from boundary lubrication to mixed lubrication
L_{hl} : L at transition from mixed lubrication to hydrodynamic lubrication

With this expression the value of μ has become dependent on the local contact conditions as they are present in each single contact. For each application a measured Stribeck curve can be fitted and used as a pragmatic friction model for finite element simulations [Haar, 1996].

In case of the Stribeck friction, the expression for the contact slip tensor $\boldsymbol{Y}^C$ in the constitutive equation for the contact behaviour changes, because the coefficient of friction depends on the normal contact pressure. So, equation (4-8) changes to:

$$\dot{\phi}^C = 0 \quad \Rightarrow \quad \frac{\partial \phi^C}{\partial \boldsymbol{\tau}} \cdot \dot{\boldsymbol{\tau}} + \frac{\partial \phi^C}{\partial \mu} \frac{\partial \mu}{\partial \boldsymbol{\tau}} \cdot \dot{\boldsymbol{\tau}} = 0 \tag{4-19}$$

Since the change of the coefficient of friction during one time increment is very small, the second term of equation (4-19) can be neglected in the predictor. This means that equation (4-14) also holds for the Stribeck friction model. The only difference compared to the Coulomb friction model is that the slip cone must be updated in the corrector and at the end of every increment by calculating the coefficient of friction according to the Stribeck curve fit, equation(4-18) [Troelstra, 1996].

The implemented constitutive behaviour can be used with the two friction models. The coefficient of friction can have a constant value or it can have a varying value depending on the local contact conditions.

4.1.4 Examples Contact Behaviour

The influence of various parameters in the contact behaviour are explained with the help of a simple example. In this strip drawing example, a strip is clamped between a die and a blank holder and is pulled down around the die corner. The geometry of the example

problem is shown in Figure 4-6. The strip has a length of 100 mm and a width of 5 mm, it is modelled with 60 membrane elements. The strip has a prescribed displacement of 15 mm. The die corner has a radius of 10 mm, the blank holder force is 400 N. The default coefficient of friction is 0.16. The parameters which are studied are the contact stiffness, the damping and the friction model.

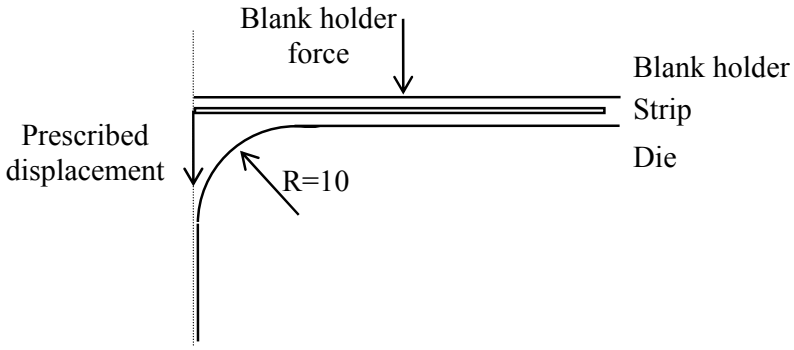

Figure 4-6 *Geometry of the strip drawing example.*

Contact stiffness

The first parameter which is studied is the contact stiffness. The contact stiffness defines the resistance against penetration into a body. Three simulations are performed: one with a contact stiffness of 10.0 MPa/mm, one with a contact stiffness of 20.0 MPa/mm and one with a contact stiffness of 100.0 MPa/mm. The contact stiffness can be interpreted as follows: when the contact pressure is in number equal to the stiffness the penetration is equal to 1 mm.

The result of the example is shown in Figure 4-7. This figure shows the x- and y-co-ordinates of the nodes in the die corner for the three contact stiffnesses. As can be seen for the low contact stiffness the curve is described differently than for the high contact stiffness. Because of the high penetration, it seems that an other die radius is followed by the strip. So, when the contact stiffness is too low, the tool geometry is not described accurately.

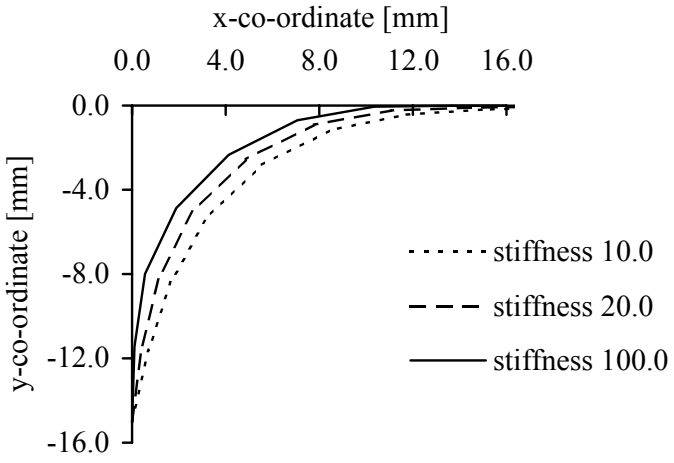

Figure 4-7 *Nodes in the die corner for different contact stiffnesses.*

Damping

The second parameter to be considered is the damping. The damping stabilises the open-closure behaviour. Again, three simulations are performed, the used damping values C_d are 0.5 MPa/mm, 1.0 MPa/mm and 2.5 MPa/mm. The contact stiffness for these simulations was 100.0 MPa/mm and the prescribed displacement increment was 0.4 mm.
Figure 4-8 shows the normal contact stress after 15 mm displacement at the top of the sheet as a function of the x-co-ordinate of the blank holder. At the co-ordinate 10, the die radius starts. At this point the strip loses contact with the blank holder. So, the normal contact stress should disappear. For a low damping value of 0.5 MPa/mm this happens, for the higher damping values of 1.0 MPa/mm and 2.5 MPa/mm is does not happen. Because of the large influence of the damping, a tensile stress appears at co-ordinate 10. For the damping value of 2.5 MPa/mm, the tensile stress is so large that, to obtain equilibrium, the normal contact stress under the blank holder is a more negative. In case of a too large damping value not only unwanted tensile stresses occur but also a deviant contact pressure is found.

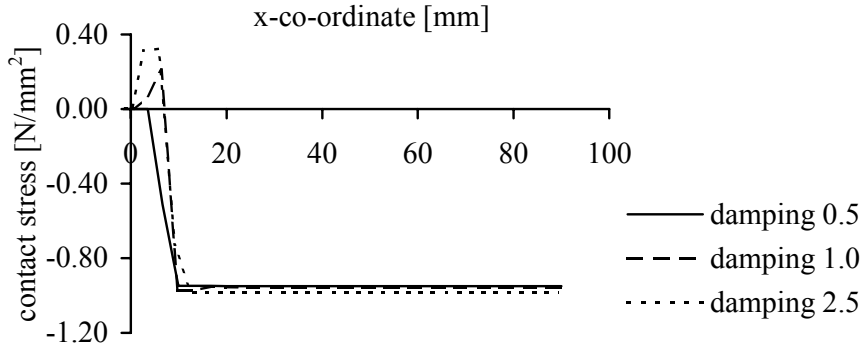

Figure 4-8 *Normal contact stress for different damping coefficients.*

Friction model

The friction model is treated as third parameter. Four simulations are performed, one with the Coulomb friction model and three with the Stribeck friction model. The simulations with the Stribeck friction model are performed with three different velocities: 2.5 mm/s, 5 mm/s and 10 mm/s. The blank holder force is increased to 700 N because for the default 400 N the differences were not significant. Figure 4-9 shows the shear stress in x-direction as a function of the x-co-ordinate at the die surface. When the curve for the Coulomb friction model is considered, it can be seen that in the blank holder area the shear stress is constant. At the die corner, the shear stress shows a peak of 1.40 N/mm^2. At the transition from the flat area to the die corner the shear stress drops to almost 0 N/mm^2. This drop is a result of a drop in the normal stress because of the element discretisation and the linearisation of the step.
When comparing the different simulations it can be seen that the shear stress in the blank holder area decreases for the Stribeck model for 2.5 mm/s and further decreases for larger velocities. Because of the increasing velocity the lubrication number L increases and therefore the coefficient of friction decreases.

The Coulomb friction model and the Stribeck friction model for 2.5 mm/s show the same peak value at the die corner. When increasing the velocity to 5.0 mm/s or even 10 mm/s, the peak value of the shear stress also decreases. The lubrication number L in the die corner decreases only for large velocities because of the higher contact pressure in the die corner. This in contrast to the blankholder area where the lubrication number already decreases for small velocities.

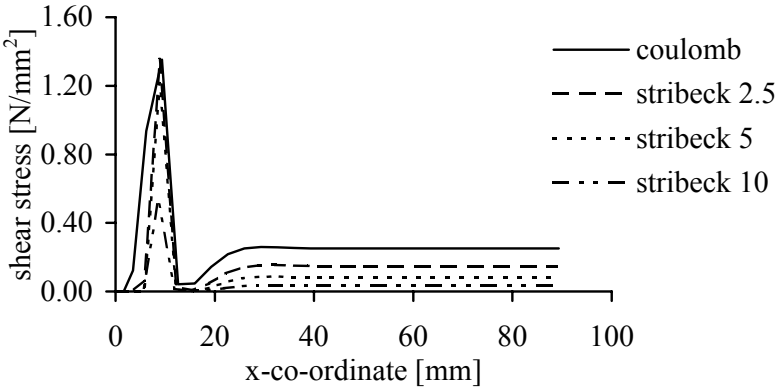

Figure 4-9 *Shear stress for different friction models and velocities.*

4.2 Tool Description

The tools in a finite element simulation are considered rigid because they are extreme stiff compared to the sheet. For this reason the tool can be presented as a surface only. In this work, two kinds of tool descriptions are discussed. The first description is an analytical one. This description is very useful for a simple tool geometry such as the tools for a rectangular or an axi-symmetric product. When the geometry of the tool becomes more complex the analytical description does not satisfy anymore. In order to model more complex surfaces a mesh description is used. This description is able to describe every arbitrary surface.

4.2.1 Analytical Description

In the analytical description, a surface is built up out from a number of standard shapes. The standard shapes can be described with relatively simple analytical equations. In three dimensional space, these standard shapes are planes, cylinders, toroids and spheres. Figure 4-10 shows an example of the tools for a rectangular product.
The punch shoulders are presented by cylinders, the punch corner is a part of a sphere, where the rest of the punch is described by planes. The die is built up the same way as the punch. Only the die corner is a part of a toroid.

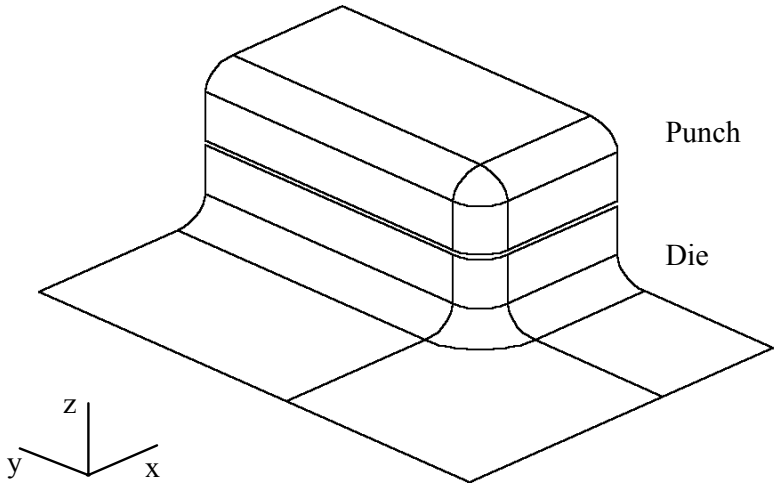

Figure 4-10 *Tool description for a rectangular product by standard shapes* [Vreede, 1992].

4.2.2 Mesh Description

One has to take into consideration that describing the surface of a complex product with the analytical description is a very hard job. For this kind of surfaces the mesh description is more practical. The elements of the mesh describe, depending on a certain tolerance, the tool surface. In Figure 4-11 a mesh of a die for a complex product is shown. As can be seen, small elements are used in curved areas, where in the flat areas larger elements are used.

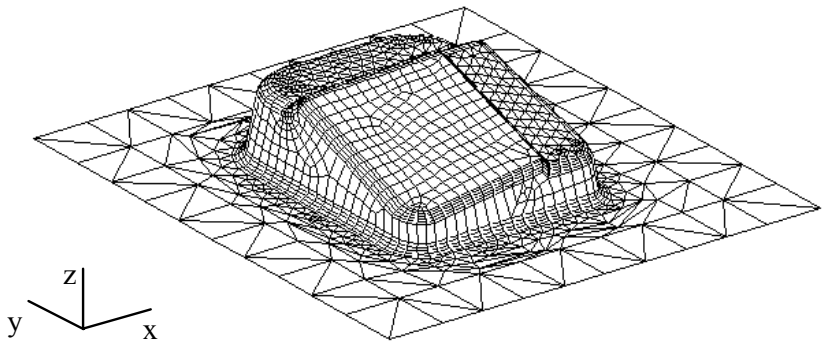

Figure 4-11 *Tool description for a complex product by elements.*

Because of the finite number of elements the surface is not completely smooth, a curve is described by a number of facets. The number of facets, this is the number of elements,

depends on the tolerance allowed. The movement of a node around a corner is piece wise straight, in contrast with the analytical description where the movement is much smoother. The lower the tolerance, the smoother the surface description and therefore the node movement. Hence, the number of elements increases considerably.

The tools for complex deep drawing parts are designed with help of CAD packages. The tool geometry is described with several surfaces of all kind of shapes. These CAD drawings can not be used for finite element applications at once. Generally, they are converted to a finite element mesh. The mesher creates large elements for flat areas and small elements for small radii. The result is a minimum of elements for a proper tool description. Because of the tolerances in the CAD-packages the surfaces are not always adjacent. This means that the mesh of the surfaces is also not adjacent.
Unfortunately, a lot of hand work still needs to be done to obtain a proper mesh. A first source of work are extremely small details which are not of interest for the forming process. Such details are meshed with a lot of elements which in fact have no meaning for the simulation. These details can be errased for the finite element simulation.
A second source of work are the non adjacent surfaces. In that case the tool surface can not be seen as a single surface. As a result overlap and holes can occur in the mesh. The mesh is a collection of meshes of the different non adjacent surfaces. When the connection between the different meshes is insufficient, the tool mesh or even the tool surface must be repaired by hand.

4.2.3 Examples Tool Description

Again, several simulations of the strip drawing example are treated. This time simulations with different tool descriptions are performed. In the first simulations the tool geometry is described by standard shapes. In the three other simulations the tool is described by a mesh. The die corner with a radius of 10 mm is described by 2, 3 and 5 elements respectively.
The result of this example is shown in Figure 4-12 and the tool description of the die corner is shown in Figure 4-13. The markers in this last figure coincides with the nodes of the tool elements. The standard shape is not plotted in the figure, but the standard shape is a quarter of a circle.
Figure 4-12 shows the x- and y-co-ordinate of the nodes in the die corner. Looking at the solution of the description with standard shapes, the nodes of the strip follow very neat the radius of 10 mm. For the mesh description with 2 elements, the strip nodes clearly differ from the standard shapes. Because of the rough description, the die corner is more an angular than a radius. The description with 3 elements shows less deviation, whereas the description with 5 elements compares very well with the standard shapes.

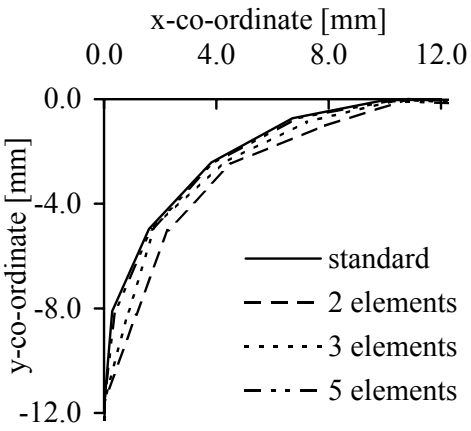

Figure 4-12 *Nodes in the die corner for different tool descriptions.*

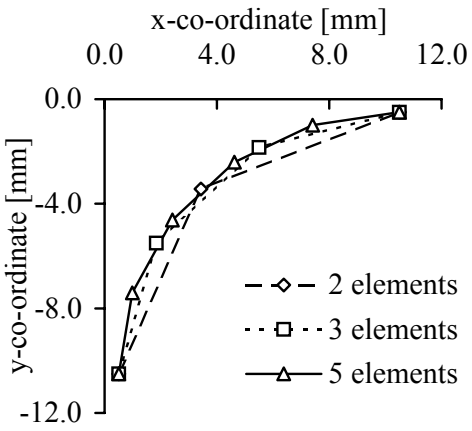

Figure 4-13 *Tool description of the die corner.*

4.3 Contact search

In 3D finite element formulations, the contact search is one of the major computational costs. As mentioned in section 4.1.1, a closest point projection is performed to detect the gap function and with that to detect contact. The gap function is the input for the contact model. This makes the contact search an important factor in the contact description. For every node of the sheet, a projection on the tool surfaces must be performed to obtain the gap function. Generally speaking, the slave nodes in contact with the master surface must be identified. The master surface is described with the analytical description or with the mesh description. So, every segment, standard shape or element, must be checked for possible contact. When the distance between each possible node-to-segment combination in the system is detected one speaks of the brute force method. This method is very robust but also extremely time consuming [Benson, 1990][Oldenburg, 1994].

In case of an analytical description a projection on every standard shape is performed. When the tool is described by elements a distance check is performed to select a number of elements for the projection.
For the distance check two types of search can be performed. The first type is based on searching the closest master node. This type of search is called the nodal search (section 4.3.1). The second type is based on searching the closest segments. This type of search is based on the pinball algorithm and is therefore called the pinball search (section 4.3.2). The exact place of contact is obtained by performing a normal projection on the selected master segments. The projection is explained in section 4.3.3.
For time effective reasons the contact search is divided into two logical steps, the global search and the local search. The local search checks the segments and performs the projection. The global search makes a first selection of a number of segments where the contact can take place. The global search performed here is a block search. This block search gives a considerable saving of time compared to the standard local search and is explained in section 4.3.4.

4.3.1 Nodal Search

This search is based on searching the closest node of the tool surface. For every node of the blank, the slave node, the distance to the nodes of the tool segment, the master nodes, is checked. The shortest node-to-node distance is the starting point for the projection.
A 2D sketch of the nodal search is given in Figure 4-14a. For every master-slave combination the distance is checked. The closest master node is used for determination of the exact place. The exact place is found by projection of the slave node on all the segments the closest master node is a member of. In Figure 4-14b the six checked segments are shown. The closest projection gives the exact contact point. This projection is explained later.

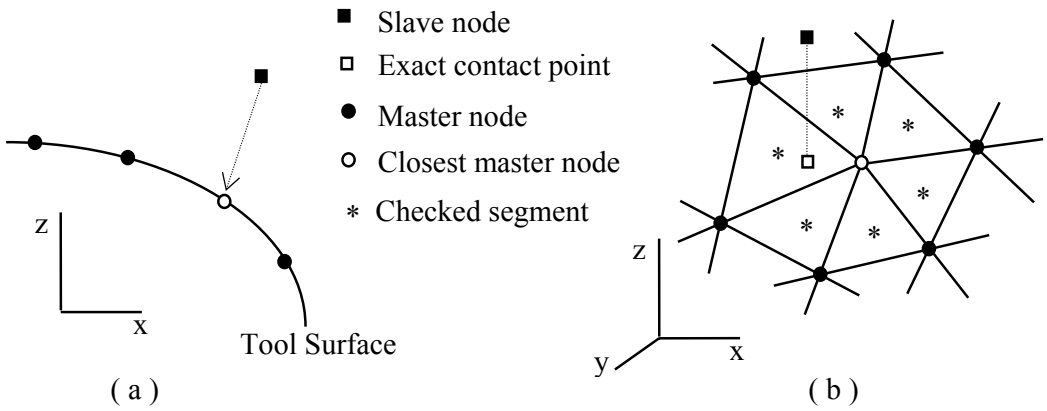

Figure 4-14 *The principal of the nodal search, searching the closest master node (a) and the exact projection (b).*

In case of non adjacent elements the nodal search can fail. The closest master node does not always offer the right segments to be checked. When the wrong segments are checked, the projected contact point is also wrong.
An example of a wrong nodal search with non adjacent elements is shown in Figure 4-15. Because of the non adjacent surfaces the segments of master group one and two are also non adjacent. The slave node is situated in the area of master group one. The closest master node is a node of master group two. So, only segments of master group two are checked which results in a wrong projection of the slave node.

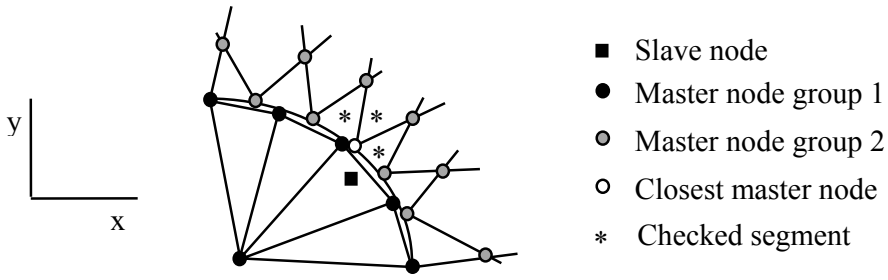

Figure 4-15 *Problems in nodal search because of non adjacent elements.*

Problems also occur when the segments of the mesh have widely different sizes or aspect ratios situated close to each other. This can happen at the transition from a flat area to a curved area. In a flat area large elements can be used where in a curved area small elements must be used. A slave node in the flat area can find a master node in the curved area to be the closest master node. This closest master node delivers the wrong segments to be checked and therefore the wrong exact contact point. An example of a wrong nodal search with different element sizes is shown in Figure 4-16.

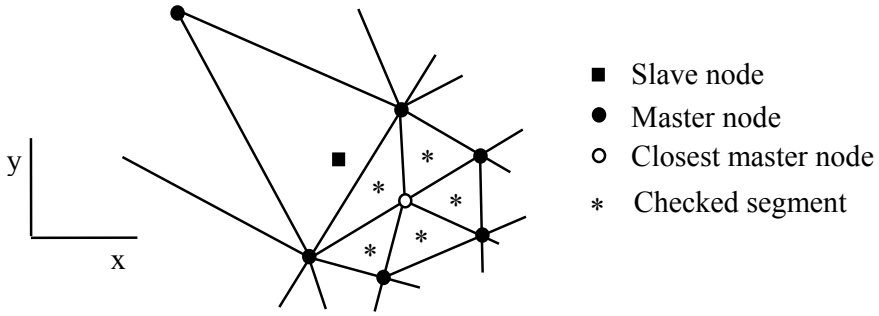

Figure 4-16 *Problems in nodal search because of different element sizes.*

4.3.2 Pinball Search

The nodal search does not always delivers the correct segments for the projection. It would be an improvement if the distance check directly checked the segments instead of the nodes. The pinball algorithm [Belytschko, 1991] is based on checking the segments. Around every master segment as well as around every slave node imaginary spheres are created. These spheres are designated as pinballs. The radius of the master pinball is denoted by R_{master}, whereas the radius of the slave pinball is denoted by R_{slave}. The principle of the pinball search is to check the distance between the slave node and the centre of the master segment.
The centre of the slave pinball is the slave node itself. The centre of the master segment is the centre of the circumscribed circle of the master segment. A 2D sketch of the pinball search is given in Figure 4-17. [Kerkhoff, 1995]

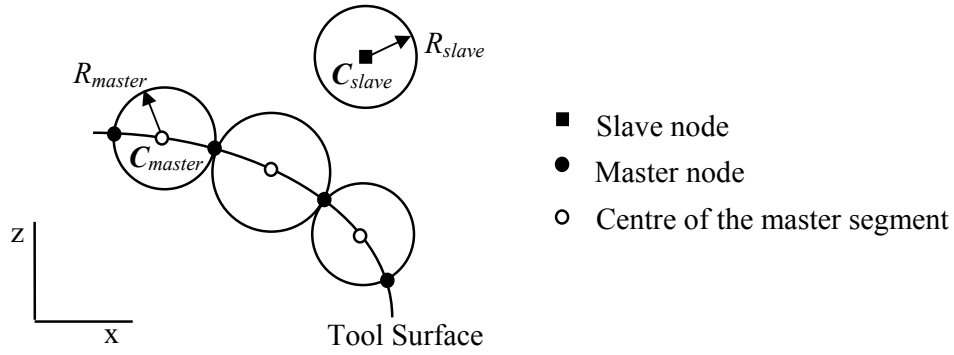

Figure 4-17 *The principal of the pinball search.*

If an overlap of these pinballs occurs, the segment belonging to the pinball is further taken into account for projection. Overlap is noticed when the distance between the centre of the slave pinball, $\boldsymbol{C}_{slave}$, and the centre of the master pinball, $\boldsymbol{C}_{master}$, is smaller than the sum R of the radii of these pinballs. In formula this can be written as:

$$\left\| \boldsymbol{C}_{slave} - \boldsymbol{C}_{master} \right\| < R \tag{4-20}$$

Where $\| \ \|$ denotes the Euclidean vector norm.

In contrast to Belytschko's method, the algorithm is used for a segment search instead of determination of the exact contact points. Another essential difference is the fact that the pinball size will vary during the simulation.
The pinball size is an important parameter for a well functioning contact search. It must not be too large because the pinball search is more often successful than necessary. But, it must not be to small either because it is necessary to observe contact in an early stage.

Slave Pinball
Firstly, the slave pinball is considered. The slave pinball is necessary to prevent missing the master segment. If the step size of the slave node is large compared to the master pinballs, the slave node can pass the master segment without contact detection (Figure 4-18).
The slave pinball is also used to prevent detecting a master segment too late. As mentioned in section 4.1, damping is applied for stabilising the open-closure behaviour of the contact. So, the master segment must be detected at a distance larger than g_{damp} before the slave node is in contact. It is possible that the slave node has a displacement path where the contact is detected too late to apply damping effectively (Figure 4-18).

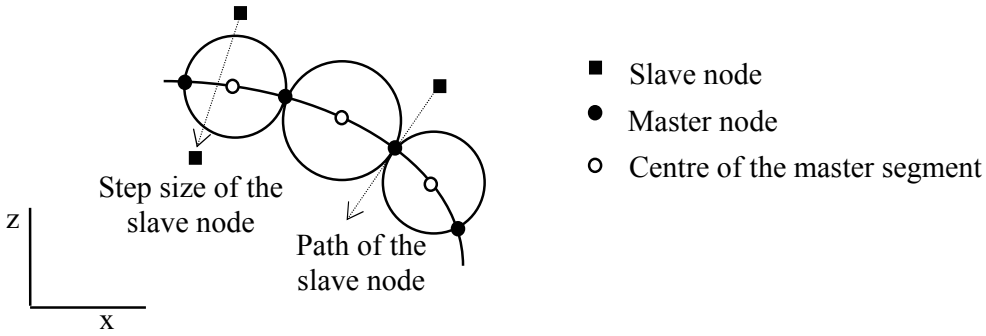

Figure 4-18 *Necessity of a pinball around the slave node.*

For the slave pinball, two phases can be distinguished. In the first phase, the pre-contact phase, the slave node is not in contact with a master segment. During this phase the radius is set at a start value equals to g_{damp}. This minimum radius of the slave pinballs is enlarged with the nodal displacement to prevent missing contact during large displacements.
In the second phase, the post-contact phase, the slave is in contact. During this phase the radius of the pinball is set to the nodal displacement increased with the penetration g into the master surface. The slave can penetrate the master surface because of the penalty method used in the contact algorithm. The slave pinball radius is set:

$$R_{slave} = \Delta U_{node} + g_{damp} \quad : \text{pre} - \text{contact}$$
$$= \Delta U_{node} + \|g\| \quad : \text{post} - \text{contact} \tag{4-21}$$

Master pinball

Secondly, the master pinball is considered. The master pinball radius exists of a constant value and a variable value, equation (4-22).

The constant value R_0 depends on the segment size. The centre of the pinball and the pinball radius are constructed in such a way that the pinball radius is as small as possible. But the sphere must contain the whole segment.

The variable value of the radius depends on the displacement of the tool. This pinball enlargement is necessary because possible contact will be missed if the tool displacement is large compared to the pinball size. The master pinball size is:

$$R_{master} = R_0 + \Delta U_{tool} \tag{4-22}$$

The slave pinball radius and the master pinball radius are updated in every increment. The sum of the pinball radii is:

$$R = R_{slave} + R_{master} \tag{4-23}$$

With this R the pinball search according equation (4-20) is performed. After having checked all necessary master pinballs, a set of segments is obtained where the slave node can be in contact. With these segments the projection is executed. If no overlap with any pinball is found, no contact occurs.

4.3.3 Projection

In order to obtain the exact contact point, projections on the selected master segments are performed. The closest projection is the exact contact point. The projection algorithm is explained with the help of Figure 4-19.

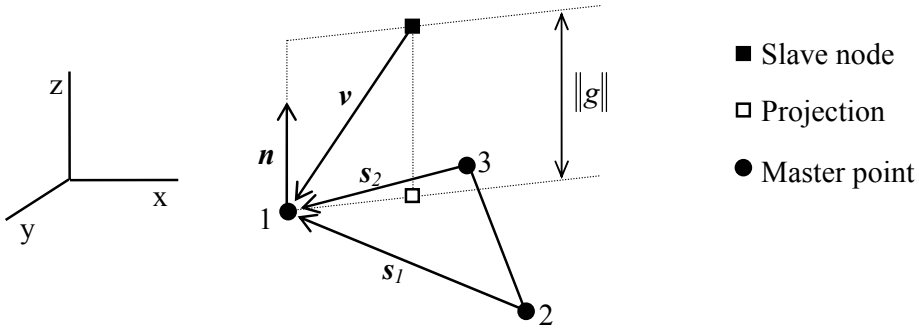

Figure 4-19 *Projection of a slave node on a master segment.*

The slave node will be projected on the master segment 123. Therefore, the normal, $\boldsymbol{n}$, is determined with help of the vectors $\boldsymbol{s}_1$ and $\boldsymbol{s}_2$:

$$\boldsymbol{n} = \boldsymbol{s}_1 \times \boldsymbol{s}_2 \tag{4-24}$$

The projection distance is defined by the scalar product of the vector $\boldsymbol{n}$ and the vector $\boldsymbol{v}$:

$$g = \boldsymbol{v} \cdot \boldsymbol{n} \tag{4-25}$$

The exact place of contact is determined with help of the projection distance, g, and the co-ordinates of the slave node:

$$\boldsymbol{c}_{contact} = \boldsymbol{c}_{slave} - g\boldsymbol{n} \tag{4-26}$$

The exact place of contact is in the plane of the segment 123. It must be checked if the projection is in the segment 123. When not, the projection is replaced to the closest side of the master segment. This is necessary because the master segment might be a boundary of the master surface.
Even when the master segment is no boundary, the projection must be replaced on the master side. A 2D example is given in Figure 4-20.

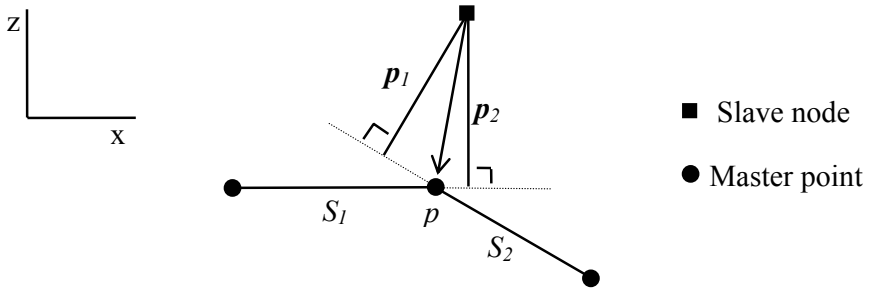

Figure 4-20 *Replacing the projection to a side of the master segment.*

The slave node is projected on two masters segments which are adjacent but not in the same plane. Both projections $\boldsymbol{p}_1$ and $\boldsymbol{p}_2$ are not inside the master segment. These projections are not satisfactory. Therefore, the projection is placed to point p at the side of the master segment. This gives indeed the closest projection of the slave node on the master surface.

4.3.4 Block Search

Sometimes the tool description exists of many segments. In that case the local search must be carried out so often that the computational cost is enormous. Therefore a first selection of the master nodes or master segments is performed. This first selection is called the global search. The global search performed here is a block search. The block search is based on the work of [Atzema, 1994] and [Heinstein, 1993].

The master surface is divided into a number of blocks. The number of blocks depends on the level of division. At level zero the complete master surface is surrounded by one block. When increasing one level, the block is divided into four sub-blocks. These sub-blocks are generated by calculating the mid-point of the block and divide it into left-right and top-bottom. This division can be repeated by further increasing the level. The level is denoted by l, so each level contains of 4^l blocks. The level of division is chosen in such manner that at the highest level only a few masters are in one block. An example of a block division into two levels is given in Figure 4-21.

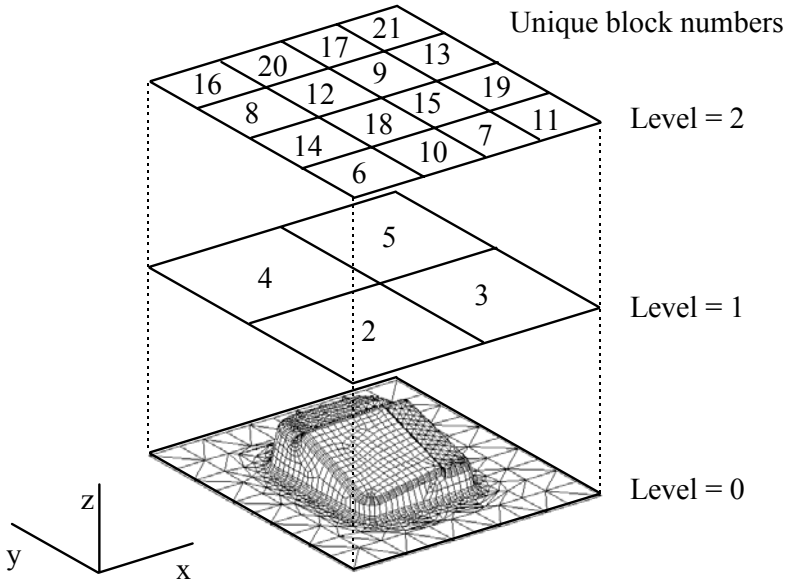

Figure 4-21 *Block division of a tool into two levels with unique global block number.*

Each block regardless of the level, has a unique global block number. This unique number, m, is assigned to a block using the following summation:

$$m = 1 + \sum_{l=1}^{l\max} n(l)\, 4^{l-1} \tag{4-27}$$

Where $n(l)$ is a local number at each level which runs from 1 to 4:

$$n(l) = 1 + i_x(l) + 2\, i_y(l) \tag{4-28}$$

The parameters i_x and i_y depend on the position of the block edges and the subscript *middle* denotes the middle of the block:

$$\begin{aligned} x_{edge} < x_{middle} &\Rightarrow i_x = 0 \\ x_{edge} \geq x_{middle} &\Rightarrow i_x = 1 \\ y_{edge} < y_{middle} &\Rightarrow i_y = 0 \\ y_{edge} \geq y_{middle} &\Rightarrow i_y = 1 \end{aligned} \tag{4-29}$$

In Figure 4-21 also the unique block numbers are shown.

The next step is to sort the masters in block order. The masters differ according to the search that is used. In case of the nodal search the master nodes are sorted, in case of the pinball search the centres of the master segments are sorted. The masters are sorted in such a way that at each level they are sorted sequentially. For every block, on every level, it is very easy to find the masters it contains. Also switching from one level to the other level is a simple operation. This sort must performed only once because of the rigid tools. An example of an array of arbitrary masters is given in Figure 4-22.

Masters	Level 0 block number	Level 1 block number	Level 2 block number
21			6
45			10
43		2	
3			14
89			18
23	1		7
65			11
95		3	15
1			
34			19
13			

Figure 4-22 *Array of masters sorted in block order.*

Theoretically, the block search can be performed. Depending on the co-ordinates of the slave node and the level of division, a block is selected. The global search is only performed with the masters of the selected block. In practice the algorithm appeared not sufficient robust.

In order to obtain a robust algorithm, it is not sufficient to treat the block the slave is in. The right contact segment can be overlooked because of the slave node displacement, the penetration of the slave node and the block crossing segments. A block crossing segment is a segment that crosses the block boundary. Therefore a window is constructed around a slave node. The window size shows a lot of similarity with the pinball enlargement. The size of the window w depends on the slave node and on the master surface:

$$w = w_{slave} + w_{master} \tag{4-30}$$

The contribution of the slave node depends on the displacement of the slave node, ΔU_{slave}. Further, difference is made in the pre-contact phase and the post-contact phase. In the pre-contact phase the window size is enlarged with g_{damp}, whereas in the post-contact phase the window size is enlarged with the penetration into the master surface:

$$\begin{aligned} w_{slave} &= \Delta U_{node} + g_{damp} \quad : pre-contact \\ &= \Delta U_{node} + \|g\| \quad : post-contact \end{aligned} \tag{4-31}$$

The contribution of the master surface depends on the displacement of the master surface, ΔU_{master} and the maximum size of the segments of the master surface S_{master}. In case of the nodal search the maximum segment length is S_{master}, and in case of the pinball search the maximum pinball radius *is* S_{master}.

$$w_{master} = \Delta U_{master} + S_{master} \tag{4-32}$$

The window is constructed by creating four window corners around the slave node at w and $-w$ in x and y direction. The block search is performed with the co-ordinates of the window corners. The block level is decreased until the block size is larger than the window size.
The window can only be in four blocks at the same time and these four blocks are always adjacent. If the window corners are in different blocks, all these blocks are used in the global search.

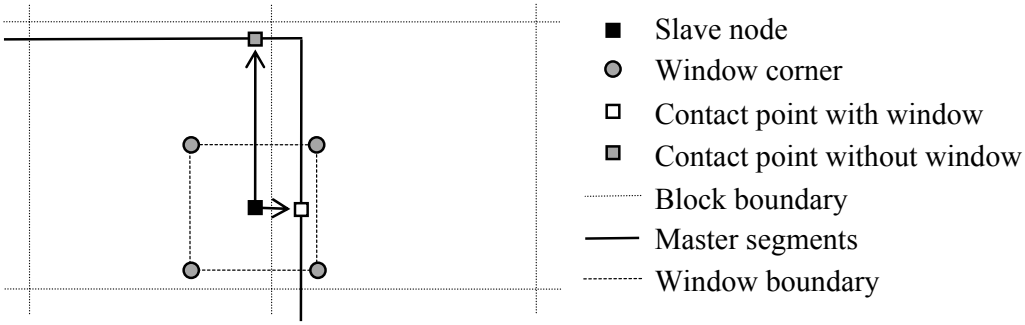

Figure 4-23 *Use of a window in the block search.*

An example of the need of a window is given in Figure 4-23. When searching only in the block the slave node is in, a contact point inside the block is found. But this projection is not the closest projection. By checking the blocks of the window corners, the block right from the slave node is also checked. In this block, another projection is found which is much closer than the contact point found without window projection.
In this case the wrong projection was found but it is very well possible that while missing the right master segment, the contact will be missed as well.

4.3.5 Examples Contact Search

As an example for the search algorithm the tool surface of a complex product is used. The tool surface is already shown in Figure 4-11 and Figure 4-21. Because of the proper tool description all search methods give the right exact contact point. But the time to obtain the contact point differs. Table 4-1 shows the necessary time to perform the contact search for the different types of search. The two search types, nodal and pinball, are performed in combination with the block search with different levels.
The brute force pinball search takes most of the time and is the reference time. The brute force nodal search is almost two times faster. The reason is that the pinball search needs more overhead like determining the variable pinball size.

When using the block search, the search time decreases with an increasing level. Again the nodal search is faster than the pinball search. For high block levels the saving of time is not so large anymore. The nodal search with block level 3 needs the same time as the with block level 4. This is caused by the window used for robustness. Because of the large size of this window compared to the block size at this level, the search switches one level up and has to perform more searches than expected. Further increasing the level does not make any sense since the level will be switched up so often that time will increase again.

Search type	Time (normalised)
Nodal	0.527
Nodal with block level 1	0.162
Nodal with block level 2	0.133
Nodal with block level 3	0.123
Nodal with block level4	0.123
Pinball	1.000
Pinball with block level 1	0.575
Pinball with block level 2	0.310
Pinball with block level 3	0.215
Pinball with block level 4	0.178

Table 4-1 *Computer time to perform a contact search on a complex product.*

4.4 Concluding Remarks

The contact description with all its facets is treated in this chapter. The contact behaviour depends on the physical parameters such as the coefficient of friction as well as on the numerical parameters such as the contact stiffness and the damping. This numerical parameters must be chosen very carefully.
The tool surfaces can be described with help of two tool descriptions. A description based on standard shapes for geometric simple tool shapes. A description based on elements for complex tool shapes.
The determination of the exact place of contact is important in order to simulate the forming process successfully. It is also one of the major computational costs. For time effective reasons a block search can be performed. The distance check can be performed in two ways, the nodal search and the pinball search. The exact place of contact is obtained by performing a normal projection.

4.5 References

[Atzema, 1994]
Atzema, E. H., *Formability of sheet metal and sandwich laminates*, PhD-thesis, University of Twente, 1994

[Belytschko, 1991]

Belytschko T., M. O. Neal, *Contact-impact by the pinball algorithm with penalty and Lagrangian methods*, Int. J. Num. Meth. Eng., 31, 547-572, 1991

[Benson, 1990]
Benson D. J., J. O. Hallquist, *A single surface contact algorithm for the post-buckling analysis of shell structures*, Comp. Meth. Appl. Mech. Eng., 78, 141-163, 1990

[Haar, 1996]
Haar R. ter, *Friction in sheet metal forming, the influence of (local) contact conditions and deformation*, PhD-thesis, University of Twente, 1996

[Heinstein, 1993]
Heinstain M. W., S. W. Attaway, J. W. Segle, F. J. Mello, *A general contact detection algorithm for finite element analysis*, Contact Mechanics, computational techniques, M. H. Aliabadi & C. A. Brebbia (eds.), Computational mechanics publications, Southampton, 1993

[Kerkhoff, 1995]
Kerkhoff M. D. P., *A modified pinball contact algorithm for deep drawing simulations based on CAD data*, Graduate report, University of Twente, 1995

[Lugt, 1986]
Lugt J. van der, J. Huétink, *Thermal-mechanical coupled finite element analysis in metal forming processes,* Comp. Meth. Appl. Mech. Eng., 54, 1986

[Oldenburg, 1994]
Oldenburg M., L. Nilsson, *The position code algorithm for contact searching*, Int. J. Num. Meth. Eng., 37, 359-386, 1994

[Simo, 1992]
Simo J. C., T. A. Laursen, *An augmented lagrangian treatment of contact problems involving friction*, Comp. Struc., 42, 97-116, 1992

[Schey, 1983]
Schey J. A., *Tribology in metalworking, friction , lubrication and wear,* ASM Metals Park, Ohio, 1983

[Schipper, 1988]
Schipper D. J., *Transitions in the lubrication of concentrated contacts*, PhD-thesis, University of Twente, 1988

[Stoker, 1994]
Stoker H. C., *Analysis of the simulation of deep drawing*, Graduate report, University of Twente, 1994

[Troelstra, 1996]
Troelstra C., *Friction in deep drawing simulations, implementation of the Stribeck curve in the finite element code DIEKA*, Graduate report, University of Twente, 1996

[Vreede, 1992]

Vreede P.T., *A finite element method for simulations of 3-dimensional sheet metal forming*, PhD-thesis, University of Twente, 1992

5. Drawbeads

The flow of the material during the deep drawing process is controlled by the blank holder geometry and the blank holder load. In order to increase the formability, these two aspects can be optimised. But they are global control tools. A widely used method to locally control the material flow is the application of drawbeads.
Drawbeads are placed in the blank holder/die area. A drawbead consists of a bead attached to the blank holder or the die face. This bead fits into a groove or contra bead on the opposing face (Figure 5-1). The drawbead forces the blank material to bend and unbend several times while it is pulled through the bead. This bending and the friction generate a restraining force. By placing a drawbead wherever a restraining force is needed makes it a suitable tool to control the material flow.

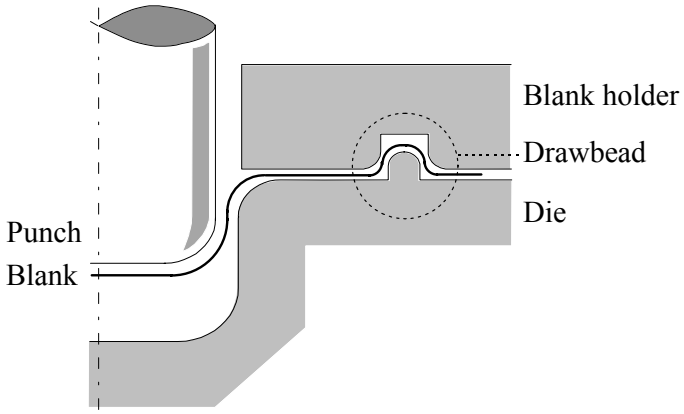

Figure 5-1 *Principle of the deep drawing process with a drawbead.*

In order to get more insight in the drawbead behaviour, 2D numerical analyses have been performed. These analyses give information on the drawbead restraining force, the friction stress and the strain changes in the sheet. A set of experiments has been performed to verify the 2D analyses. The 2D drawbead model is treated in section 5.1.
In 3D simulations of the deep drawing process, the drawbead geometry is seldom included because of the small radii. These small radii require a very large number of elements and therefore large computer time. For this reason an equivalent drawbead has been developed which replaces the geometry by a numerical algorithm. The equivalent drawbead is treated in section 5.2.

5.1 2D Drawbead Model

For studying the drawbead behaviour a 2D plane strain model has been developed in the finite element code DIEKA. This code has the possibility to use a mixed Eulerian-Lagrangian formulation, a combination of the Updated Lagrangian formulation and the Eulerian formulation [Huétink, 1986].
The Updated Lagrangian formulation is commonly used in solid mechanics. The grid points move with the material. It can easily describe history dependent properties like strain hardening. Besides, free surfaces can be followed in a natural way. A restriction of the Updated Lagrangian formulation is the limited deformation range because the element mesh is likely to be distorted, resulting in a loss of accuracy and convergence.
The Eulerian formulation is commonly used in fluid dynamics, the material flows through a fixed grid. An advantage of this method is that grid will never be distorted in spite of great displacements. To incorporate history dependence, material path lines must be determined along which the evolution equations must be integrated. The shape of a free surface cannot change during the simulation.
In order to avoid the above mentioned problems with both the Updated Lagrangian formulation and the Eulerian formulation a mixed Eulerian-Lagrangian formulation has been applied. In this formulation the locations of the nodal points are not updated according to the displacements of the material but are decoupled. However, they are not fixed in the space. With this formulation it is possible to keep a neat mesh and describe free surfaces as well.

To study the drawbead behaviour, two drawbead geometries have been used, a bead with a round cross section and a bead with a rectangular cross section (Figure 5-2a and Figure 5-2b, respectively). Both beads have the same height and width, they only have different radii. The contra bead is also identical for both configurations. The dimensions in mm are given in Figure 5-2.

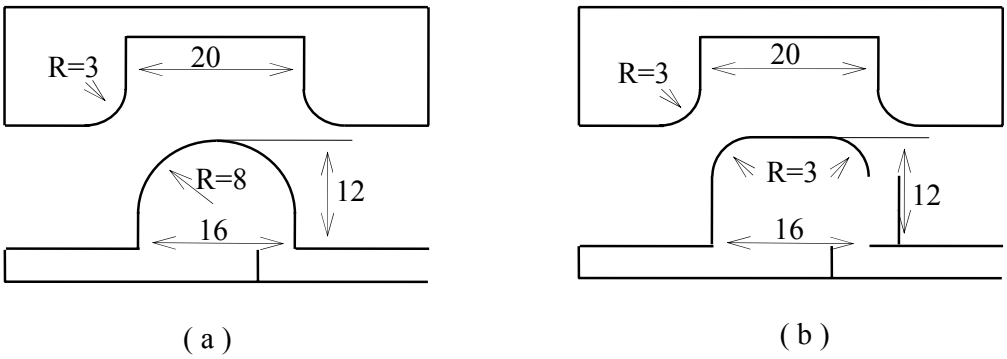

Figure 5-2 *Drawbead geometry of a round bead (a) and of a rectangular bead (b).*

Initially, the simulations were started with a flat sheet, like in reality. By closing the blank holder, the sheet was deformed between the bead and the contra bead. Later on, it turned out that the calculation time could be reduced with a pre-deformed sheet in the drawbead. Not modelling the initial closing of the drawbead had hardly any influence on the results [Beugels, 1993].

In the simulations the mixed Eulerian-Lagrangian formulation has been used. The mesh was fixed in flow direction. Imagine an observer of the drawbead who sees how the material flows through the drawbead. In the direction perpendicular to the flow the mesh was free to move.
The advantage of this formulation is that the grid refinements remain at their place and the effects of sheet thinning can be described as well. Besides, there is no need to model a large mesh in contrast to a Lagrangian formulation where the sheet can be pulled out of the drawbead.
The sheet was modelled with four layers of four node plane strain elements. The initial meshes of both drawbead configurations are shown in Figure 5-3. The mesh refinements can be distinguished at the radii of the drawbead.
To describe the contact between the sheet and the drawbead, contact elements were used. These contact elements are also depicted in Figure 5-3. When no contact occurs the contact element are also projected onto the drawbead contour. This projection gives an indication of the drawbead geometry.

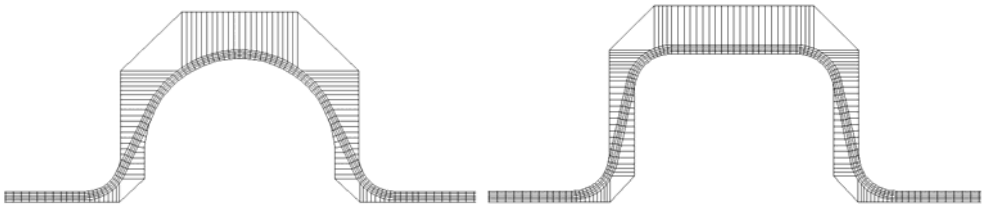

Figure 5-3 *Initial meshes of the round bead (a) and the rectangular bead (b).*

The stress strain curve is fitted with the Nadaï formula. The material behaviour is described with the Von Mises yield funtions. The material properties of a low carbon steel were used:
Ludwik value (C) = 551 N/mm^2
n-value (n) = 0.230
initial yield stress = 149 N/mm^2

The blank thickness was 0.7 mm whereas the clearance between die and blankholder was 0.9 mm. A constant coefficient of friction of 0.16 was applied.

The sheet was given a prescribed displacement; the left end was pulled to the left. Figure 5-4 shows the deformed meshes of both drawbead configurations. Comparing the initial meshes with the deformed meshes the use of the mixed Eulerian-Lagrangian formulation can be seen. The elements of the sheet only moved perpendicular to the flow; in the flow direction, the elements remained at their place.
At the first radius of the contra bead the sheet increases its bending radius because of the bending resistance. When looking at the rectangular bead, the sheet loses contact at the flat top of the bead. Because of the bending resistance the sheet can not follow the sharp bead radius and is lifted.

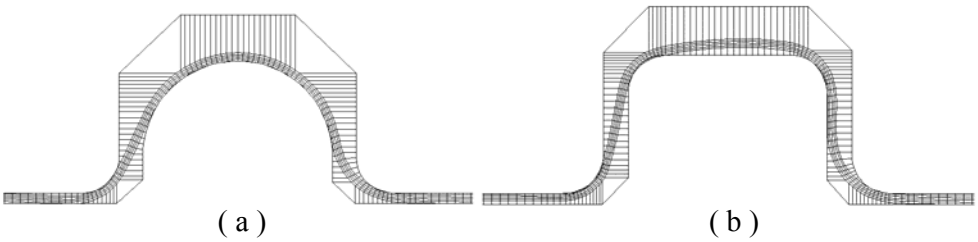

Figure 5-4 *Deformed meshes of the round bead (a) and the rectangular bead(b).*

5.1.1 Numerical Results

The main results of the 2D drawbead simulations are discussed in this section. The force to pull the sheet through the drawbead and the friction stress acting on the sheet are considered. Further the tangential strain distribution and the equivalent plastic strain distribution will be considered.

Pulling force
The force to pull the strip through the drawbead as a function of the sheet displacement is given in Figure 5-5. Because of the plane strain model the pulling force is a force per unit width. Although after a few mm already eighty percent of the stationary pulling force is reached, the stationary value is reached when a material particle has passed the entire drawbead [Cao, 1993]. The stationary value is reached after pulling the sheet approximately 35 mm. The stationary value in case of the round bead is 85.1 N and in case of the rectangular bead it is 149.3 N.
The resistance of the sheet to move through a drawbead is caused by friction and by the bending and unbending cycle of the strip. Firstly, the frictional part is considered, secondly the bending part is considered with help of the tangential strain.

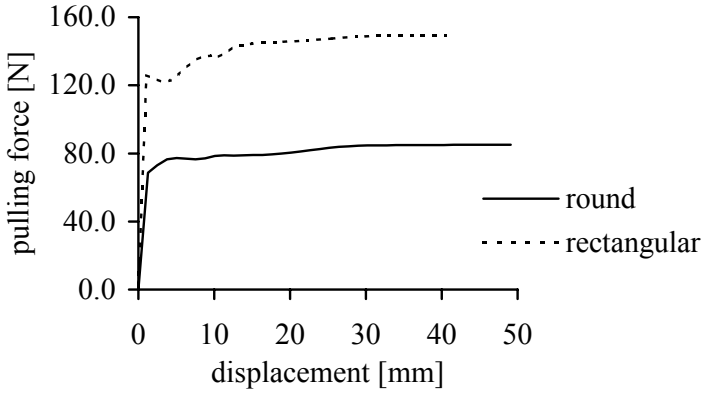

Figure 5-5 *Drawbead pulling force for the round bead and the rectangular bead.*

Friction stress
The friction stresses acting on the sheet at the bead and at the contra bead for both the round bead and the rectangular bead are printed in Figure 5-7 and Figure 5-8 respectively. The friction stresses are printed as a function of the position in the sheet. The position

starts at 0 mm at the right end of the drawbead and runs through the sheet to the left end of the drawbead to 60 mm (see also Figure 5-6).

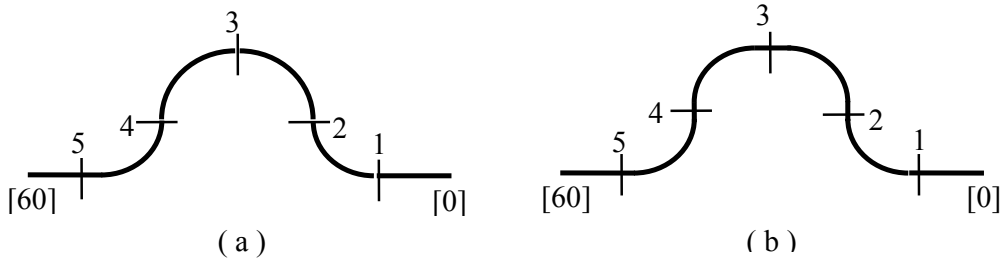

Figure 5-6 *Drawbead position (between brackets) and drawbead locations for the round bead (a) and the rectangular bead (b).*

The sheet and the tools have contact in a few small zones because of the constant clearance between the die and the blank holder.
The friction stress at the contra bead shows an identical trend for both drawbead configurations. The contact between the contra bead and the sheet occurs at the small radii. The peaks in the friction stress are caused by the peaks in the contact pressure which in turn are caused by the bending of the sheet. The peak at the position 50 mm, the exit of the bead, is larger than the peak at the position 10 mm because of the extra tension in the sheet.
In comparing the friction stresses for both bead configurations, a few differences can be distinguished. The contact zone with the bead in case of the round bead is relatively large, the sheet is in contact with the whole top surface. But the friction stress is not uniform in the contact area. At the beginning and at the end, small peaks can be distinguished. The contact zone with the bead in case of the rectangular bead is more localised. The contact is limited to the radii of the bead and in the flat area no contact occurs. At the contra bead both drawbead configurations show the same friction stress distribution. Two peaks can be distinguished at the radii of the contra bead. The smallest peak is situated at the entrance of the drawbead.

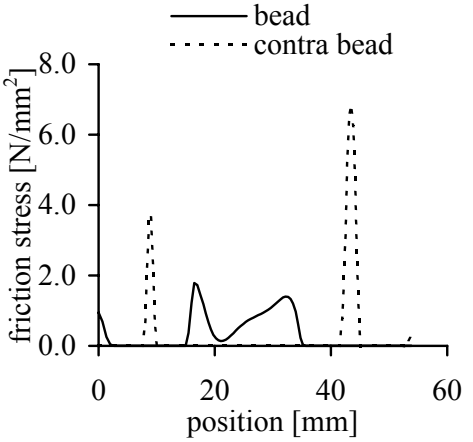

Figure 5-7 *Friction stress as a function of the position for the round bead.*

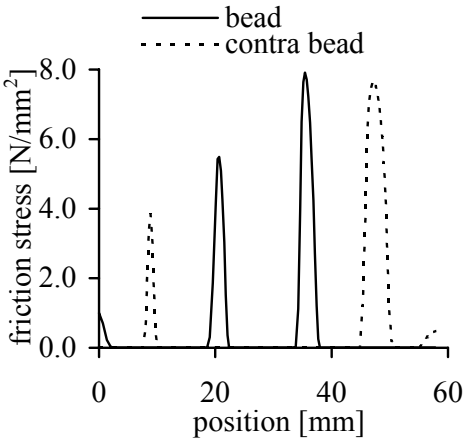

Figure 5-8 *Friction stress as a function of the position for the rectangular bead*

Tangential strain

When a sheet passes a drawbead it is being bend and unbend. These deformations result in a tangential strain in the strip. Figure 5-9 and Figure 5-10 show the tangential strain of the sheet for the round bead and rectangular bead respectively. The strain of the lower face, mid plane and upper face are printed as a function of the position in the sheet. The vertical dotted lines indicate the locations in the drawbead as defined in Figure 5-6. Tangential strains larger than zero indicate stretching, values smaller than zero indicate compression.

Focusing on the round bead, Figure 5-9, the following strain distribution can be distinguished. Shortly after location 1 the sheet bends around the first radius of the contra bead. The lower face is stretched whereas the upper face is compressed. At position 15 mm, the sheet unbends and directly bends the other way around on the bead. Between location 2 and 4, the sheet slides around the bead. In this zone the upper face is stretched and the lower face is compressed. At position 37 mm, the sheet unbends. A small zone of stretching can be distinguished; the sheet is stretched between the bead and the contra bead. Between location 4 and 5 the sheet is bend around the second radius of the contra bead. At the end of the radius the sheet unbends and the strain is uniform over the thickness. During the flow through the drawbead the mid plane is elongated due to a tensile stress and due to the shift of the neutral plane.

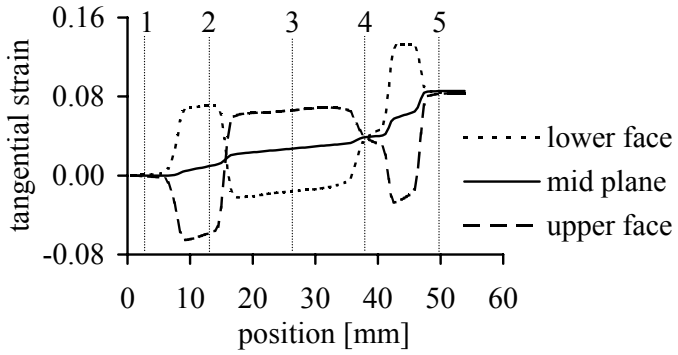

Figure 5-9 *Tangential strain distribution in the sheet at the sheet faces and in the mid plane for the round bead.*

The strain distribution of the rectangular bead can be seen in Figure 5-10. Again shortly after location 1 the sheet bends around the first radius of the contra bead. At location 2 the sheet bends around the first radius of the bead. After the radius, the sheet unbends. A zone with a more or less uniform strain distribution over the thickness can be distinguished. This zone represents the flat top of the bead where location 3 lies. At position 35 mm the sheet bends around the second radius of the bead. At location 4, a zone of stretching can be distinguished. The sheet is stretched between the radius of the bead and the contra bead. This stretching zone is larger than in case of the round bead because of the smaller radius of the bead. Between location 4 and 5, the sheet bends around the second radius of the contra bead. At the end, the sheet unbends.

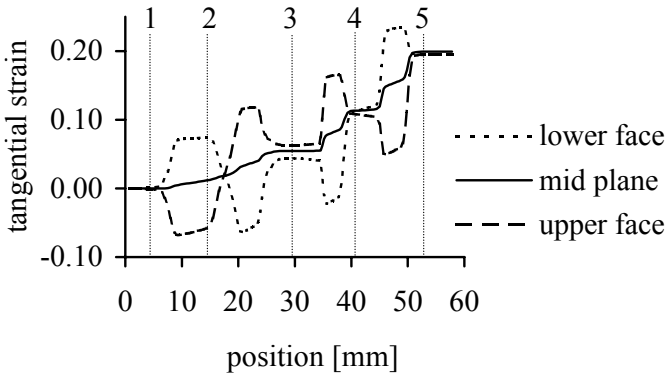

Figure 5-10 *Tangential strain distribution in the sheet at the sheet faces and in the mid plane for the rectangular bead.*

Equivalent plastic strain

The equivalent plastic strain at the exit of the bead, location 5, as a function of the sheet displacement is given in Figure 5-11. For both drawbead configurations the equivalent plastic strain increases with an increasing displacement until the stationary value is reached. The stationary value for the round bead is 0.23 and for the rectangular bead 0.42. The sharper bending because of the sharper bead radii result in a larger value for the equivalent plastic strain for the rectangular bead.

The first large slope from 5 mm till 15 mm is caused by the material which only passed the second radius of the contra bead. The more or less constant value from 15 mm till 25 mm is caused by the material which started in the bead area and passed the second contra bead radius. The second slope from 25 mm till 35 mm is caused by the material which passed both radii of the contra bead. The stationary value is reached after pulling the sheet 35 mm. It is reached when a material particle passed the whole drawbead.

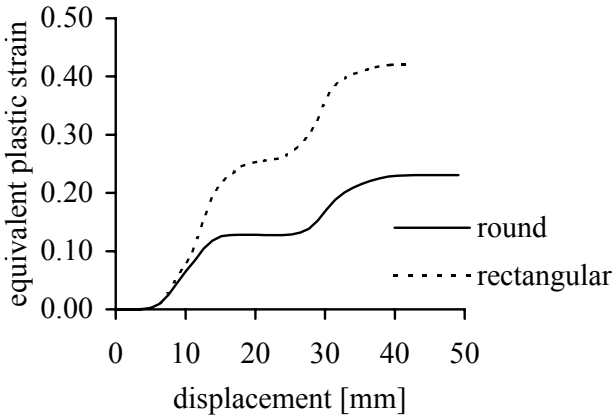

Figure 5-11 *Equivalent plastic strain for the round bead and for the rectangular bead.*

5.1.2 Experimental Results

Experiments were performed to verify the 2D numerical analyses; they were performed on a fully equipped Erichsen press. The experimental set up looks like the deep drawing principle of Figure 5-1. The significant geometrical difference between the finite element simulations and the experiments is the extra die shoulder radius as a consequence of using a deep drawing press.
The material used in this study was a deep drawing steel with the mechanical properties as listed in section 5.1.1. The dimensions of the sheet were 50*500 mm. Throughout the experiments the sheets were prepared with the long side oriented in rolling direction. The surface roughness of the tools was about 0.25 μm. The applied lubricant was a deep drawing oil with a viscosity of 0.04 Pa·s at room temperature. The blanks were lubricated on both sides with the help of a paint roller. The punch speed was kept constant at 3 mm/s.

After performing the experiments, the thickness of the sheet was measured. The measuring locations were identical to the locations used in the numerical model and are indicated in Figure 5-6. Since in the measuring area a plane strain state is assumed and the material behaves almost incompressible, the tangential strain has the same value (except for the sign) as the thickness strain. The result of the thickness measurements are plotted as positive values in Figure 5-12. To verify the numerical model the tangential strain distribution of the mid plane of Figure 5-9 and Figure 5-10 are also plotted in Figure 5-12.
At the entrance and at the exit of the drawbead the results compared very well. In the drawbead itself small differences occured. The resulting tangential strains found in the experiment and in the model were 0.080 and 0.085 respectively in case of the round bead, and 0.190 and 0.198 respectively in case of the rectangular bead.

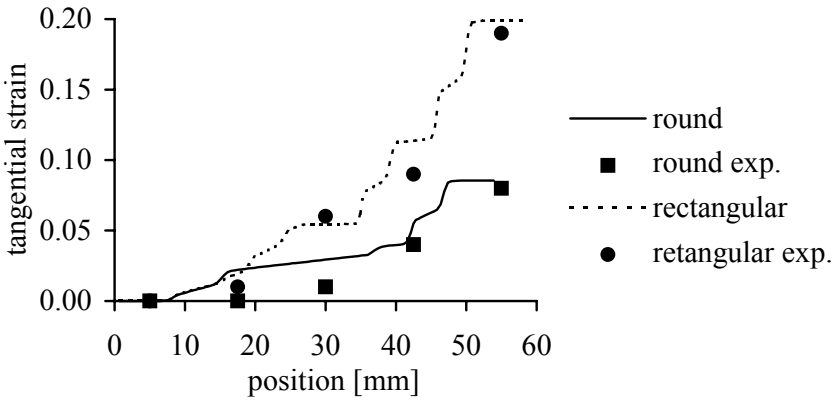

Figure 5-12 *Measured and calculated tangential strains for the round bead and the rectangular bead.*

In order to compare the restraining force an additional 90° bend was calculated. The pulling force found in the drawbead calculations was applied as an initial load on the 90° bend. The initial conditions for the 90° bend, like thickness and equivalent strain distribution, were obtained form the drawbead simulations. Summons of the drawbead pulling force and the additional bend form the total force which can be compared with the

measured punch force. The measured punch force is expressed per unit width and because of the symmetry in the simulations halved. Now, the total force can be compared with the measured punch force. The results are collected in Table 5-1. Looking at the last two columns of the values agree fairly well. The simulated values are a fraction higher.

Geometry	Drawbead force	Total force	Measured force
round	85	118	106
rectangular	149	205	195

Table 5-1 *Comparison of the pulling force for model and experiment.*

The evident agreement between the simulations and the experiments indicate the reliability of the model. It can be concluded that the material and the friction were reasonably well modelled. The used elements and meshes were sufficiently accurate in describing the deformation of the sheet. The 2D drawbead model proved to be a useful tool to predict the effects of a drawbead.

5.2 Equivalent Drawbead

In 3D finite element simulations the drawbead geometry is seldom included because of the small radii. These small radii require a very large number of elements and therefore large computer time. For this reason equivalent drawbeads are used.
Equivalent drawbeads are defined as fixed lines on the tool surface. On these lines the drawbead restraining force acts. This force is assigned through a 2D simulation of the drawbead or through an experiment. Although the restraining force reaches its stationary value when a material particle passed the whole drawbead most finite element programs use the steady state value.

Different strategies were used for the equivalent drawbead in finite element programs. In ABAQUS the drawbead restraining force was applied as a set of frictional forces [Taylor, 1993]. A concentrated normal load was applied along the drawbead line and a drawbead coefficient of friction was used. The normal load was chosen so that the tangential friction force matched the steady state restraining force.
In PAM-STAMP the tangent restraining force was a sum of the resistance of bending and the resistance of friction [Haug, 1991]. The bending resistance depended on the geometry of the drawbead, its penetration depth and the sheet material. The sliding resistance was a function of the drawbead coefficient of friction and the normal force.
ITAS-3D uses an other strategy [Kawka, 1994]. The drawbead restraining force introduced some additional stiffness. The non-symmetrical drawbead stiffness matrix was not assembled into the global stiffness matrix but introduced an incremental drawbead force.

However, the effect of the drawbead is much more than adding a restraining force to the sheet, see section 5.1 and [Wouters, 1994]. During the flow of the material through a drawbead the material usually becomes thinner and the material properties are modified in a significant manner. Modelling drawbeads by only applying an additional restraining force does not incorporate these effects. For this reason an equivalent drawbead has been developed which incorporates the effects of sheet thinning and the change of the strain distribution. Both the restraining force and the strain are history dependent. Their value is

a function of the material which already passed the drawbead. The model is fed by a curve fit which in turn is gained from a 2D drawbead simulation or an experiment.
An explanation of the implementation of the equivalent drawbead in DIEKA is discussed in the rest of this section.

The equivalent drawbead is defined as a line on the tool surface. If an element passes the drawbead line, the force acts on the normal component of the material flow. The tangential component of the material flow does not give any contribution. Therefore the material flow v is split in a normal component v_n and a tangential component v_t, see Figure 5-13. For the equivalent drawbead only the normal component is taken into account. The drawbead co-ordinates are defined as the x_{db}-axis normal to the drawbead line and the y_{db}-axis tangential to the drawbead line. The y_{db}-axis is the plane strain direction of the 2D analysis.
The implementation of the drawbead restraining force is straight forward and is treated in section 5.2.1. The implementation of the drawbead strain is more complicated. At this point two strategies can be followed. The first strategy is based on a stress estimation because of the drawbead strains and is treated in section 5.2.2. The second strategy adds constraints to obtain the drawbead strains. This approach is treated in section 5.2.3.

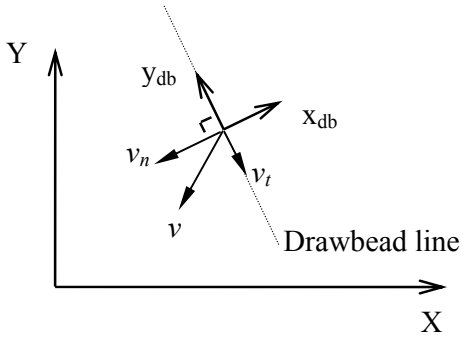

Figure 5-13 *Drawbead co-ordinate system.*

5.2.1 Drawbead Restraining Force

The restraining force acts normally to the drawbead line opposite the normal material flow. This additional force is taken into account at the right hand side of the finite element equations as a body force. The force is assigned to the nodes of the elements which have passed the drawbead line.

$$\boldsymbol{K} \cdot \Delta\boldsymbol{u} = \Delta\boldsymbol{f} + \boldsymbol{f}_{db} \tag{5-1}$$

With: $\boldsymbol{K}$: stiffness matrix
$\Delta\boldsymbol{u}$: displacement increment
$\Delta\boldsymbol{f}$: force increment
$\boldsymbol{f}_{db}$: drawbead restraining force

The drawbead restraining force per element $\boldsymbol{f}_{db}^{elem}$ is calculated by integrating the drawbead force per unit width over the length of the elements in the drawbead line:

$$\boldsymbol{f}_{db}^{elem} = \int_{l^{elem}} f_{db}\, dl \tag{5-2}$$

5.2.2 Drawbead Strain Prediction based on Stress Estimation

In the first strategy, the drawbead is modelled as an extra stiffness term in the finite element equations:

$$\left(\boldsymbol{K} - \boldsymbol{K}_{db}\right) \cdot \Delta\boldsymbol{u} = \Delta\boldsymbol{f} \tag{5-3}$$

With: $\boldsymbol{K}$: stiffness matrix
$\boldsymbol{K}_{db}$: drawbead stiffness matrix
$\Delta\boldsymbol{u}$: displacement increment
$\Delta\boldsymbol{f}$: force increment

The drawbead stress estimation is based on splitting the left side of equation (5-3):

$$\boldsymbol{K} \cdot \Delta\boldsymbol{u} - \boldsymbol{K}_{db} \cdot \Delta\boldsymbol{u} = \Delta\boldsymbol{f} \tag{5-4}$$

or

$$\boldsymbol{K} \cdot \Delta\boldsymbol{u} = \Delta\boldsymbol{f} + \boldsymbol{K}_{db} \cdot \Delta\boldsymbol{u} \tag{5-5}$$

The drawbead stiffness term can be rewritten in drawbead stresses:

$$\boldsymbol{K} \cdot \Delta\boldsymbol{u} = \Delta\boldsymbol{f} + \int_{V} \boldsymbol{B}^{T} \cdot \boldsymbol{\sigma}_{db}\, dV \tag{5-6}$$

To calculate the last term in equation (5-6) an estimation of the drawbead stresses must be performed. The following equations must be solved to estimate the drawbead stresses:

$$\dot{\boldsymbol{\sigma}}_{db} = \left(\boldsymbol{E} - (1-h)\boldsymbol{Y}\right) : \dot{\boldsymbol{\varepsilon}}_{db} \tag{5-7}$$

With: $\boldsymbol{E}$: elasticity tensor
$\boldsymbol{Y}$: yield tensor
h : hardening rate

Equation (5-7) is the general constitutive equation for elastic plastic material with isotropic hardening. The starting point to solve this equations is the configuration as displayed in Figure 5-14.

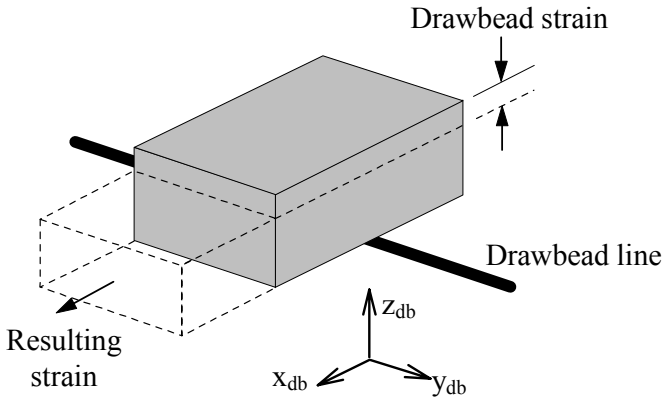

Figure 5-14 *Initial configurations for stress estimation*

The material that passes the drawbead line becomes thinner. The material only becomes longer in x_{db}-direction because of the plane strain assumption in y_{db}-direction. The shear stresses are neglected. The thickness of the material is very small compared to its other dimensions. So, a plane stress situation is assumed.

As mentioned above the boundary condition for this problem are:

$$\begin{aligned} \dot{\boldsymbol{\sigma}}_{dbz} &= 0 && \text{: plane stress in } z_{db}\text{-direction} \\ \dot{\boldsymbol{\varepsilon}}_{dby} &= 0 && \text{: plane strain in } y_{db}\text{-direction} \\ \dot{\boldsymbol{\varepsilon}}_{dbz} &= \dot{\boldsymbol{\varepsilon}}_{db} && \text{: strain fit value for the drawbead strain} \end{aligned} \tag{5-8}$$

Equation (5-7) reduces with the boundary conditions of equation (5-8) to three equations with three unknowns. Before solving the equations, the components of the elasticity tensor, the yield tensor and the hardening rate will have to be dealt with.

The components of the elasticity tensor are written as:

$$\left[E_{ij}\right] = \begin{bmatrix} 2G+l & l & l \\ l & 2G+l & l \\ l & l & 2G+l \end{bmatrix} \tag{5-9}$$

Where G is the shear modulus and l is the constant of Lamé as defined in equation (2-31).

A general expression for the yield tensor is:

$$\boldsymbol{Y} = \frac{\boldsymbol{E}:\frac{\partial\phi}{\partial\boldsymbol{\sigma}}\frac{\partial\phi}{\partial\boldsymbol{\sigma}}:\boldsymbol{E}}{\frac{\partial\phi}{\partial\boldsymbol{\sigma}}:\boldsymbol{E}:\frac{\partial\phi}{\partial\boldsymbol{\sigma}}} \tag{5-10}$$

Where ϕ is the yield function.

Because of the incompressibility of the plastic material behaviour and the plane strain assumption, the following equation is found:

$$\left.\begin{array}{l}\sum\limits_{i=x,y,z}\dfrac{\partial\phi}{\partial\sigma_{dbi}}=0\\ \dfrac{\partial\phi}{\partial\sigma_{dby}}=0\end{array}\right\} \quad \frac{\partial\phi}{\partial\sigma_{dbx}} = -\frac{\partial\phi}{\partial\sigma_{dbz}} \tag{5-11}$$

Working out equation (5-10) with the assumption of equation (5-11), the components of the yield tensor are:

$$\left[Y_{ij}\right] = \begin{bmatrix} G & 0 & -G \\ 0 & 0 & 0 \\ -G & 0 & G \end{bmatrix} \tag{5-12}$$

The expression for the hardening rate is defined as:

$$h = \frac{\frac{\partial\phi}{\partial\lambda}}{\frac{\partial\phi}{\partial\lambda} - \frac{\partial\phi}{\partial\boldsymbol{\sigma}}:\boldsymbol{E}:\frac{\partial\phi}{\partial\boldsymbol{\sigma}}} \tag{5-13}$$

Where $\frac{\partial\phi}{\partial\lambda}$ depends on the yield stress and the hardening function.

So, equation (5-7) can be solved by substitution of the equations (5-9), (5-12) and (5-13) and using the boundary conditions of equation (5-8). The estimated stresses σ_{dbx} and σ_{dby} are substituted into equation (5-6) to describe the drawbead strain in the equivalent drawbead.

Summarising the equivalent drawbead model it exists of two components. First, the prescribed force resists the element of sliding too fast through the drawbead. Second, the prescribed strain implemented with help of a stress estimation elongates the element. Because of this elongation and the plane strain assumption the element becomes thinner. A graphical presentation of the force distribution in an element because of the equivalent drawbead is given in Figure 5-15.

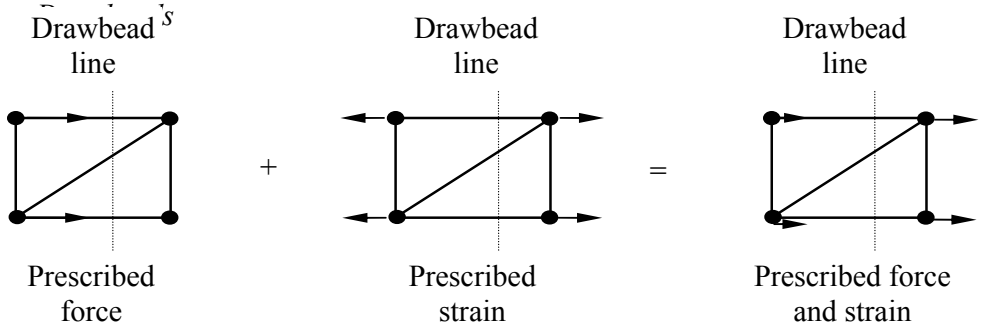

Figure 5-15 *Graphical presentation of the force distribution for the equivalent drawbead.*

5.2.3 Drawbead Constraint

In the second strategy, the drawbead strain prediction is modelled as an extra stiffness term and an extra drawbead force in the finite element equations:

$$\left(\boldsymbol{K} - \boldsymbol{K}_{db}\right) \cdot \Delta\boldsymbol{u} = \Delta\boldsymbol{f} + \boldsymbol{f}_{dbc} \tag{5-14}$$

With: $\boldsymbol{K}$: stiffness matrix
$\boldsymbol{K}_{db}$: drawbead stiffness matrix
$\Delta\boldsymbol{u}$: displacement increment
$\Delta\boldsymbol{f}$: force increment
$\boldsymbol{f}_{dbc}$: drawbead constraint force

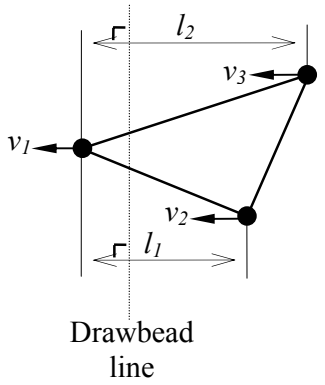

Figure 5-16 *Basis of the drawbead constraint approach.*

The configuration of Figure 5-16 is the basis of the drawbead constraint approach. The perpendicular length of the element sides which cut the drawbead line are defined as l_1 and l_2 respectively. In order to achieve the prescribed drawbead thickness strain the element must be elongated. In this model the thickness strain and the elongation are equal because of incompressibility. To obtain the elongation, the nodal displacements v_1, v_2 and v_3 must fulfil some constraint conditions. The element sides between node 1 and 2 and between node 1 and 3 must elongate Δl_1 and Δl_2 respectively. In mathematical form:

$$\begin{bmatrix} -1 & 1 & 0 \\ -1 & 0 & 1 \end{bmatrix} \cdot \begin{Bmatrix} v_1 \\ v_2 \\ v_3 \end{Bmatrix} = \begin{Bmatrix} \Delta l_1 \\ \Delta l_2 \end{Bmatrix} \tag{5-15}$$

In short notation:

$$\boldsymbol{A} \cdot \boldsymbol{v} = \boldsymbol{r} \tag{5-16}$$

The matrix $\boldsymbol{A}$ is a non-symmetric matrix. The least square method is used to obtain a symmetrical matrix. For the least square method the following equation must be solved:

$$(\boldsymbol{A} \cdot \boldsymbol{v} - \boldsymbol{r})^2 = \text{minimal} \tag{5-17}$$

The minimum with respect to $\boldsymbol{v}$ is found by solving:

$$\frac{\partial}{\partial \boldsymbol{v}} (\boldsymbol{A} \cdot \boldsymbol{v} - \boldsymbol{r})^2 = 0 \tag{5-18}$$

Which gives:

$$\boldsymbol{A}^T \boldsymbol{A} \cdot \boldsymbol{v} = \boldsymbol{A}^T \cdot \boldsymbol{r} \tag{5-19}$$

The symmetric drawbead stiffness matrix $\boldsymbol{A}^T\boldsymbol{A}$ is written as $\boldsymbol{K}_{db}$ and the drawbead constraint force $\boldsymbol{A}^T \cdot \boldsymbol{r}$ is written as $\boldsymbol{f}_{dbc}$. This results in a following equation which can be substituted into equation (5-14):

$$\boldsymbol{K}_{db} \cdot \boldsymbol{v} = \boldsymbol{f}_{dbc} \tag{5-20}$$

Writing out the components of equation (5-20) gives:

$$E_{db} \begin{bmatrix} 2 & -1 & -1 \\ -1 & 1 & 0 \\ -1 & 0 & 1 \end{bmatrix} \cdot \begin{Bmatrix} v_1 \\ v_2 \\ v_3 \end{Bmatrix} = E_{db} \begin{Bmatrix} -\Delta l_1 - \Delta l_2 \\ \Delta l_1 \\ \Delta l_2 \end{Bmatrix} \tag{5-21}$$

The system of equations is weighted with a penalty parameter. The penalty parameter must be large enough to characterise the drawbead behaviour. But is must not be too large because of dominating the solution of the total system. A value equal to the maximum of the diagonal of the element stiffness matrix works very well.

Because of the incremental formulation, an element passes a drawbead during some increments. Hence, the elongation of the element must not be applied at once. The elongation is scaled with step size $\|\boldsymbol{v}\|$ and the element length perpendicular to the drawbead line l.

The step size is unknown yet so the step size of the previous increment $\|\boldsymbol{v}^{i-1}\|$ is used as a prediction for it. In fact the step size can be written implicitly, but this gives a strongly non linear behaviour. In this phase of the research this first prediction works very satisfactory. So, the drawbead constraint for increment *i* results in the following equation:

$$E_{db}\begin{bmatrix} 2 & -1 & -1 \\ -1 & 1 & 0 \\ -1 & 0 & 1 \end{bmatrix} \cdot \begin{Bmatrix} v_1^i \\ v_2^i \\ v_3^i \end{Bmatrix} = E_{db}\frac{\|\boldsymbol{v}^{i-1}\|}{\|l\|}\begin{Bmatrix} -\Delta l_1 - \Delta l_2 \\ \Delta l_1 \\ \Delta l_2 \end{Bmatrix} \tag{5-22}$$

If the mechanical unbalance ratio is not sufficiently small, the displacement is recalculated in an iteration process. In the continuing iteration, the matrix $\boldsymbol{K}_{db}$ is unchanged but the right hand side $\boldsymbol{f}_{db}$ differs. Consider an element side which must elongate Δl. In the previous iterations, it is already Δl^{iter-1} elongated. So, the elongation for this iteration is:

$$\Delta\Delta l^{iter} = \Delta l - \Delta l^{iter-1} \tag{5-23}$$

So in the continuing iterations the corrected elongation $\Delta\Delta l$ replaces Δl in the right hand side of equation (5-21).

A graphical presentation of the force distribution and the additional stiffness term of the equivalent drawbead is given in Figure 5-17. The difference with the equivalent drawbead described in section 5.2.2 is the added stiffness terms in the stiffness matrix. The stiffness terms are presented as springs.

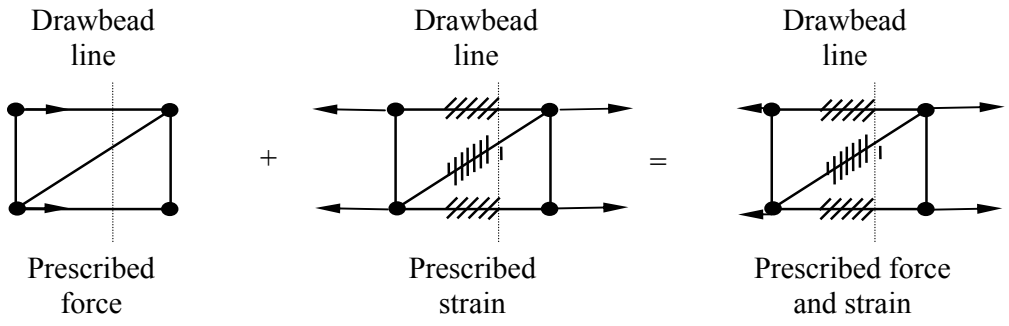

Figure 5-17 *Graphical presentation of the force distribution and the additional stiffness terms for the equivalent drawbead with help of constraints.*

5.2.4 Examples Equivalent Drawbead

In this section, an example of the equivalent drawbead is performed. The applied drawbead is the round bead discussed in section 5.1. The drawbead force and the drawbead strain are history dependent and imported by curve fits of the 2D numerical results. The curve for the force is directly obtained from the 2D simulation. For the strain curve this was not possible. The curve for the strain is obtained from combining the equivalent plastic strain history and the stationary thickness strain. It seemed that scaling the equivalent plastic strain curve on the stationary thickness strain gave a good reproduction of the real thickness strain history [Meinders, 1996]. Figure 5-18 shows the force and the strain from the 2D drawbead model and their fits.

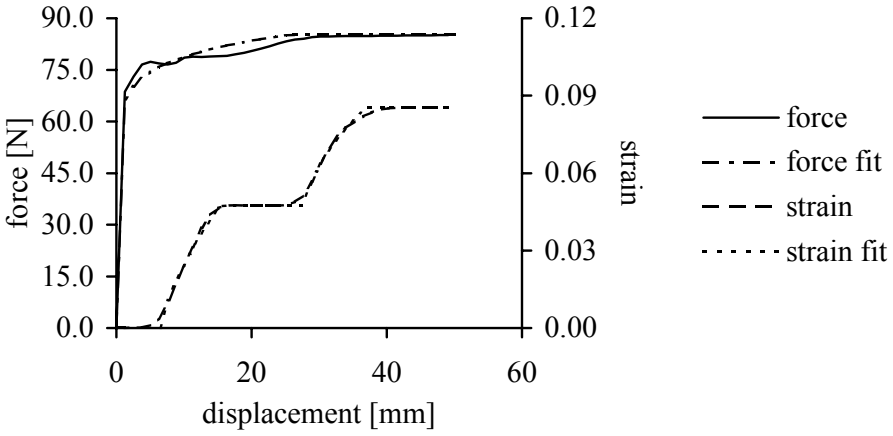

Figure 5-18 *The force fit and the strain fit for the equivalent drawbead*

The drawbead force is fitted by a power law. When the curve fit reaches the steady state value, that value is taken into account.

$$f_{db} = 65 \cdot d^{0.083} \quad \text{till } f_{steady\,state} = 85.1 \tag{5-24}$$

The fit for the strain is more complicated. It exists of two slopes and two plateau's. The two slopes are fitted by a power law and the two plateau's are lines. The fit is split in two parts depending on the displacement d:

$$\begin{aligned} \varepsilon_{db} &= 0.01 \cdot d^{0.714} && \text{till } \varepsilon_{steady\,state} = 0.047 \quad \text{for } d < 27.5 \\ \varepsilon_{db} &= 0.047 + 0.01 \cdot d^{0.606} && \text{till } \varepsilon_{steady\,state} = 0.085 \quad \text{for } d \geq 27.5 \end{aligned} \tag{5-25}$$

Other fit functions are possible and recommended. But in this phase of the research the above mentioned fit works satisfactory.

The drawbead is applied on the deep drawing of a rectangular product. The initial blank size was 442 mm x 626 mm. The punch size was 200 mm x 400 mm and the punch displacement was 80 mm. Because of the symmetry only one quarter of the product has been simulated. The simulation has been performed with 2000 membrane elements. Figure 5-19 shows the initial mesh and the deformed mesh. The lines of symmetry are also depicted.

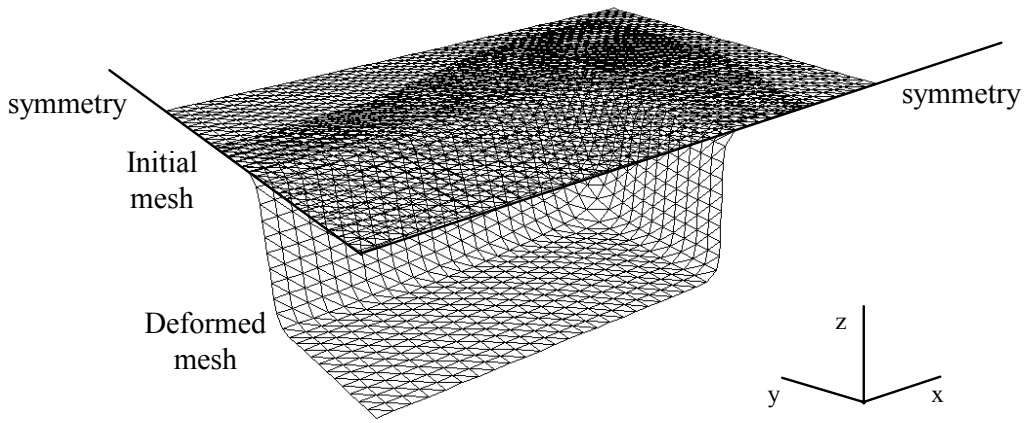

Figure 5-19 *The initial mesh and the deformed mesh of the rectangular product.*

Three deep drawing simulations of the rectangular product are performed. The first simulation is without a drawbead. In the second simulation only the drawbead restraining force is applied. In the third simulation both the restraining force and the strain changes are applied. The force fit and the strain fit of Figure 5-18 are used. The drawbead is positioned at a y-co-ordinate of 127 mm at the long side of the product parallel to the x-axis. The drawbead length is 200 mm.
In Figure 5-20 the flange outline of the three simulations as well as the initial blank outline are shown. The initial undeformed flange outline is a rectangle at an x-co-ordinate of 313 mm and at an y-co-ordinate of 221 mm. The deformed flange outlines show the draw-in at the x-axis and the y-axis, and the forming of a tip at the corner of the product.
It is clearly that the flange outline of all simulations is different. Comparing the two simulations with the drawbead and the simulation without a drawbead the following can be observed. The draw-in of the position of the drawbead is less than the draw-in without drawbeads. At the x-axis it is the other way around. Because of the different draw-in the tip of the blank is rotated.
Comparing the two simulations with the drawbead the draw-in of the simulation with the prescribed force and strain is smaller than the draw-in of the simulation with only the prescribed force. The material is more elongated because of the prescribed strain and consequently less draw-in occurs.

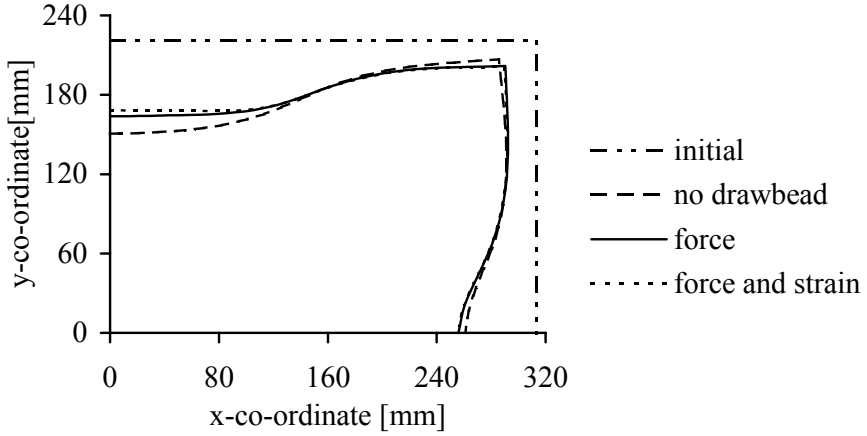

Figure 5-20 *The flange outlines of the simulations of the rectangular product.*

The thickness strain distribution along the y-axis is printed in Figure 5-21. The simulation without drawbead shows a smooth characteristic. In the simulations with the drawbead more thickness reduction is found than in the simulation without the drawbead. Under the punch, co-ordinate distance 0 mm till 100 mm, a constant strain of -0.055 is found for both simulations with the drawbead. In the up-right side of the product, 100 mm till 200 mm, some differences occur. The simulation with the prescribed force and strain shows more thickness reduction than the simulation with only the prescribed force. For the simulation with only the prescribed force the largest thickness reduction of -0.062 is found at the punch corner, co-ordinate distance 100 mm. For the simulation with the prescribed force and strain the largest thickness reduction of -0.075 is found just after the die rounding, co-ordinate distance 180 mm.

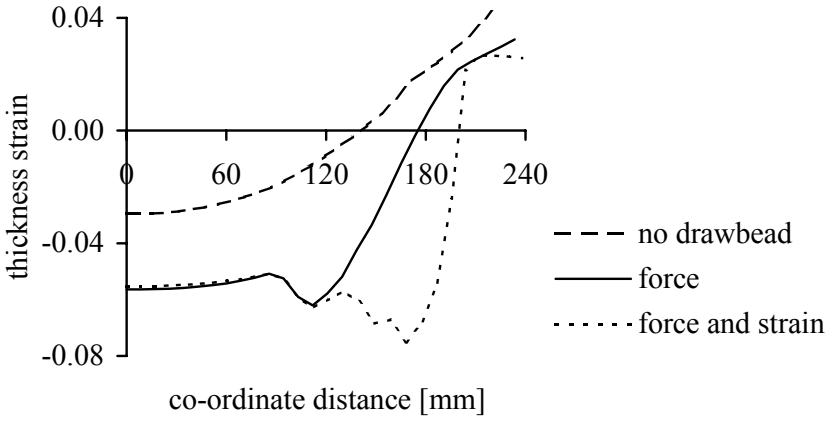

Figure 5-21 *Thickness strain distribution along the y-axis for the rectangular product.*

In the simulation with only the prescribed force the sheet is stretched between the punch rounding and the drawbead. A constant membrane force acts in that part of the sheet. The maximum thickness reduction occurs at the punch rounding, because this is the area which is in the stretching part during the whole forming process. In the simulation with the prescribed force and strain, the sheet is also stretched. Moreover the drawbead stretches the material at the drawbead area. Because of the history dependent behaviour of the drawbead strain, the material which passes the drawbead at the end of the process obtains more strain than the material which passes the drawbead at the beginning of the process. Therefore, the maximum thickness reduction is found a co-ordinate of distance180 mm.

The deep drawing example is performed with the model for the drawbead strain by stress estimation and by drawbead constraints. Both models give the same results. But, the drawbead model based on a stress estimation converged very slowly. The number of iterations was four to five times higher than the drawbead model by drawbead constraint. So, the model by drawbead constraints is preferred.

5.3 Concluding Remarks

Drawbeads are used to control the material flow locally. They restrict the material of moving to fast and they modify the material properties in a significant manner. An equivalent drawbead has been discussed which incorporates not only the flow restriction but also the material modification. Two strategies have been followed to incorporate the strain changes, the first is based on the drawbead stress estimation and the second is based on the drawbead constraint. The drawbead constraint is recommended because of its better convergence behaviour.

5.4 References

[Beugels, 1993]
Beugels J, *Drawbead simulations*, Graduate report (in Dutch), University of Twente, 1993

[Cao, 1993]
Cao J., M. C. Boyce, *Drawbead penetration as a control element of material flow*, SAE 930517, Sheet-metal and stamping symposium, Detroit, 1993

[Carleer, 1994]
Carleer B. D., P. T. Vreede, P. Drent, M. F. M. Louwes, J. Huétink, *Modelling drawbeads with finite elements and verification*, J. Mat. Proc. Tech., 45/1-5, p 63-68, 1994

[Carleer, 1996]
Carleer B. D., T. Meinders, J. Huétink, *Equivalent drawbead model in finite element simulations*, Numerical simulations of 3-D sheet metal forming processes, Kinzel et al. (eds.), Dearborn, 1996

[Haug, 1991]
Haug E., E. Di Pasquale, A. G. Pickett, D. Ulrich, *Industrial sheet metal forming simulation using explicit finite element methods*, FE-simulation of 3D sheet metal forming process in automotive industry, VDI Berichte 894, 1991

[Huétink, 1986]
Huétink J., *On the simulation of thermo-mechanical forming processes*, PhD-thesis, University of Twente, 1986

[Kawka, 1994]
Kawka M., N. Wang, A. Makinouchi, *Improving drawbeads and friction models in simulations of industrial sheet metal forming processes*, Metal forming simulation in industry, B. Kröplin & E. Luckey (eds.), 1994

[Meinders, 1996]

Meinders T., *Drawbead modelling in 3D deep drawing processes*, Graduate report, University of Twente, 1996

[Taylor, 1993]
Taylor L. M., J. Cao, A. P. Karafillis, M. C. Boyce, *Numerical methods in sheet metal forming*, Numerical simulations of 3-D sheet metal forming processes, Makinouchi et al. (eds.), 1993

[Wouters, 1994]
Wouters P., G. Montfort, J. Defourny, *Numerical simulation and experimental evaluation of the modifications of material properties in a drawbead*, Recent developments in sheet metal forming technology, M. J. M. Barata Marques (eds.), Lisbon, 1994

6. Applications

In this chapter the theory presented in the previous chapters will be applied for the analysis of a number of deep drawing products. The goal of these applications is to show the possibilities of finite element simulations. Every problem can be analysed by different approaches resulting in different results. Depending on the approach the user can obtain results as accurate as he wants to. The applications in this chapter are not the ultimate test but they are an example of how to analyse a deep drawing simulation.
The first application concerns the deep drawing of a square cup. In this example the influence of mesh refinement and the influence of using different element types are studied. The different friction models in combination with varying punch velocities are also examined. The second example is the deep drawing of an S-Rail in which the phenomena of springback and wrinkling are examined. The third application concerns the simulation of the standard Limiting Dome Height test. This test is designed to explore the sensitivity to material behaviour and the prediction of failure. The fourth application concerns the deep drawing of a bracket headlight. In this deep drawing process drawbeads are used to control the material flow. These drawbeads are incorporated with help of the equivalent drawbead. The fifth application is the deep drawing of a mini bonnet out of sandwich laminate. With an adjustment to the existing elements it is possible to describe the behaviour of a sandwich laminate. Three industrial products complete the applications. The cushion seat, the fender and the heat exchanger part show the possibility of analysing industrial applications with the finite element program DIEKA.

6.1 Square Cup

The square cup deep drawing was used as a benchmark problem at the Numisheet ’93 conference [Numisheet, 1993]. The dimensions of the tools are given in Figure 6-1. The blank dimensions, the material properties and the process parameters are listed in Table 6-1. The stress strain curve is fitted with the Nadaï formula, the Nadaï parameters C and n are listed under the material properties.

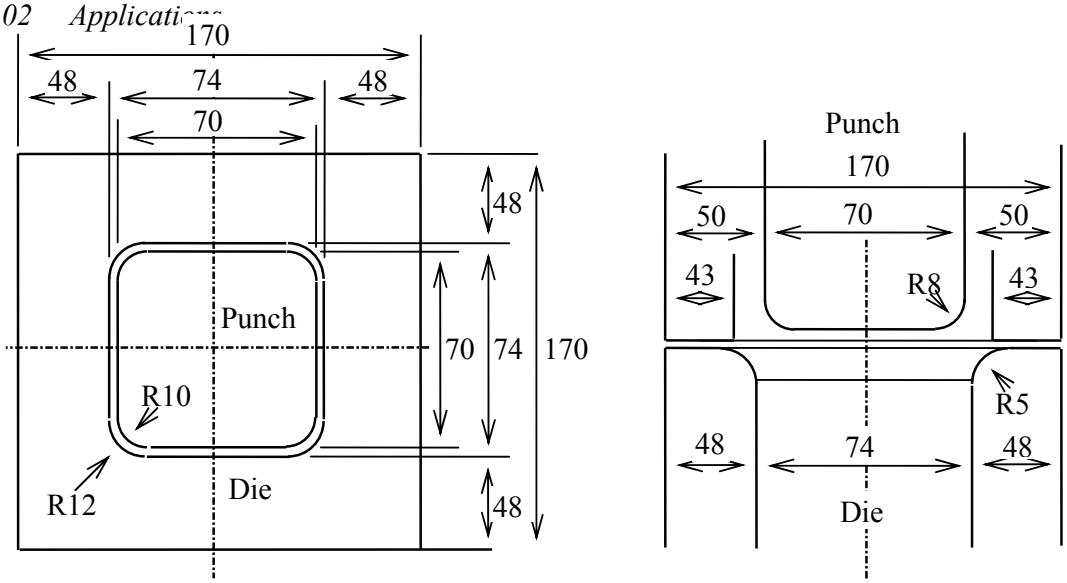

Figure 6-1 *Schematic illustration of the square cup tools*

Blank characteristics		Material properties		Process parameters	
dimension	150x150mm	E	210000 N/mm^2	punch displacement	40 mm
thickness	0.78 mm	ν	0.3	punch speed	1-100 mm/s
		σ_{yield}	173.1 N/mm^2	blankholder force	19.6 kN
		C	565.3 N/mm^2	coefficient of friction	0.144
		n	0.2589		
		R_0, R_{45}, R_{90}	1.79, 1.51, 2.27		

Table 6-1 *Properties for the square cup deep drawing problem.*

Because of the symmetry of this problem only one quarter of the cup was simulated. The material behaviour is described with the Hill yield function. The force displacement curve and the thickness strain along the diagonal of the blank are studied for result evaluation. Firstly, the influence of mesh refinement is studied. Secondly, the element type and last the friction model is studied.

6.1.1 Mesh Refinement

The finite element method is a discrete method, hence the blank has to be divided into a number of elements. The number of elements should not be too small as this can result in an inaccurate solution. The number of elements must not be to large either because of the increasing computational cost.
The square cup is simulated with membrane elements with four different uniform meshes. The mesh characteristics are printed in Table 6-2.

	number of elements	element length [mm]
Mesh 1	338	5.8
Mesh 2	968	3.4
Mesh 3	2178	2.3
Mesh 4	3872	1.7

Table 6-2 *Mesh characteristics for the mesh refinement.*

Figure 6-2 shows the top view of the four deformed meshes. The four meshes are plotted as if they form one product although every mesh is a single simulation. The initial blank size is indicated with the large square. When looking at the four meshes they describe the draw-in almost identical. Small differences in the gradient of the mesh at the line of symmetry occur. The smaller the average element length the better the description of the gradient.

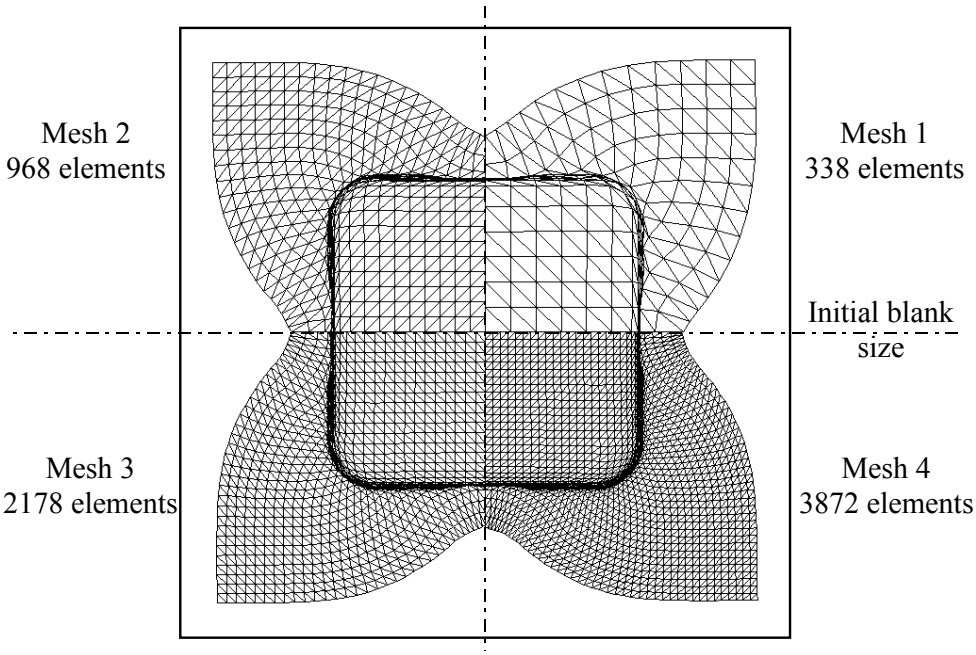

Figure 6-2 *Square cup simulation, deformed product for different numbers of elements.*

The next evaluated item is the force displacement curve of the punch, see Figure 6-3. The punch force for one quarter of the product is printed on the vertical axis. On the horizontal axis, the displacement of the punch is printed. It is clearly that the punch force for mesh 1 shows a lot of scatter and that its value is a little larger than the punch force for the other meshes. The scatter caused by the open-closure behaviour of the contact elements. For the other three meshes, the punch force values are very close to each other.

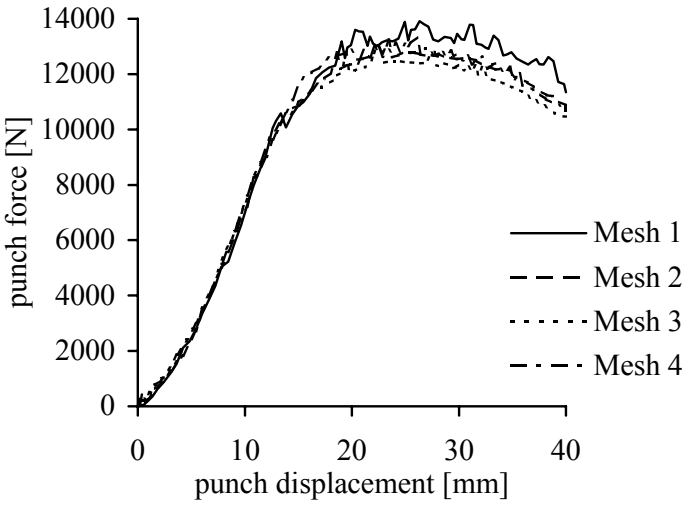

Figure 6-3 *Punch force versus punch displacement for different levels of mesh refinement*

The last item to be evaluated is the thickness strain distribution. Along the diagonal of the square cup the thickness strain is plotted in Figure 6-4 as a function of the original co-ordinate distance. The original co-ordinate distance starts in the centre of the square cup and runs to the edge of the blank.
The thickness strain has a negative peak at the punch corner and a positive peak at the die corner. When comparing the four simulations, mesh 1 again shows a small deviation from the other meshes. Because of the large elements of mesh 1, detailed information is lost.

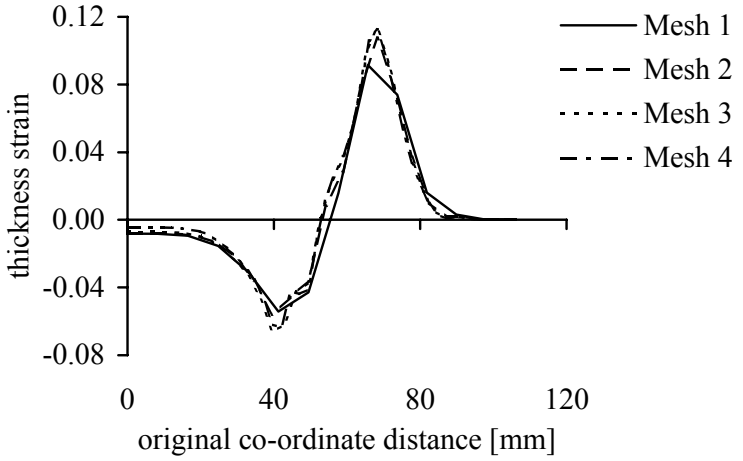

Figure 6-4 *Thickness strain along the diagonal for mesh refinement*

From these results can be concluded that mesh 1 is too coarse. The other meshes do not give many differences in results. So, mesh 2 is the best mesh for this simulation balancing accurate description and computational cost.

6.1.2 Element Type

Different plate deformation theories can be used to describe the sheet behaviour. Based on these theories different element types are implemented in the finite element code DIEKA. The square cup is simulated with mesh 2 from section 6.1.1 with four different element types. These types are the membrane, the DKT1, the DKT3 and the DST element as treated in section 3.5. The plate bending elements are applied with five integration points in thickness direction.
Firstly the force displacement curve will be studied, see Figure 6-5. The membrane elements show the smallest value. The plate bending elements show larger values because of the bending stiffness. The DKT3 and the DST element show identical curves. The curve for the DKT1 element lies between the curves for the membrane element and the DKT3/DST element.

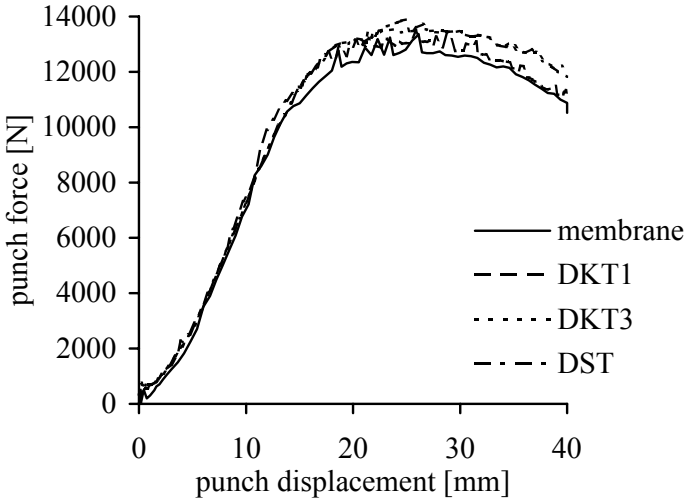

Figure 6-5 *Punch force versus punch displacement for various element types.*

Secondly, the thickness strain distribution along the diagonal is studied, see Figure 6-6. In this figure the average values of the Numisheet experimental benchmark participants are also printed. The experimental in-plane strains are evaluated at the outer side of the product, away from the punch. The thickness strain is obtained from the in-plane strains. So, the results of the simulations are also evaluated at the outer side of the product. This does not affect the results for the membrane element because of the constant strain values in thickness direction.
When looking at the results, the membrane element clearly deviates from the other elements at the punch corner. The neglected bending effects which results in a constant strain in thickness direction are the origin of this deviation. The three plate bending elements show similar strain values and their strain values compare well with the experiments except at the die corner. The height of the sharp peak of the average experimental results is smaller than the peak in the simulations. A reason could be the averaging of the results of the ten experimental benchmark results. The place and the width of the peak compare very well.

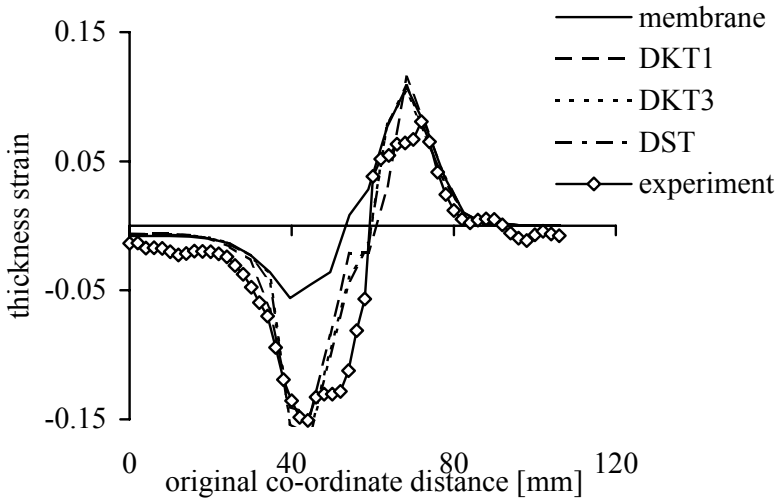

Figure 6-6 *Thickness strain along the diagonal for various element types.*

The DKT3 and the DST element again show identical results where the DKT1 element slightly differs from these two. Already mentioned in section 3.5.3 the DST element degenerates to the DKT3 element for thin plates. A plate is a thin plate if the transverse shear stresses are very small compared to the normal stresses. To verify this, the transverse shear stress in the DST element along the diagonal of the square cup is printed in Figure 6-7.
The shear stress is examined at three places in thickness direction, the inner face, the mid plane and the outer face. The values of these stresses are rather small compared to the value of the other stresses. The in plane stresses are about 400 N/mm^2. So, for this kind of deep drawing products the DKT3 element is preferred to the DST element. When the plate thickness/tool radii-ratio is similar to this problem, the DKT3 element is sufficiently accurate and it is not necessary to use the DST element.

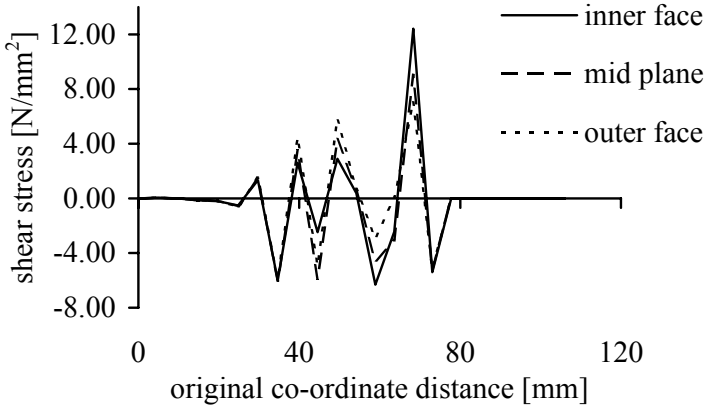

Figure 6-7 *Transverse shear stress along the diagonal for the DST elements.*

6.1.3 Friction Model

In this section the friction model will be examined. The simulations are performed with the DKT3 element with mesh 1. For friction the Coulomb friction model as well as the Stribeck friction model were used. The parameters for the Stribeck friction were obtained from experiments with a material comparable with the material used for the Numisheet '93 benchmark [Haar, 1996]. The Coulomb coefficient of friction is 0.144 and the parameters for the Stribeck friction model are listed in Table 6-3.

η	R_a	μ_{bl}	μ_{hl}	L_{bl}	L_{hl}
0.6 Pa·s	$1.03 \cdot 10^{-6}$ m	0.144	0.010	$2.78 \cdot 10^{-3}$	$5.09 \cdot 10^{-4}$

Table 6-3 *Parameters for the Stribeck friction model.*

Four simulations are performed. One with the Coulomb friction model and three with the Stribeck friction model. In order to study the effect of the Stribeck friction model, three different punch speeds are used, 1 mm/s, 10 mm/s, 100 mm/s. In Figure 6-8 the punch force for a quarter of the square cup for the four simulations are presented. The Coulomb friction model and the Stribeck friction for 1 mm/s give nearly identical punch forces. This means that at a low punch speed all the local contacts operate in the boundary lubrication regime. When the punch speed is increased to 10 mm/s or to 100 mm/s the punch force decreases. Because of the higher velocities larger areas of the surface in contact start to operate in the mixed lubrication regime. This regime shows a decreasing coefficient of friction and therefore the punch force also decreases. The punch force decreases from 13.5 kN for the Coulomb friction to 11.1 kN for the Stribeck friction with a punch speed of 100 mm/s.

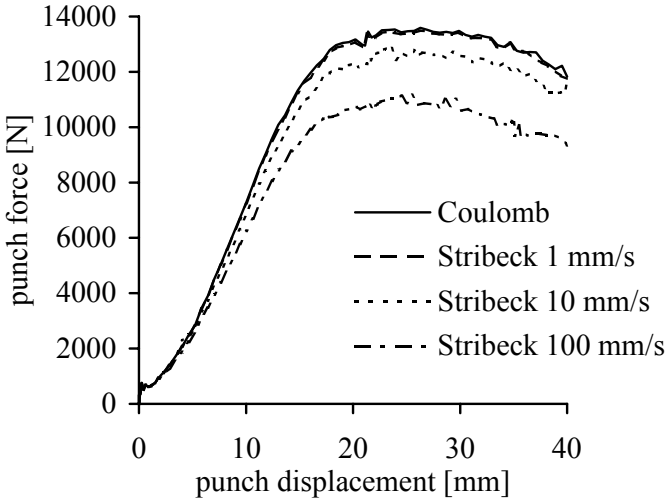

Figure 6-8 *Punch force versus punch displacement for different friction models.*

In Figure 6-9 the thickness strain distribution along the diagonal for the simulations are printed. Again no difference is found for the Coulomb friction compared to the Stribeck friction with a punch speed of 1 mm/s. All simulations give the same results under the punch. In this region the sliding velocity is that low that the blank/punch contact operates in the boundary lubrication regime.
Material initially under the blank holder will have different sliding velocities because of the different punch speeds. A larger sliding velocity means a smaller coefficient of friction. For this reason the material gets less sliding resistance for larger punch

velocities. For the square cup the differences in thickness strain are only very small. The reason is the geometrically dominated deformation. The material flow is strongly defined by the tools and therefore the deformation path of the blank cannot vary a lot.

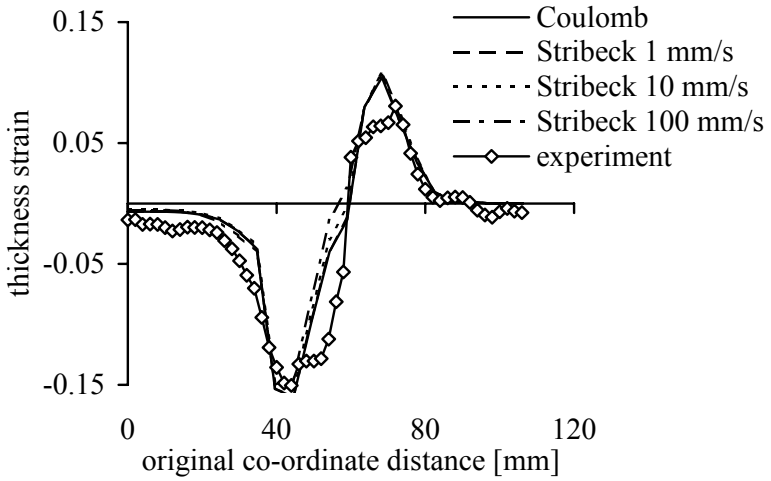

Figure 6-9 *Thickness strain along the diagonal for different friction behaviour.*

6.2 S-Rail

The S-Rail deep drawing problem was a benchmark problem at the Numisheet ’96 conference [Numisheet, 1996]. This benchmark was designed to compare simulations and experiments for shape distortion, wrinkling and springback. The dimensions of the blank are printed in Figure 6-10. The dotted lines in this figure give the major dimensions of the punch and the die. The measures printed in *italics* at the bottom of the blank belong to the punch. The measures printed in *italics* at the top belong to the die, just like the *italics* printed radii. The other punch and die radii are 5 mm.

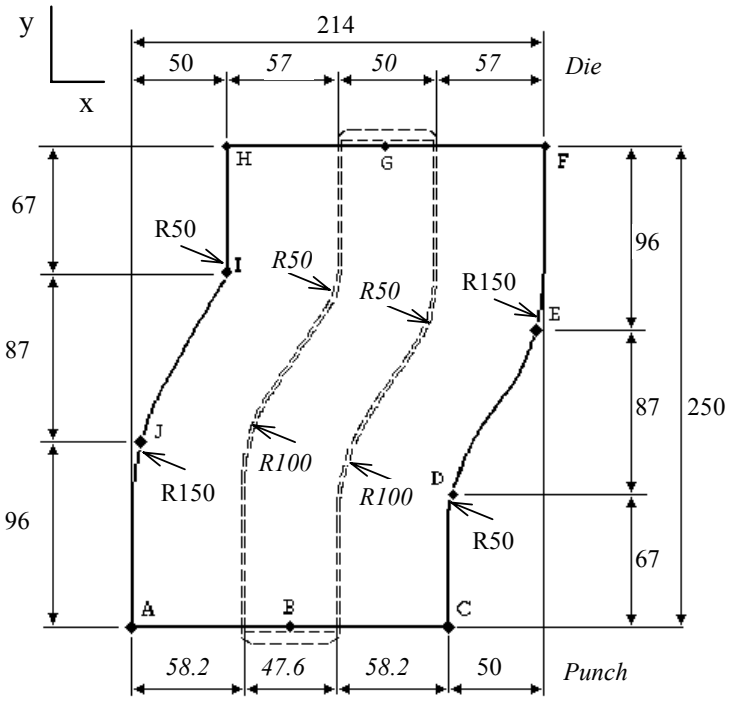

Figure 6-10 *Schematic illustration of the S-Rail blank and the outline of the tools*.

The blank material is a draw quality mild steel with a thickness of 1.0 mm. The rolling direction of the blank is taken along the y-axis. The other material properties and the process parameters are listed in Table 6-4.

Material properties		Process parameters	
E	206000 N/mm^2	punch displacement	37 mm
ν	0.3	blank holder force	10 kN
σ_{yield}	158 N/mm^2	coefficient of friction	0.11
C	520 N/mm^2		
n	0.233		
R_0, R_{45}, R_{90}	1.85, 1.52, 2.37		

Table 6-4 *Properties of the S-Rail deep drawing problem.*

The S-Rail simulation is performed with DKT3 elements and the results are studied in section 6.2.2. Before this simulation can be performed attention will have to be paid to the springback behaviour of the DKT3 element in section 6.2.1.

6.2.1 Springback Analysis

A small strip of the S-Rail is treated to study the springback behaviour. This strip is forced in a plane strain condition. This so called strip model is a powerful tool for preliminary studies of a complete deep drawing simulation [Wiedijk, 1995]. In Figure 6-11 the simulation set-up of the strip model for the springback analysis is shown. A small section of the whole tool set in the strip region is enough for the strip drawing simulation.

Because of the large difference in element size of the tool elements the pinball search algorithm is used for the contact detection. The strip of 164 mm length and 10 mm width is modelled with 120 DKT3 elements.

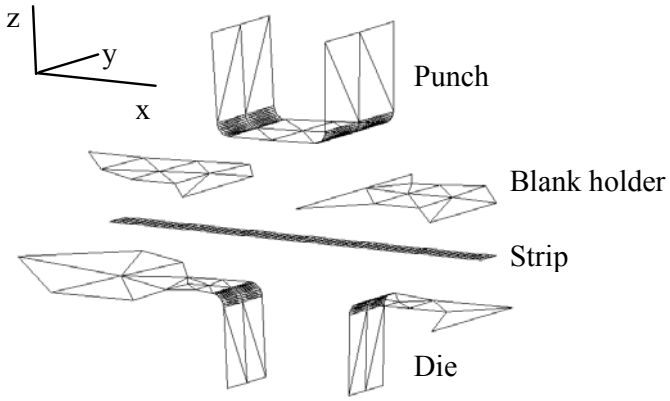

Figure 6-11 *Simulation set-up of the strip model for the springback analysis*.

After the strip is drawn, the tools must be released of the strip to springback. In practice the punch and the blank holder are withdrawn and the product is taken out of the die. In the simulation an other procedure is followed. The tools are fixed at their position and the contact stiffness is relaxed in a few steps to zero. In fact the tools melt away around the strip. This springback analysis is very effective and proved itself to reproduce very well [Atzema, 1994].
Six springback simulations are performed with the number of integration points in the thickness direction varying from two up to seven.

The shape of the strip after drawing and after springback for two and for seven integration points is shown in Figure 6-12 and Figure 6-13 respectively. The shape after drawing is presented by the full line whereas the shape after springback is presented by the dotted line. As can be seen in these figures the number of integration points influences the springback behaviour. The strip with two integration points shows more springback than the strip with seven integration points. In order to be able to look in more detail at the influence of the number of integration points the tangential stresses at the die corner for the six simulations are printed in Figure 6-14.

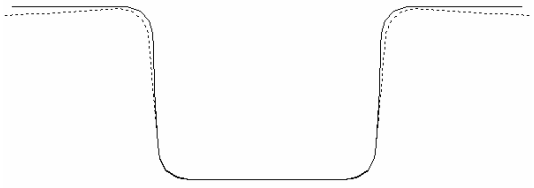

Figure 6-12 *Springback for 2 integration points.*

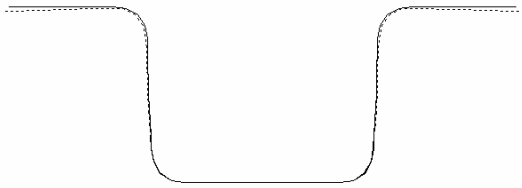

Figure 6-13 *Springback for 7 integration points.*

These six graphs show the tangential stresses in thickness direction at the die radius after drawing and after springback. The full line with the diamond markers represents the stress after deep drawing. The dotted line with the round markers represents the stresses after springback. The x-axis represents the thickness of the strip. The x-value runs through the thickness of the strip from -1 to 0 to 1, which is from the outer face (away from the punch) via the mid-plane to the inner face. The markers in the graph coincide with the position of the integration points.

When looking at the stresses after drawing, the stress distribution represents a superposition of a membrane stress distribution and a bending stress distribution. It is clear that the deformation is in the plastic range, the stress distribution is not linear.
To obtain the stress distribution after springback, the elastic springback stresses are added to the stress distribution after drawing. The stress distribution after springback should be in equilibrium and also the momentum equilibrium should be met. For all the simulations the equilibrium is met within the allowed unbalance.
Comparing the different simulations, the simulations with two and three integration points do not describe the stress distribution very well. The simulations with four up to seven integration points clearly show a similar stress distribution, whereas the simulation with seven integration points should be the closest to the exact stress distribution. But when the computational cost is also taken into account the simulation with four integration points is preferred. This simulation is the best compromise between accuracy of the results and computational cost.

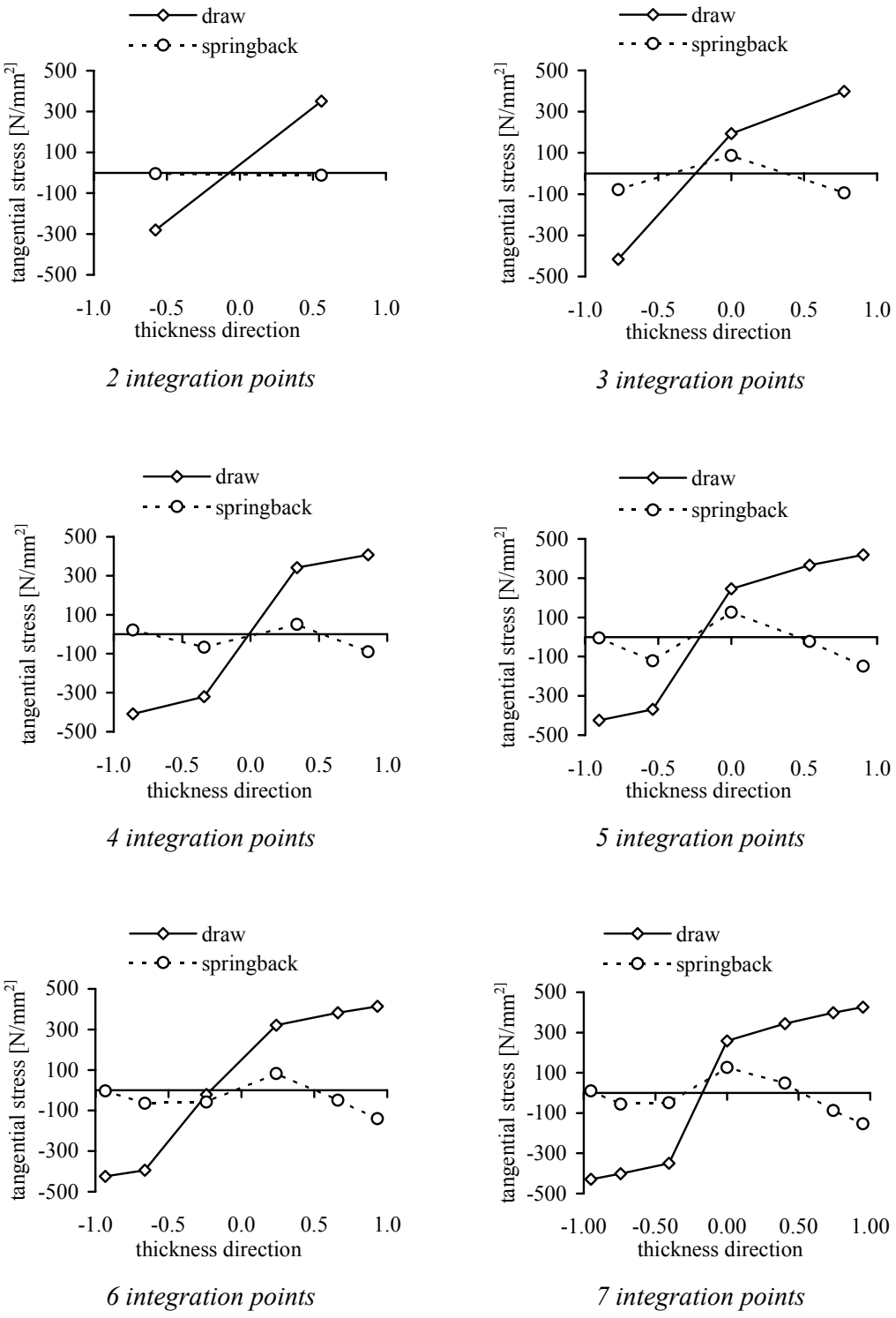

Figure 6-14 *Tangential stress distribution in thickness direction for different number of integration points.*

6.2.2 S-Rail Simulation

The deep drawing of the S-Rail is performed with DKT3 elements with four integration points in thickness direction. The blank is meshed with 6000 elements. An overview of the simulation set-up is shown in Figure 6-15.
The pinball search algorithm is used for contact detection. In combination with a three level block search the contact detection works very effective and efficient. The deep drawing process is simulated in 130 steps, while the springback process takes another 10 steps.

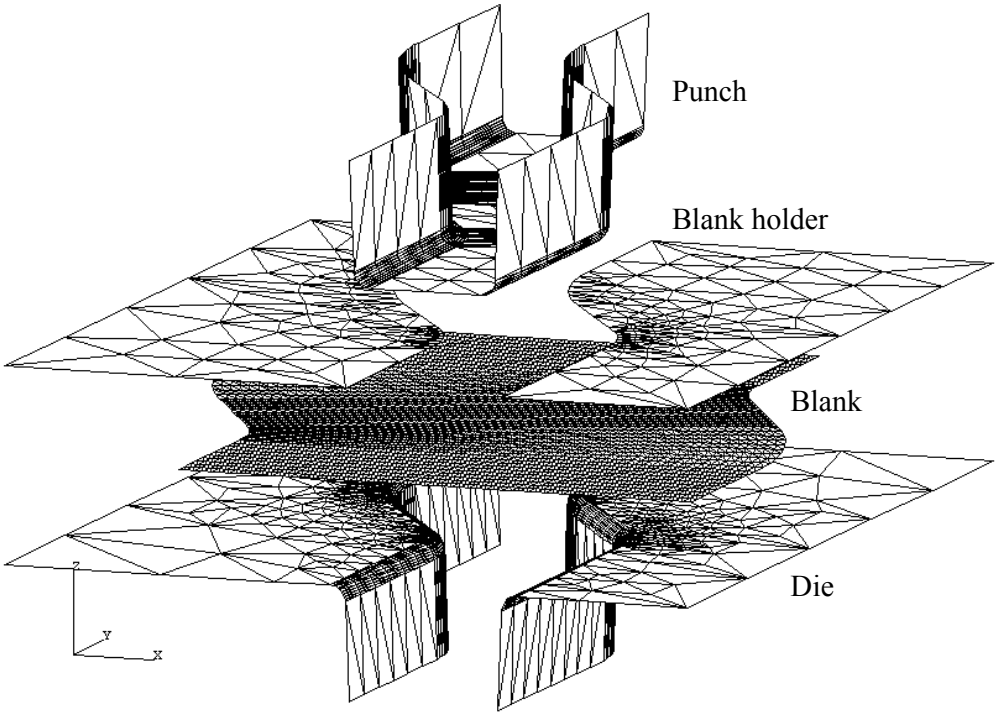

Figure 6-15 *Overview of the simulation set-up for the S-Rail.*

Figure 6-16 shows the thickness distribution of the S-Rail after springback. The initial thickness of 1.00 mm is in the green range. Thickening of the material is represented up to the red range. Thinning of the material is represented down to the blue range. This figure gives a good impression of the overall thickness distribution. For a more detailed look, some results will be presented in x-y graphs.

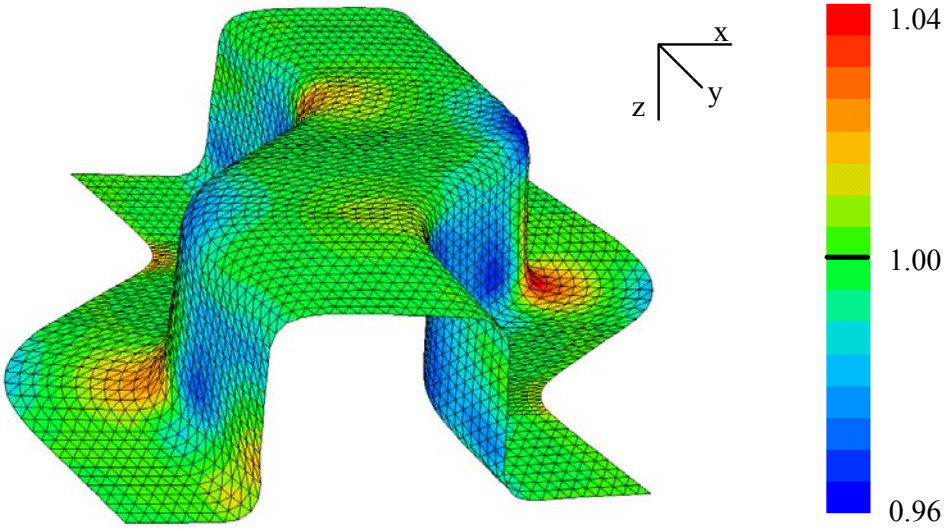

Figure 6-16 *Thickness distribution of the S-Rail after springback.*

Firstly, the major and the minor strains along the line JD will be presented, see Figure 6-17 and Figure 6-18 respectively. The definition of the line JD can be found in Figure 6-10. For comparison the average experimental results from the Numisheet experimental benchmark participants are also presented in these graphs. The strains are evaluated at the outer side of the product away from the punch.

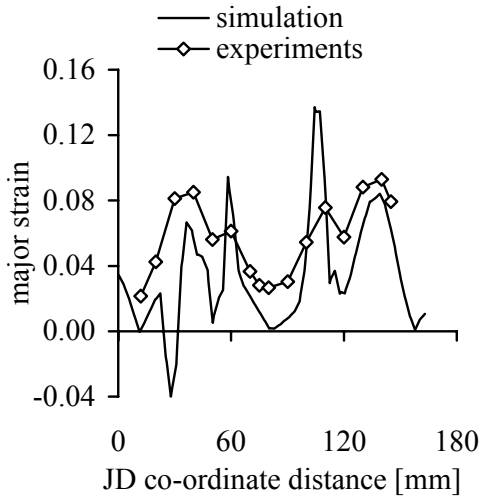

Figure 6-17 *Major strain along JD after spring back.*

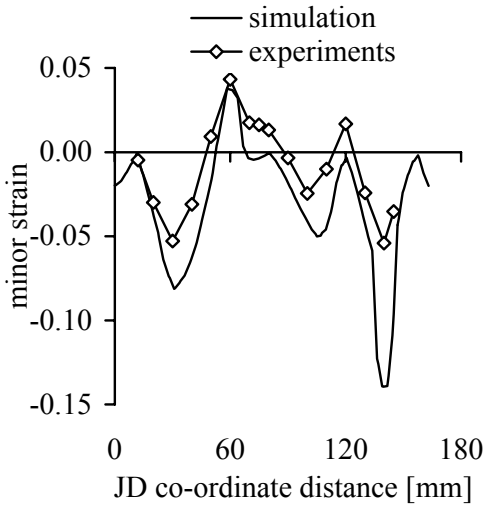

Figure 6-18 *Minor strain along JD after spring back.*

Looking at the major strain distribution in Figure 6-17, four peaks in positive direction can be seen. The peaks represent the bending around the die and the punch corner. The four peaks are seen in both the simulation and the experiments. They compare very well concerning the position and fairly well concerning the values. At co-ordinate distance 30

mm, which is near the die corner, the simulation shows a negative peak. This negative peak is a result of the strain extrapolation from the integration points to the outer side. At this position a large gradient in thickness direction can be seen.
The minor strain distribution in Figure 6-18 also compares very well for the simulation and the experiments.

At the bottom of the S-Rail some shape distortion and wrinkling can be detected. In order to show these phenomena, the z-co-ordinate along the line BG across the bottom of the product is printed in Figure 6-19. The definition of the line BG can be found in Figure 6-10. Again the simulation and the experiments can be compared. When looking at the evolution of the shape, both graphs look similar . The ups and downs of the curves compare very well concerning place and size.
This makes the finite element simulations a powerful tool to detect this kind of shape distortions even before the product is produced. The process parameters and the tool design can be modified in the model input to examine their influence on the shape distortion. When the right characteristics are found the tools can be produced and a neat product can be obtained without an expensive experimental trial and error process.

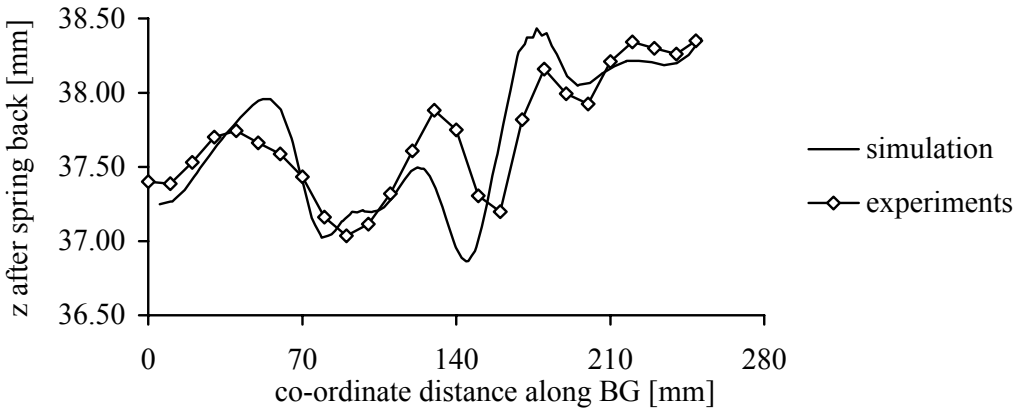

Figure 6-19 *Z-co-ordinate after spring back along BG.*

6.3 Limiting Dome Height

The Limiting Dome Height (LDH) was also used as a benchmark problem at the Numisheet ’96 [Numisheet, 1996]. The LDH benchmark was designed to compare simulations and experiments for the prediction of failure and for the sensitivity of material behaviour. The dimensions of the tools cross section at the line of symmetry are given in Figure 6-20 and the dimensions of the lockbead are given in Figure 6-21. The die and the lockbead are also round just like the punch.

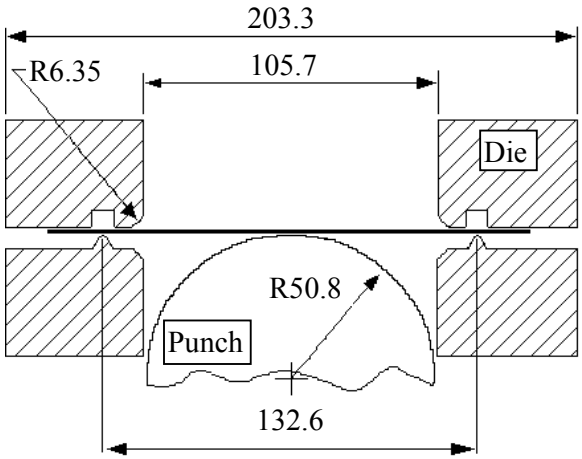

Figure 6-20 *Schematic illustration of the LDH tools*

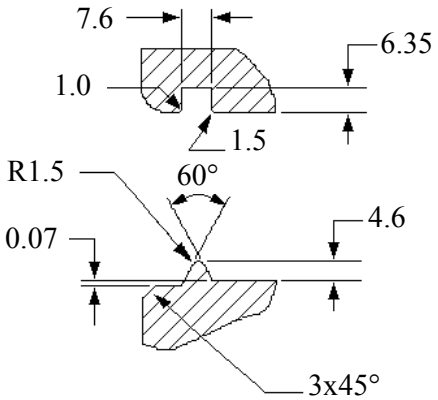

Figure 6-21 *Schematic illustration of the lockbead.*

The dimension of the blank is 180 x 100 mm with the rolling direction along the long side. The test is performed with the draw quality mild steel identical to the material for the S-Rail. The blank holder force must be that large that the draw-in at the centre line does not exceed 0.25 mm at a punch height of 30 mm.
A closer look at the lockbead is given in section 6.3.1. In section 6.3.2 the LDH simulation is examined.

6.3.1 Lockbead Analysis

The lockbead can be treated like a drawbead. Therefore a 2D plane strain analysis, which has been developed for drawbeads has been performed, The deformed mesh of the lockbead is shown in Figure 6-22. The strip is pulled to the left. The projected contact elements are also shown and they given an indication of the lockbead geometry.

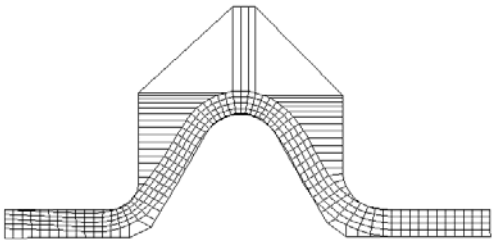

Figure 6-22 *Mesh for the lockbead analysis.*

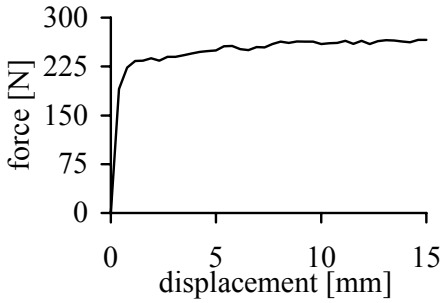

Figure 6-23 *Lockbead pulling force.*

The main result of this simulation is the force to pull the strip through the lockbead, see Figure 6-23. The pulling force increases very fast and after a small displacement the force

is already 240 N. The force slightly increases while pulling the strip further. It is not necessary to pull the strip that far because the bead should lock the material. A steady state value of 260 N is assumed for the lockbead force.
The strain changes are of minor importance because the material will not be pulled that far through the lockbead.

6.3.2 LDH Simulation

For the LDH simulation only a quarter of the product is analysed because of symmetry. The quarter blank is shown in Figure 6-24. The x-axis and the y-axis are the axis of symmetry. The blank is meshed till the lockbead which is indicated at the right side. The lockbead is incorporated by an equivalent drawbead. The equivalent drawbead works on the edge nodes at the right side of the blank. The top of the blank is a free edge. The blank is modelled with 3000 DST elements. The tools are modelled with standard shapes. The process is simulated in 200 steps.

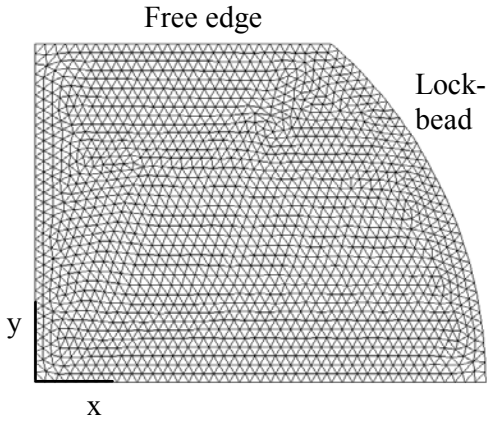

Figure 6-24 *Original mesh with the position of the lockbead.*

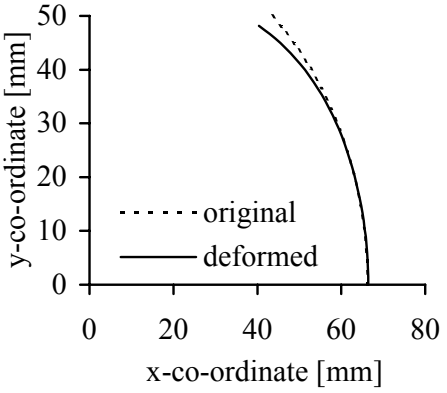

Figure 6-25 *Draw-in at the lockbead.*

Three simulations are performed, every simulation uses a different material behaviour. The first simulation uses an planar isotropic Hill yield function. The second simulations uses an planar anisotropic Hill yield function whereas the third simulation uses a Vegter yield function. The stress strain curve is fitted with the Nadaï formula. The parameters for this formula are identical to the parameters used in the S-Rail simulation.
The other parameters for the three material descriptions are listed in Table 6-5. The material properties for the Hill material description are the material definitions of the Numisheet ’96. The material properties for the Vegter material description are obtained from experiments at Hoogovens Research & Development and can also be found in [Numisheet, 1996].
The reference points for the Vegter yield function are normalised with the yield stress. Because of the missing of experimental data for the pure shear point, this value is an estimated one. It is clearly that for the Vegter yield function much more parameters are necessary. So, to use this function an extensive experimental program must be performed.

Material properties	E	ν	σ_{yield}	C	n
	206000 N/mm^2	0.3	158 N/mm^2	520	0.233

Hill isotropic		Hill anisotropic		Vegter :	0°	45°	90°
$R_{average}$	1.82	R_0	1.85	pure shear	0.545	0.545	0.545
		R_{45}	1.52	uni-axial	0.993	1.009	0.991
		R_{90}	2.37	plane strain	1.233	1.228	1.262
				equi-biaxial	1.190	1.190	1.190
				R	2.07	1.86	2.63

Table 6-5 *Material properties for the LDH simulation.*

A first interesting point is the draw-in at the lock bead. The co-ordiante of the lockbead edge of the original blank and of the deformed blank are printed in Figure 6-25. The dotted line represents the original position of the lockbead edge and the full line represents the position of the points which originally started in the lockbead. All three simulations show an identical draw-in, so only one deformed edge is printed.
As can be seen, the lockbead not fully locks the material. At the axis of symmetry the material is locked whereas at the free edge the material draw-in is about 4.5 mm. A draw-in at the free edge was also found in the experiments. So, the approximation of the lockbead with the equivalent drawbead is better than completely lock the lockbead edge.

The major and minor strains along the x-axis are presented in Figure 6-26 and Figure 6-27 respectively. The average results of the Numisheet experimental benchmark participants are also presented in these graphs. The strains are evaluated at the outer side of the product away from the punch.

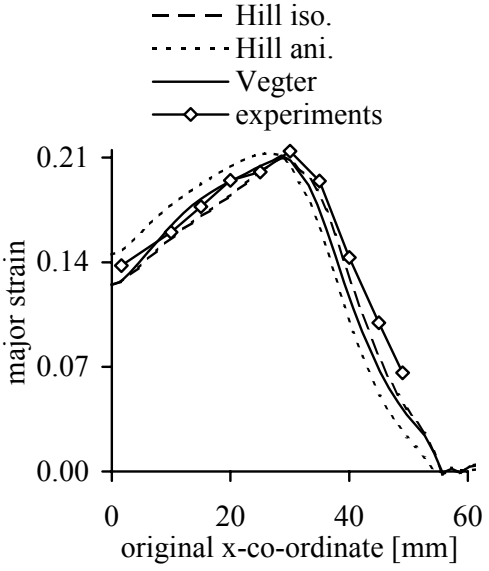

Figure 6-26 *Major strain along the x-axis.*

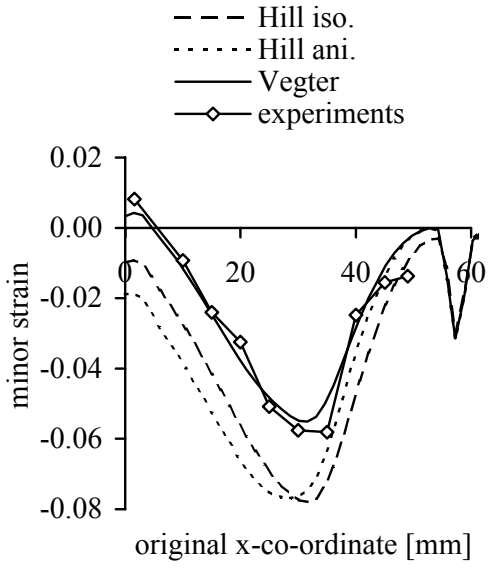

Figure 6-27 *Minor strain along the x-axis.*

Looking at the major strain, the maximum value is found at a x-co-ordinate of 30 mm. For larger x-co-ordinates the three simulations show a smaller value than the experiments. For smaller x-co-ordinates the planar isotropic Hill description shows smaller strain values whereas the planar anisotropic Hill description shows larger values. The Vegter description lies between the two simulations with the Hill description and compares very well with the experiments.
Looking at the minor strain, the Vegter description again compares very well with the experiments. The two simulations with the Hill description show more strain and clearly deviate from the experiments.
The deformations on the x-axis lie between the uni-axial point and the plane strain point. The position of the plane strain point is of importance to describe the deformations on the x-axis. The Vegter yield function is constructed by using among others the plane strain point whereas the Hill yield function only uses the uni-axial point. This is the strength of the Vegter yield function and the reason that this yield function gives a better description of the strains. The extensive experimental program is worth while when an accurate description of the material behaviour is needed.

The forming limit diagram (FLD) of this mild steel is used to predict failure. In an FLD two areas can be distinguished. The forming limit curve (FLC) divides the strain space into a safe part and a failure part. The strain combinations below the FLC are in the safe part and above the FLC are in the failure part.
The Figure 6-28 shows the FLD for the draw quality mild steel. In this figure also the strains of the LDH simulation with the Vegter material at a punch height of 40.05 mm are shown. It is clear that most strain combinations are in the safe zone but a few strain combinations just pass the line of the FLD. So, the material fails at a punch height of 40.05 mm. The failure zone is at the line of symmetry, at the x-axis.
The average value of the Numisheet experimental benchmark participants was 40.1 mm. So, the simulation predicts the punch height at failure very well. It should be mentioned that the spread in the experimental results was rather large. The minimum value was 30.0 mm whereas the maximum value was 46.0 mm.

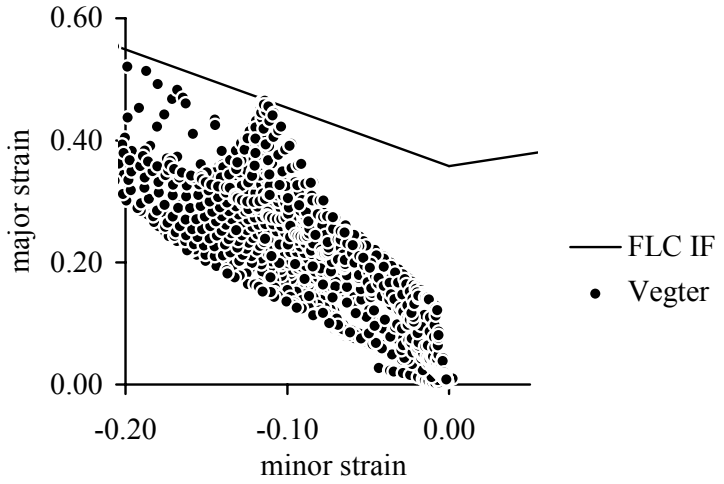

Figure 6-28 *Forming limit diagram for the LDH at a punch height of 40.05 mm.*

6.4 Bracket Headlight

The deep drawing of the bracket headlight has already been simulated by Vreede [Vreede, 1992]. One of the recommendations in this work was to incorporate drawbeads in the simulation. Since the equivalent drawbead is now available in DIEKA this deep drawing simulation is repeated.

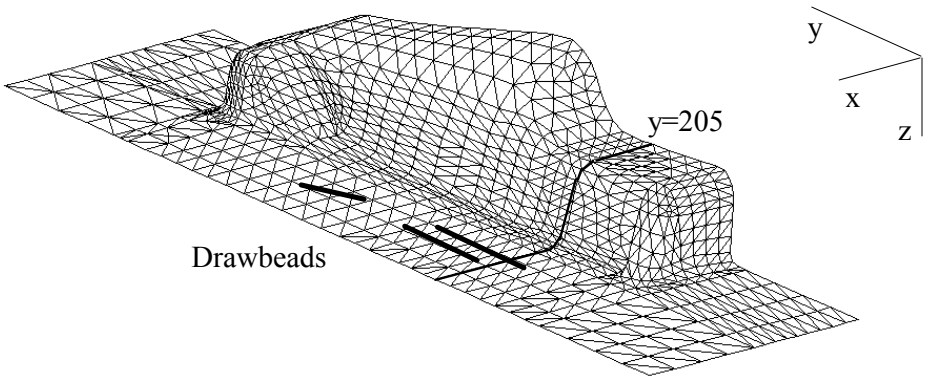

Figure 6-29 *Die for the bracket headlight simulation.*

Figure 6-29 shows the definition of the die. In contrast to Vreede, who used a collection of points, the tools are defined by elements. In the figure the position of the drawbeads is indicated by the three fat lines. The blank is modelled with 7200 membrane elements. Three different simulations are performed. The first simulation neglects the drawbeads. The second simulation applies the equivalent drawbead with only the restraining force. The third simulation applies the equivalent drawbead with both the restraining force and the strain changes.

The thickness distribution of the bracket headlight simulation with the equivalent drawbead with both the restraining force and the strain changes is shown in Figure 6-30. The initial blank thickness of 1.48 mm is in the green region. The material thickens up to 1.65 mm in the red region and becomes thinner down to 1.15 mm in the blue region. The appearance of the drawbead at the long flange influences the thickness distribution. A thinning of the material can be distinguished at the position of the drawbeads.

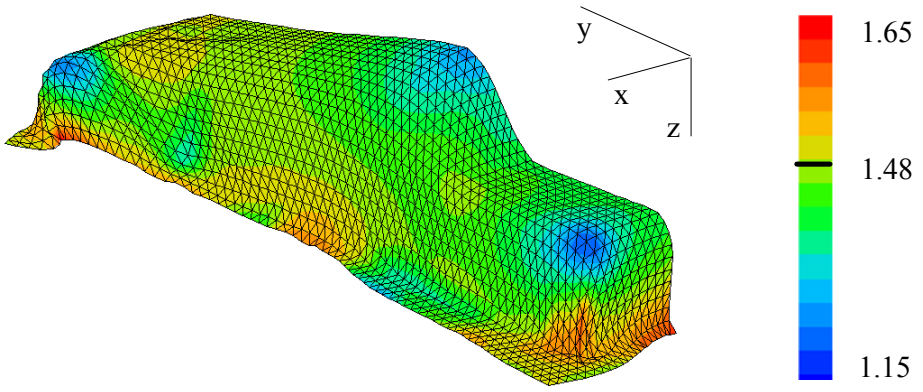

Figure 6-30 *Thickness distribution of the simulation of the bracket headlight.*

In order to take a closer look at the thickness distribution, the cross section y=205 mm is examined. The cross section is indicated in Figure 6-29. In Figure 6-31 the thickness distribution for the simulations and the experiment is plotted. Along the x-axis the co-ordinate distance of the deformed part is printed. The co-ordinate distance starts at the line of symmetry and runs till the flange of the product. In the left side of the graph the values are rather close to each other. In the right side, large differences appear. The experiment shows a large thickness reduction. This is caused by the drawbeads. The simulation with the equivalent drawbead with force and strain also shows a small drop in thickness. The simulation with the equivalent drawbead with only force does not show this effect. The simulation without drawbeads overestimates the thickness considerably.
The simulations can be improved while they are being performed with the DKT3 or DST element because these elements do not neglect the bending effects around the die corner. However, the equivalent drawbead is under development for these element types and hence not available yet.

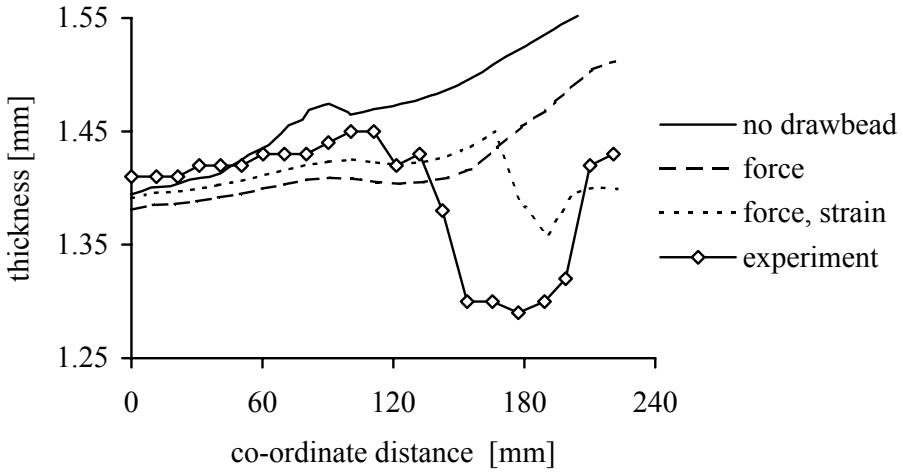

Figure 6-31 *Thickness along cross section y=205 mm for the bracket headlight.*

The drawbeads also influence the material flow. The flange shape of the simulations and the experiment is examined to study this influence, see Figure 6-32. The simulation

without drawbead clearly overestimates the draw-in at the long flange. But even at the short flange, at y-co-ordinate around 50 mm, the draw-in differs from the experiment.
The two simulations with the drawbeads are quite good at the short flange in comparison to the experiment. At the long flange these simulations predict the draw-in better than the simulation without drawbead. The simulation with the equivalent drawbead with force and strain is a little closer to the experiment than the simulation with the equivalent drawbead with only force. Although, there still is a deviation from the experiment. Again a simulation with DKT3 or DST elements is recommended to improve the draw-in prediction.

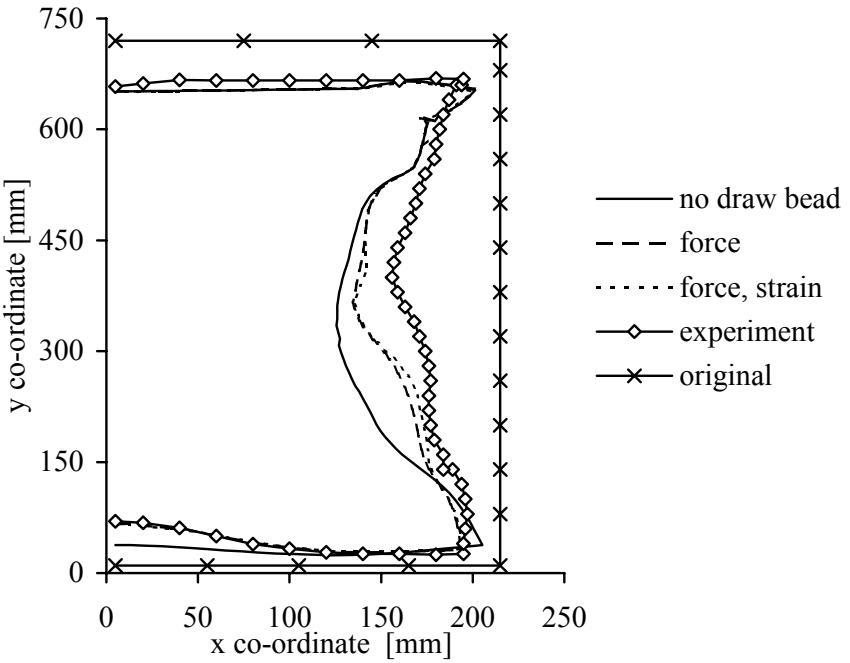

Figure 6-32 *Flange shape of the bracket headlight.*

6.5 Mini Bonnet

The mini bonnet is a try-out part for the deep drawing of sandwich laminates. In this product the characteristics of a real bonnet are incorporated. This part has the code name VD II. Figure 6-33 shows the tools for the VD II; because of symmetry it is sufficient to analyse half of the product. The blank for the product is a rectangle sandwich laminate of 800 x 600 mm. The sandwich laminate consists of a polymer core of 0.85 mm thickness with an aluminium skin with a thickness of 0.20 mm on both sides. The material properties of the sandwich laminate are listed in Table 6-6. In section 6.5.1 a short explanation of the sandwich element will be given. The simulation of the VD II is discussed in section 6.5.2.

	Aluminium skins	Polymer core
E	70.0 GPa	2.0 GPa

σ_{yield}	120 MPa	28.0 MPa
C	590.0 MPa	1.0 MPa
n	0.33	0.50
R	0.7	1.0

Table 6-6 *Material properties of the sandwich laminate.*

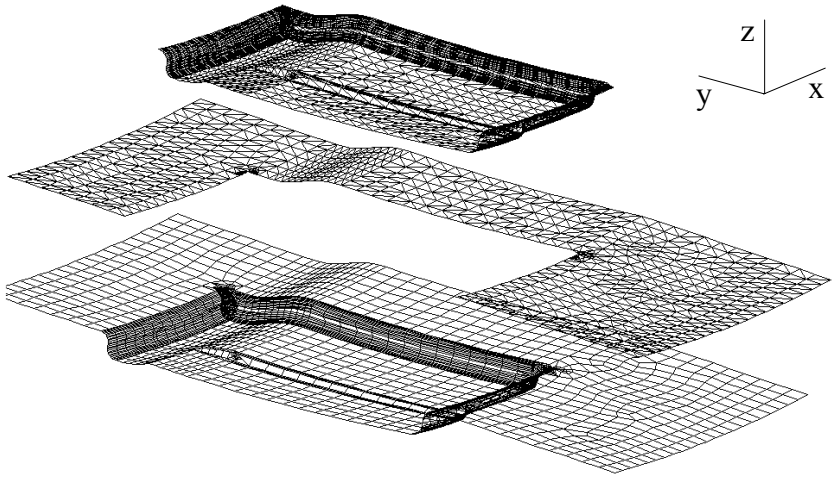

Figure 6-33 *Tool set-up for the VD II analysis.*

6.5.1 Sandwich Element

In the development of the sandwich element, a few assumptions have been made:
- The model is restricted to sandwich laminates with thin skins compared to the core.
- Perfect bonding between the skins and the core is assumed.
- No temperature effects will be treated, so only cold forming processes can be analysed.

The next step is to find out the important phenomena during the forming of the sandwich laminate. For this reason a 2D study of bending and deep drawing was performed. From this study the following conclusions can be drawn [Pape, 1995-1]:

the membrane stresses of the skin	>>	the membrane stresses of the core
the membrane stresses of the skin	>>	the bending stresses of the skin
the membrane stresses of the skin	>>	the shear stresses of the skin
the membrane stresses of the core	>>	the bending stresses of the core
the membrane stresses of the core	≈	the shear stresses of the core

With these results and balancing complexity and effectiveness, a sandwich element has been developed. This sandwich element evaluates the membrane stresses in the skins and the membrane and shear stresses in the core. Because of the perfect bonding assumption it is possible to reduce the number of external degree's of freedom. For a three node element 18 degrees of freedom are sufficient; three displacements and three rotations per node.

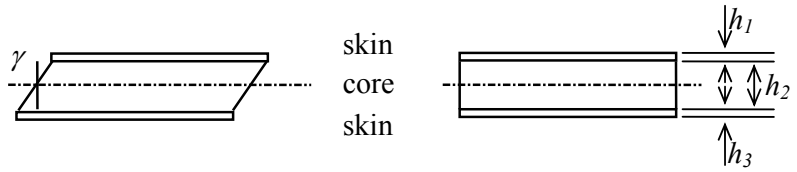

Figure 6-34 *Schematic outline of the sandwich element.*

The membrane stress in the skin are evaluated on half the thickness of the skin. So, for layer one on ½(h_1+h_2) and for layer three on -½(h_2+h_3), see Figure 6-34. Because the membrane stress is evaluated out of the neutral plane, the element shows bending resistance. The shear stress varies linearly over the thickness according to the Mindlin theory. In order to avoid shear locking the shear stresses are reduced integrated.
This element efficiently describes the deformation behaviour of a sandwich element while its complexity is limited. This element can be seen as a special edition of the DST element with three integration points in thickness direction. The element proved to describe the deep drawing of an axi-symmetric product and of a square cup very well [Pape, 1995-1]. In the next section the deep drawing of the VD II will be treated.

6.5.2 Mini Bonnet Simulation

The blank is modelled with 4734 sandwich elements with mesh refinements at the places of the local radii of the tools. Because of the curved die face a pre-formed blank is used [Pape, 1995-2]. The calculated total thickness distribution for the VD II is shown in Figure 6-35. The initial thickness of 1.25 mm is in the yellow range. The thickness changes occur at a limited number of areas. These areas are the corners of the product and the edge in the middle of the product. However, when no thickness changes are found, it does not mean that no deformation occurs.

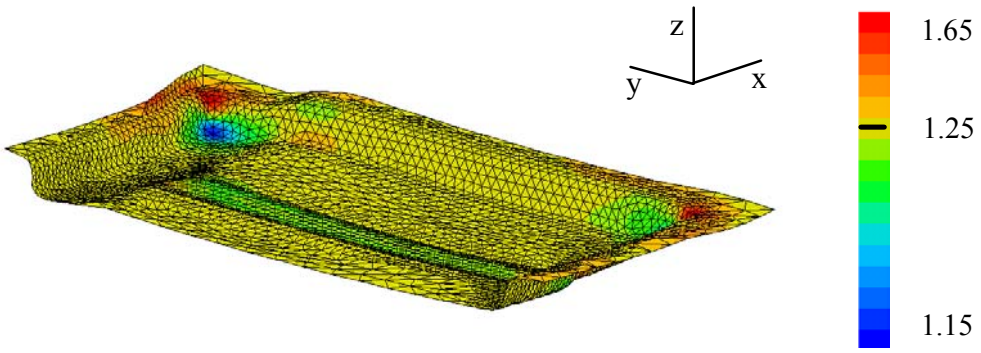

Figure 6-35 *Total thickness distribution for the VD II.*

An advantage of finite element simulations is the possibility of analysing results in the material and not only at the surface. Properties of the core can be analysed which is very difficult in experiments. In Figure 6-36 the shear strain in the core for the VD II along a cross section parallel to the x-axis halfway the product is printed. In this figure the z-co-

ordinate of the cross section of the product is also depicted. The co-ordinate distance along the x-axis starts at the line of symmetry. At the S-curves in the product, at the co-ordinate distance of 120 mm and 340 mm, the shear stresses are not equal to zero. When running across the cross section from the left to the right, the shear stress shows a positive peak followed by a negative peak. The core shears in alternating direction to reduce the membrane strains in the skins. This makes the sandwich laminate a suitable material for products with this kind of deformations.

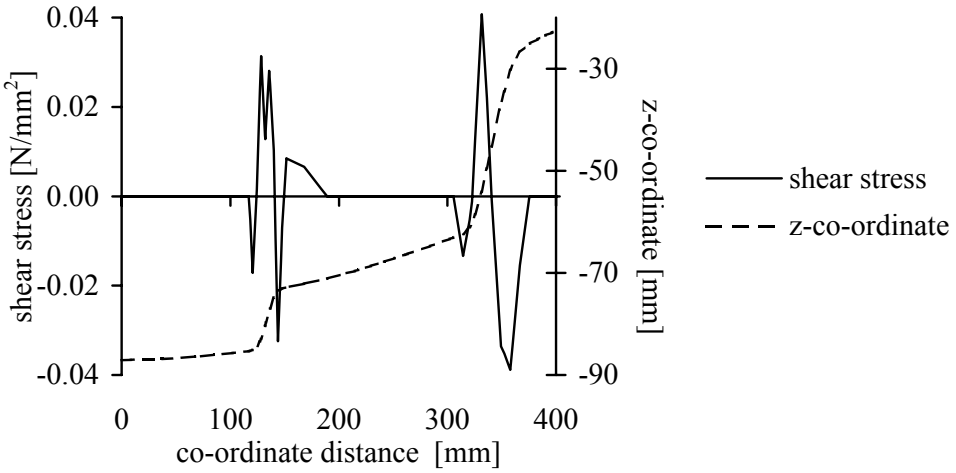

Figure 6-36 *Shear strain in the core of the VDII along a cross section.*

6.6 Spin-off

In this section three examples of industrial applications are shown. The examples are analysed with the finite element code DIEKA at Hoogovens R&D. The first example is a part of a cushion seat, the second example is a fender and the third example is a heat exchanger part. The previous sections showed extended analyses of the deep drawing applications whereas in this section the deep drawing applications are only briefly reviewed.
An extensive validation program at Hoogovens R&D has been carried out. The tendency is a very acceptable agreement of simulation results and experimental data.

The material data for the simulations are obtained from tensile tests and the friction data are based on the actual measured values for the used mean punch velocity and contact pressure [Langerak, 1996].
The simulations were performed on small scale workstations. The actual simulations took several hours with a maximum of sixteen hours, which means that all the simulations could be done over night. The preparation for the simulations took much more time. Depending on the problem this time varied from several days to several weeks. Most of the work was devoted to the preparation of the tool description. The tool description must not be to coarse in order to give a proper description of the tools. The tool corners and the

details of the tools have to be accurately described. But some small details are not meshed because they are not important and therefore they are only a ballast for the forming simulation. This means that still a lot of handwork needs to be done.
The tools description exists of a large number of elements in order to describe the parts, 60000 elements is no exception. Because of this large number of elements of the tool descriptions, the block search algorithm is used for the contact search. The application of the block search considerably speeded up the computation.

6.6.1 Cushion Seat

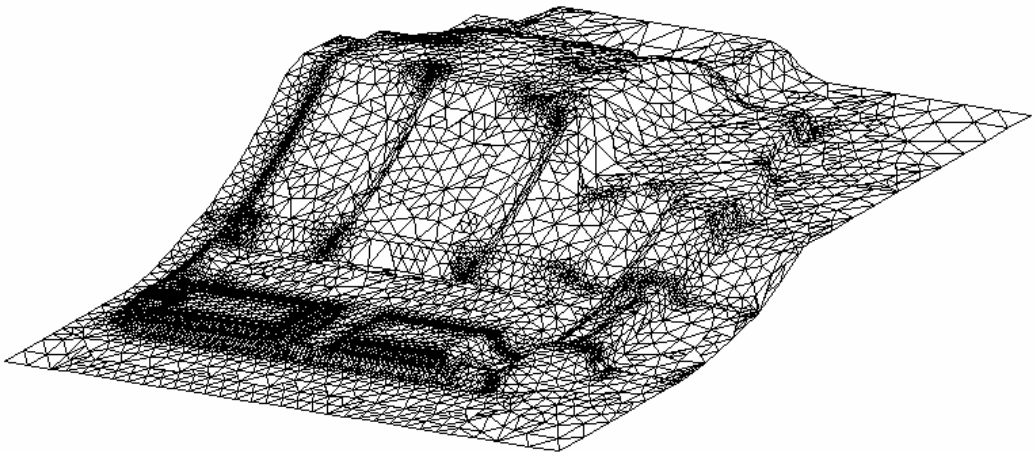

Figure 6-37 *Die for the cushion seat simulation.*

Figure 6-37 shows the definition of the die for the cushion seat. The tool description was achieved by CAD data using an IGES interface. The blank was modelled with 9514 elements. In the bottom left corner of the blank a mesh refinement was applied, see Figure 6-38. This area of the part was a critical zone. This figure shows the thickness strain distribution of the simulation of the cushion seat.

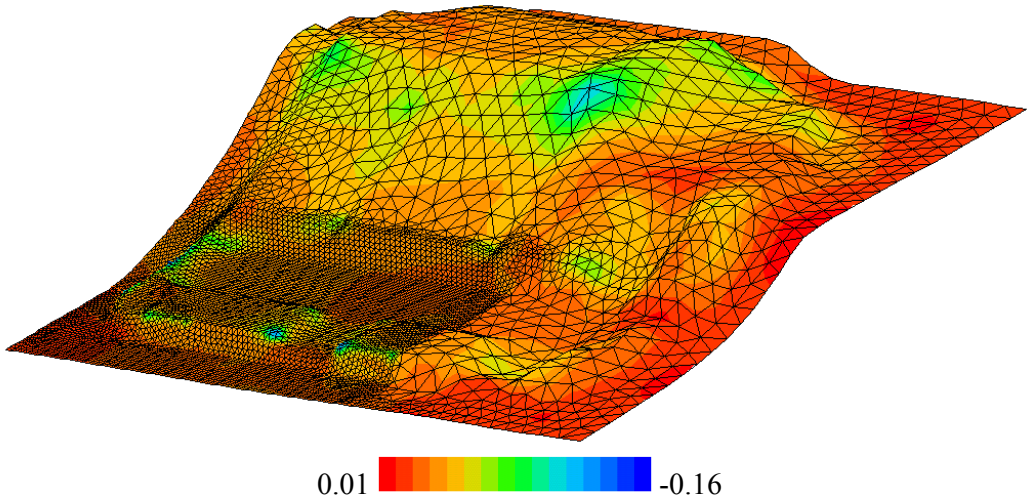

Figure 6-38 *Thickness strain distribution of the simulation of the cushion seat.*

6.6.2 Fender

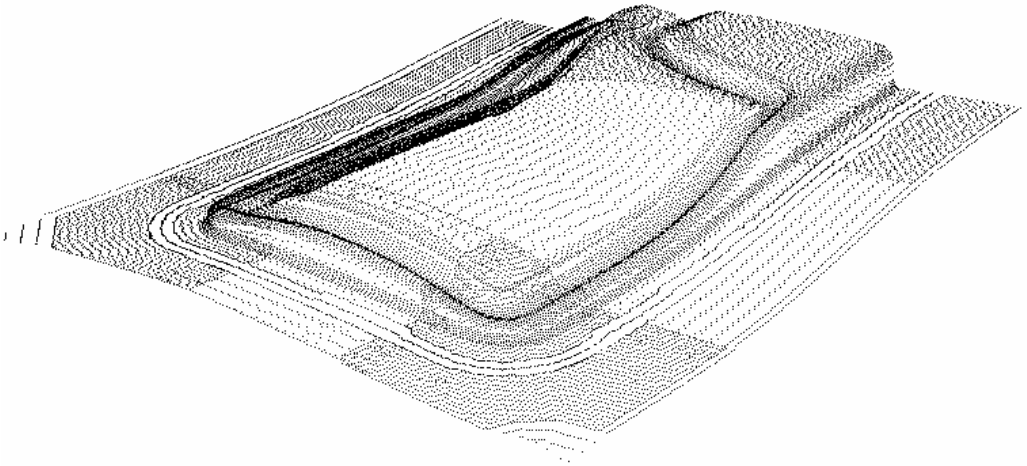

Figure 6-39 *Collection of points of the die for the fender simulation.*

The tool description of this part was achieved by a collection of points obtained from a tool measurement. The collection of points of the die is shown in Figure 6-39. The collection of points is meshed to obtain a neat tool definition for the finite element simulation.
The original blank is a rectangle of 1038 x 908 mm and it is meshed with an isoparametric mesh of 11016 elements. Figure 6-40 shows the deformed mesh with the major strain distribution of the fender. The strain distribution is relatively smooth with some peaks, the red and yellow zones in the figure.

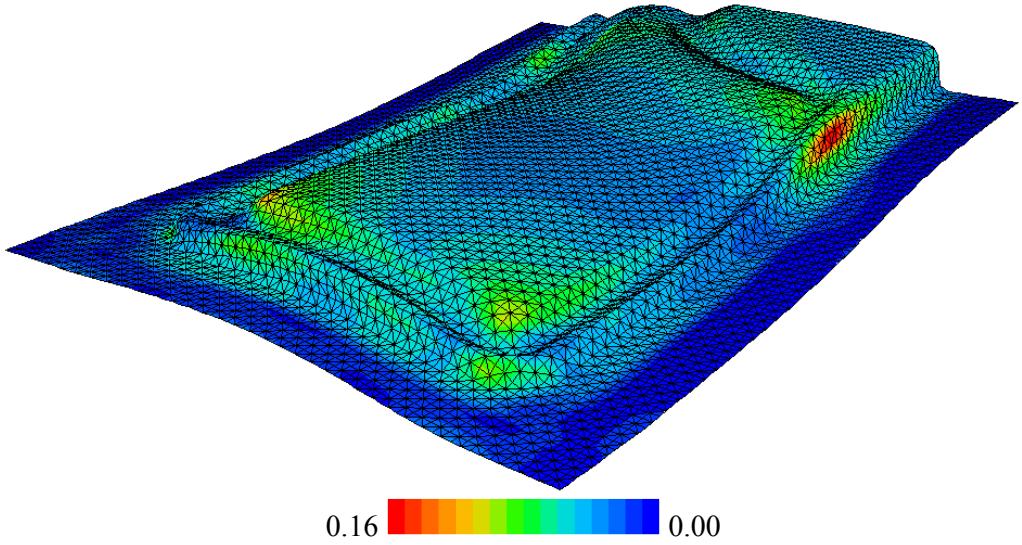

Figure 6-40 *Major strain distribution of the simulation of the fender.*

6.6.3 Heat Exchanger

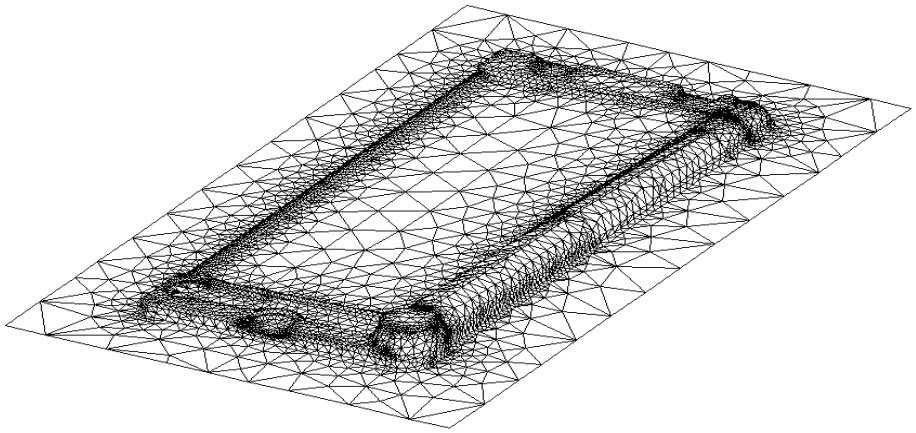

Figure 6-41 *Die for the heat exchanger part.*

Figure 6-41 shows the definition of the die for the heat exchanger part. The tool description was obtained from a collection of points which was meshed. The deformation of the part is concentrated at the deepest corner of the product.
The blank is meshed with 3965 elements with a mesh refinement at the deepest corner. Figure 6-42 shows the equivalent plastic strain of a detail at the deepest corner of the deformed mesh of the heat exchanger part. The deformations at this zone are rather critical whereas the deformations in the rest of the part are very small.

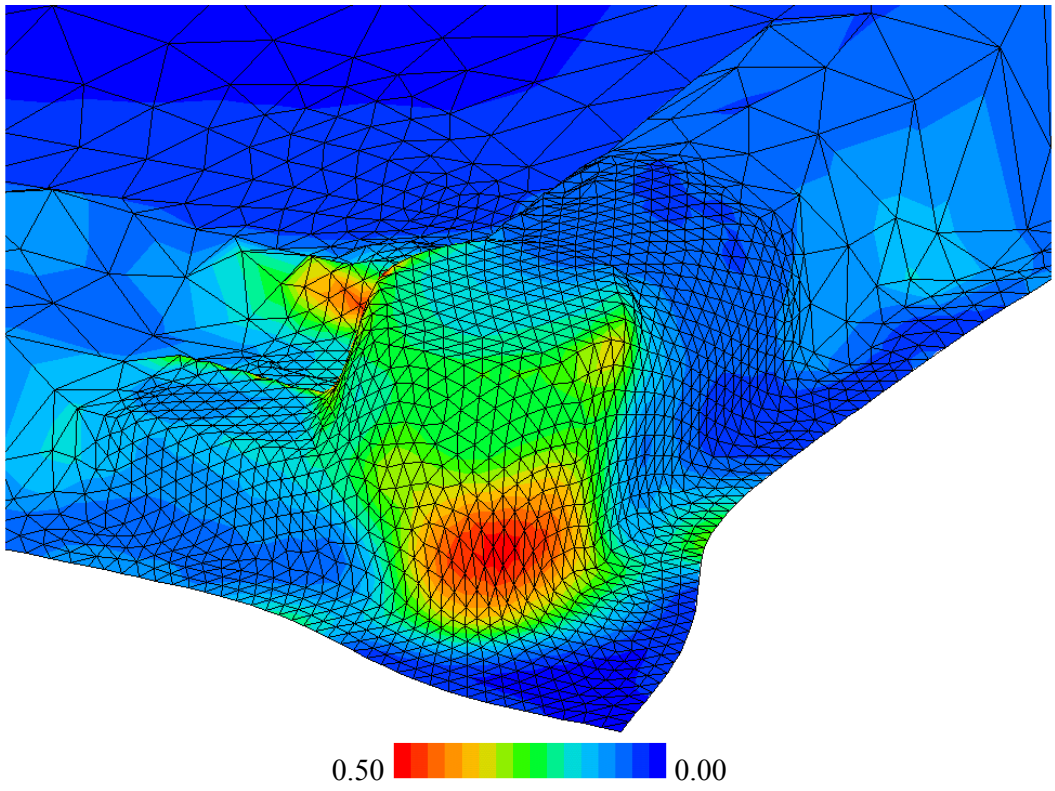

Figure 6-42 *Equivalent plastic strain of a detail of the deformed mesh of the heat exchanger part.*

6.7 Concluding Remarks

In order to analyse a deep drawing product the finite element simulation is a suitable tool. Depending on the deep drawing product and the problem to be solved different models can be used.
The square cup problem showed the influence of the number of elements, the influence of the element type and the influence of the friction model. The number of elements does not necessary have to be as large as possible because from a certain level onwards no further improvement of the results is found. The same holds for the element type; the DST element describes the transverse shear stresses which are not important for this product. So, the DKT3 element is good enough. Varying the punch speed influences the friction behaviour which results in different punch forces.
The phenomena of springback and wrinkling are examined by the S-Rail. A strip model is used to examine the springback behaviour of the DKT3 element for this deep drawing part. With the obtained knowledge the complete S-Rail is simulated in an efficient and effective way. The simulation and the experiments correspond in a high degree.
The Limiting Dome Height problem showed the influence of the material description. The Vegter yield function which depends on multi axial stress states performs better than the classical Hill yield function which only depends on the uni axial stress state. The punch height at failure is predicted with help of a forming limit diagram. For this problem the simulation and the experiments are also highly correspondend.
The deep drawing of the bracket headlight is a process with drawbeads. In order to incorporate the drawbeads, the equivalent drawbead is used. The equivalent drawbead with the restraining force and the strain changes gives a reliable description of the real drawbead behaviour.
The mini bonnet is a deep drawing part made of sandwich laminate. An adjustment to the existing DST element was sufficient to characterise the sandwich laminate behaviour. The possibility of looking in the material, for example at the core of the sandwich laminate, is an advantage of the finite element simulations.
The spin-off applications showed the possibility of simulating industrial products with the finite element program DIEKA. The computation time is acceptable but the preparation time has to be shorten.

6.8 References

[Atzema, 1994]
Atzema, E. H., *Formability of sheet metal and sandwich laminates,* PhD-thesis, University of Twente, 1994

[Haar, 1996]
Haar R. ter, *Friction in sheet metal forming, the influence of (local) contact conditions and deformation*, PhD-thesis, University of Twente, 1996

[Langerak, 1996]
Langerak, N. A. J., D. E. ten have, J. J. Smit, *The deep drawing of zinc coated steel; finite element modelling and experimental verification.* Body assembly & manufacturing IBEC '96, Detroit, 1996

[Numisheet, 1993]
Benchmark problems, Numerical simulations of 3-D sheet metal forming processes, A. Makinouchi et al (eds.),1993

[Numisheet, 1996]
Benchmark problems, Numerical simulations of 3-D sheet metal forming processes, J.K. Lee et al (eds.),1996

[Pape, 1995-1]
Pape G, *A FEM simulation model for plastic forming of sandwich laminate*, Graduate report (in Dutch), University of Twente, 1995

[Pape, 1995-2]
Pape G, *Finite element deep drawing simulations of VD II in Hylite*, Report WB-TM-1272 (in Dutch), University of Twente, 1995

[Vreede, 1992]
Vreede P.T., *A finite element method for simulations of 3-dimensional sheet metal forming*, PhD-thesis, University of Twente, 1992

[Wiedijk, 1995]
Wiedijk C.H.M., *The strip model, a model for the plane strain condition in a product*, Graduate report (in Dutch), University of Twente, 1995

7. Conclusions and Recommendations

In this research the finite element program DIEKA has been improved to better handle the deep drawing process and to better satisfy the requirement for industrial applications. Some applications are shown to illustrate the possibilities of the present program. Conclusions are drawn and for future research some recommendations will be given.

In order to describe contact, numerical parameters as well as physical parameters must be chosen. The numerical parameters must be chosen very carefully. The right balance between an accurate description and a stable calculation must be found. Knowledge of the contact algorithm and of the influence of every parameter helps to chose the right adjustment. The physical parameters such as the coefficient of friction also influences the simulation result. However, this parameter is obtained from experiments. Using a constant coefficient of friction or a coefficient of friction depending on the local contact conditions influences the results.
Plastic deformation of the sheet material influences the surface roughness. This influence must be examined and implemented in the Stribeck friction model.

An other important factor is the contact detection. The contact detection must be reliable and preferably fast. Two types of distance check can be performed. The nodal search is faster than the pinball search but it is not applicable for every tool description. The combination with the block search considerably speeds up the contact search.
A recommendation to speed up the calculation is to reduce the solver time. A technique to achieve this is to use an iterative solver instead of a direct solver. An additional recommendation is the use of automatic adaptive remeshing. The initial blank is modelled with rather large elements and during the simulation the blank will automatically be refined at the places where necessary. The preparation for the simulation still takes too much time, especially generating tool-files out of the CAD-data. A CAD-interface is already under development in order to shorten the tool generation

The material model is of major importance for a reliable finite element simulation. The Vegter yield function uses multi-axial stress states to describe the material behaviour whereas the Hill yield function only uses the uni-axial stress state. The Vegter yield function is preferred when an accurate material description is required.
The Vegter yield function needs an extensive experimental program to obtain the reference points. At this moment the pure shear point is an estimated value. An experiment to determine the pure shear point is under development and highly recommended.
In order to incorporate the deformation velocity effects, the material model can be extend with rate dependent material behaviour. The scalar hardening law can be extended to an anisotropic tensorial hardening law.

A widespread method to predict failure is the use of a forming limit diagram (FLD). The FLD approach proves to accurately determine the failure. It can also be used to predict failure in a coating.

Drawbeads are used to locally control the flow of the material, They do not only prevent the material from moving to fast but they also change the material properties. An equivalent drawbead model is implemented. The equivalent drawbead effectively replaces the real drawbead geometry when both the restraining force and the strain changes are considered.
The equivalent drawbead is under development for the plate bending elements. This will result in more accurate deep drawing simulations.

Determination of springback is important during the manufacturing of deep drawing products. An elastic plastic material description necessary to describe this phenomenon is implemented. When balancing the accuracy and the computational cost of the simulation, four integration points in thickness direction are preferred.